# DEGENERATE FOUR-WAVE MIXING SPECTROSCOPY IN COLLISIONALLY DOMINATED ENVIRONMENTS: THEORY AND APPLICATION

A DISSERTATION
SUBMITTED TO THE DEPARTMENT OF CHEMISTRY
AND THE COMMITTEE ON GRADUATE STUDIES
OF STANFORD UNIVERSITY
IN PARTIAL FULFILLMENT OF THE REQUIREMENTS
FOR THE DEGREE OF
DOCTOR OF PHILOSOPHY

by
Skip Williams
January 1994
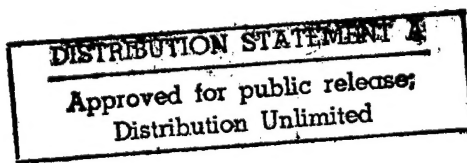
19980115 183

REPORT DOCUMENTATION PAGE			Form Approved OMB No. 0704-0188

Public reporting burden for this collection of information is estimated to average 1 hour per response, including the time for reviewing instructions, searching existing data sources, gathering and maintaining the data needed, and completing and reviewing the collection of information. Send comments regarding this burden estimate or any other aspect of this collection of information, including suggestions for reducing this burden, to Washington Headquarters Services, Directorate for information Operations and Reports, 1215 Jefferson Davis Highway, Suite 1204, Arlington, VA 22202-4302, and to the Office of management and Budget, Paperwork Reduction Project (0704-0188) Washington, DC 20503.

1. AGENCY USE ONLY (Leave Blank)	2. REPORT DATE January 1994	3. REPORT TYPE AND DATES COVERED Final

4. TITLE AND SUBTITLE Degenerate Four-Wave Mixing Spectroscopy in Collisionally Dominated Environments: Theory and Application	5. FUNDING NUMBERS

6. AUTHORS
Skip Williams

7. PERFORMING ORGANIZATION NAME(S) AND ADDRESS(ES)
Stanford University

AFRL-SR-BL-TR-98-

$\bigcirc\bigcirc$|⁊

AGENCY REPORT NUMBER

9. SPONSORING/MONITORING AGENCY NAME(S) AND ADDRESS(ES)
AFOSR/NI
110 Duncan Avenue, Room B-115
Bolling Air Force Base, DC 20332-8080

11. SUPPLEMENTARY NOTES

12a. DISTRIBUTION AVAILABILITY STATEMENT
Approved for Public Release

12b. DISTRIBUTION CODE

13. ABSTRACT *(Maximum 200 words)*
See attached.

DTIC QUALITY INSPECTED 2

14. SUBJECT TERMS

15. NUMBER OF PAGES

16. PRICE CODE

17. SECURITY CLASSIFICATION OF REPORT Unclassified	18. SECURITY CLASSIFICATION OF THIS PAGE Unclassified	19. SECURITY CLASSIFICATION OF ABSTRACT Unclassified	20. LIMITATION OF ABSTRACT UL

Standard Form 298 (Rev. 2-89)
Prescribed by ANSI Std. 239.18
Designed using WordPerfect 6.1, AFOSR/XPP, Oct 96

I certify that I have read this dissertation and that in my opinion it is fully adequate, in scope and quality, as a dissertation for the degree of Doctor of Philosophy.

Richard N. Zare (Principal Advisor)

I certify that I have read this dissertation and that in my opinion it is fully adequate, in scope and quality, as a dissertation for the degree of Doctor of Philosophy.

Charles H. Kruger

I certify that I have read this dissertation and that in my opinion it is fully adequate, in scope and quality, as a dissertation for the degree of Doctor of Philosophy.

Hans C. Anderson

Approved for the University Committee on Graduate Studies

iii

ABSTRACT

The potential of degenerate-four wave mixing (DFWM) spectroscopy for the analysis of molecular species in high-pressure, high-temperature environments has been explored theoretically and experimentally. In addition, the reliability of DFWM has been assessed by comparing to laser induced fluorescence (LIF) measurements under the same experimental conditions. The results of these studies suggest that DFWM can provide quantitative information regarding trace molecular species in environments in which collisions and source emission hinder analysis by other means.

DFWM has been used to detect the CH radical in an atmospheric-pressure oxyacetylene flame via the (0,0) and (1,1) bands of the $A^2\Delta$-$X^2\Pi$ system. The CH radical is a minor flame species and is important for understanding the primary reaction zone of many combustion environments. We have observed CH radicals with comparable sensitivity by both DFWM and LIF. From these measurements, we estimate a DFWM detection limit of 4×10^{11} molecules/cm^3 (4×10^9 molecules/cm^3 per quantum-state) for CH at atmospheric pressure. Vibrational temperatures and concentration profiles of CH obtained by both techniques are in good agreement.

Diagrammatic perturbation theory combined with a spherical tensor treatment is used to decompose the DFWM signal resulting from an isotropic molecular sample into a sum of three multipole moments in the weak-field (no saturation) limit. The zeroth moment gives the relative internal-state population contribution, the first moment the orientation contribution, and the second moment the alignment contribution to the DFWM spectra. This treatment makes explicit how the magnitude of the DFWM signal depends on the polarizations of the other three beams and the collisional relaxation caused by the environment. A general expression is derived for the DFWM signal for an arbitrary geometric configuration of the beams (arbitrary phase matching geometry). Under the assumption that the rates of collisional relaxation of the population, the orientation, and the alignment are the same, simple analytic expressions are found for the most commonly used experimental configurations, which should facilitate the practical analysis of DFWM spectra.

Effects of field polarization and field intensity in DFWM have been investigated, and rotational distributions (temperatures) have been obtained for the CH radical using saturated DFWM. As the field intensity increases optical pumping rates become larger than the population relaxation and collisional dephasing rates, and the DFWM signal saturates becoming relatively insensitive to collisions. The saturation behavior predicted

iv

by nondegenerate two-level models is in close agreement with the observed power dependence of the (0,0) band transitions of the $A^2\Delta$-$X^2\Pi$ system. The DFWM saturation intensity does not change significantly as the polarization states of the excitation fields are changed. However large differences in the DFWM signal intensities are observed as a function of input field polarization and rotational branch. These differences are nearly independent laser intensity. The DFWM signal intensity differences are rationalized using diagrammatic perturbation theory. The weak-field expressions reproduce the data taken at saturating intensities with an accuracy of 10-30%. The important aspects of the reduction of saturated DFWM signal intensities to relative internal-state distributions in environments where population relaxation and coherence dephasing events are dominated by collisions are outlined. Rotational temperatures obtained by this method are estimated to be accurate to 5%.

To my parents

ACKNOWLEDGMENTS

group members with whom I have had valuable interactions are too numerous to list, but I am grateful to them all. The Zarelab is a wonderful place to be, and I am glad to have been a part of it.

I am especially indebted to those who have contributed indirectly to my thesis. I thank my mother and father for their love and support and my brother for always reminding me of what is *really* important in life. My wife Stacie has been my greatest source of joy over the years, and without her love, encouragement, and support none of this would have transpired. I love her deeply and look forward to many years of science, adventure, and happiness together.

Table of Contents

List of Tables

List of Figures

Chapter 4

CHAPTER 1

Overview

- Into the storm -

In between the extremes of ultrahigh vacuum and the condensed phase lies the regime of high-pressure (several hundred Torr and above) and high-temperature (several hundred Kelvin and above) gases of which flames and plasmas are the most common examples. The dynamics of these environments are complicated compared to low-pressure studies because of the high collisional rates. Of course, many "collisions" occur in the condensed phase, but the situation can be reduced by only considering nearest neighbor interactions; for example the problem can be simplified to a solute in a solvent shell or a dopant in a crystal lattice. In high-temperature, high-pressure gases the collisional rates approach those of the condensed phase, but the mobility of interacting particles is much higher. Therefore a given molecular species can interact with a variety of other molecules and surroundings. In addition these environments are "hostile" in the sense that they are usually associated with high levels of emitted radiation, limited access, nonequilibrium molecular concentrations and energy distributions, and large gradients in temperature and concentration. Most of these environments pose a severe challenge to those who wish to probe their chemical composition, kinetics, and dynamics as a function of spatial distribution and temporal evolution. Even though these environments are technically challenging, their importance warrants the experimental effort required to investigate them.

The goal of my thesis is to develop a laser-based diagnostic tool for the investigation of trace molecular species and reaction processes in collisionally dominated environments. Specifically, the development of a technique that can be used for the investigation of the plasma chemistry existing in the flow of an atmospheric-pressure rf inductively-coupled plasma that is part of a materials processing facility in the High Temperature Gasdynamics Laboratory (HTGL) at Stanford. This goal is accomplished by exploiting a relatively new nonlinear spectroscopy called degenerate four-wave mixing (DFWM). The results are complemented by companion studies using laser induced fluorescence (LIF).

Reactive plasmas are harsh environments important to energy science and technology. The nonequilibrium behavior of thermal plasmas is of particular concern in the area of plasma chemistry and plasma processing. Previous experiments have probed the nonequilibrium plasma state, excitation temperatures, electron densities, radiation escape, recombination rates, and electronic quenching effects. Emission and LIF measurements have met with limited success because of the brightness of the source and the high temperatures and pressures within the plasma. A need exists for *in situ* nonintrusive techniques that can probe nonequilibrium behavior, characterize related

2

chemical properties, and monitor trace molecular species free from source interference and collisional effects. The experimental and theoretical efforts presented in this thesis have been and are currently being applied at HTGL to understand the gas-phase and gas-surface interactions encountered in the boundary layer of their reactive plasma.

Operated on a variety of gas mixtures, especially $CH_4/H_2/Ar$, the HTGL plasma reactor has been used in the past few years to gain experience in studying chemical vapor deposition of diamond thin films. A small scale "reactor" was set up in our laboratory that consisted of an oxyacetylene flame that was operated under conditions known to be capable of growing diamond thin films. The temperatures, collisional rates, and CH radical concentrations are very similar for the flame and the HTGL plasma, so experiments that emphasized the investigation of DFWM as a diagnostic were conducted in the relatively controlled environment provided by the flame.

DFWM was chosen because it offers a means of measuring spatially resolved temperature and concentration information with a very high degree of spectral, spatial, and temporal resolution. In addition, the problem of plasma luminescence is largely overcome with DFWM because it provides a coherent, directional beam that can be detected remotely without loss in intensity. In Chapter 2, DFWM is evaluated with regard to its potential to provide sensitive detection of molecular species and quantitative determinations of CH vibrational temperatures and relative concentrations in the primary reaction zone of an atmospheric-pressure oxyacetylene flame. DFWM is found to be as sensitive and as accurate LIF under our experimental conditions.

Vibrational temperatures, however, may not be equilibrated with the translational temperature. Therefore rotational temperatures are needed because they are more likely to represent the translational temperature of the environment. The ability to reduce DFWM rotational spectra to relative populations is key to the ultimate success of the technique. Chapter 3 shows how the magnitude of DFWM signal resulting from an isotropic molecular sample depends on the degeneracies of the levels involved, the polarizations of the excitation fields, the phase matching geometry, and the collisional relaxation and dephasing caused by the environment. Simple analytic expressions are provided which should facilitate the practical analysis of DFWM spectra. However obtaining an accurate and complete set of relaxation rates for a given molecule in a specific environment is a formidable task. This difficulty results because these rates are typically dependent on temperature, collision partner, and quantum state, and therefore, are not known for a wide range of conditions.

An appealing aspect of DFWM is that the signal intensity becomes relatively insensitive to the specific value of the relaxation rates in the saturation regime. In this regime, the problem of extracting relative population distributions essentially reduces to knowing the absorption coefficients. This aspect is discussed in detail in Chapter 4 where DFWM signals are presented as a function of field polarization and field intensity. Also in Chapter 4 the important aspects of the reduction of saturated DFWM signal intensities to relative internal-state distributions are outlined for environments where population relaxation and dephasing events are dominated by collisions, and a rotational temperature analysis is presented of the CH radical in an atmospheric-pressure oxyacetylene flame. Rotational temperatures determined using the procedures discussed in Chapter 4 are estimated to be accurate to 5%.

CHAPTER 2

Evaluation of DFWM as a Spectroscopic Molecular Probe

A person with one thermometer knows the temperature.

A person with two is not sure.

Kermit C. Smyth

I. INTRODUCTION

Highly luminous sources, such as arcs, sparks, flames, explosions, plasmas, and discharges, pose a severe challenge to those who wish to probe their chemical composition, kinetics, and dynamics as a function of spatial distribution and temporal evolution. Nonintrusive optical methods,[1] like LIF, are hindered by interference from background emission, distortions caused by source temperature and density inhomogeneities, and collisional energy transfer and quenching processes that readily occur at high pressures. One method to overcome these difficulties is a four-wave mixing technique called coherent anti-Stokes Raman scattering (CARS).[1,2] This can provide a coherent signal propagating in a known direction so that its detection can be accomplished with excellent rejection of source emission. Another nonlinear technique that shares the same characteristics is DFWM[3] with the extra advantages that (1) DFWM involves one-photon resonances and is therefore more sensitive, and (2) DFWM employs a single frequency provided by one laser source and therefore is easier to implement.

DFWM is a third-order nonlinear optical process in which three fields of a single frequency ω overlap in a medium to produce a coherent fourth field which also has frequency ω. This process may also be understood in terms of light scattering from a grating. We employ the collinear phase-conjugate geometry which consists of two coaxial and counterpropagating pump fields, denoted E_f (forward) and E_b (backward), which are crossed at a small angle θ by a probe field, E_p. The grating picture of DFWM involves the interference of E_f, E_b, and E_p. When the frequency is tuned to an atomic or molecular resonance, the interference leads to a spatial modulation in the (complex) refractive index, and hence forms a grating. Two important modulation patterns result, as are shown in Fig. 1: E_f and E_p form a grating that causes E_b to be scattered into E_s (the DFWM signal), which is the phase conjugate of E_p ($E_s \propto E_p^*$); and E_b and E_p form a finer grating with spacing and orientation to scatter E_f into E_s. A third grating, that arises from the interference of E_f and E_b, does not contribute to this process because it is not phase matched for the scattering of E_p into E_s. The depth of modulation of the gratings is minute, and their scattering efficiency is poor (about $1:10^9$ under the present conditions), but E_f and E_b have so many photons that E_s is readily detected. Although DFWM is in its infancy as a nonlinear laser spectroscopy, it has been used to detect atomic[4-12] and molecular species[13-21] in a variety of conditions. In combustion systems, sodium[4-6,9] and lithium[11] atoms have been detected in atmospheric-pressure

6

FIG. 2.1. Grating picture of DFWM. (a) The interference pattern between forward pump E_f and probe E_p establish a large-spaced grating relative to (b) the small-spaced grating established between backward pump E_b and probe E_p. The phase-conjugate field E_s is the generated DFWM signal.

Grating Picture of DFWM

(a)

Forward Pump $\vec{E}_f$

θ

Probe $\vec{E}_p$

Backward Pump $\vec{E}_b$

$\vec{E}_s$

Phase Conjugate DFWM signal

Grating Spacing
$D = \lambda / [2\sin(\theta/2)]$

(b)

Backward Pump $\vec{E}_b$

Probe $\vec{E}_p$

Forward Pump $\vec{E}_f$

$\vec{E}_s$

Phase Conjugate DFWM signal

Grating Spacing
$D = \lambda / [2\cos(\theta/2)]$

8
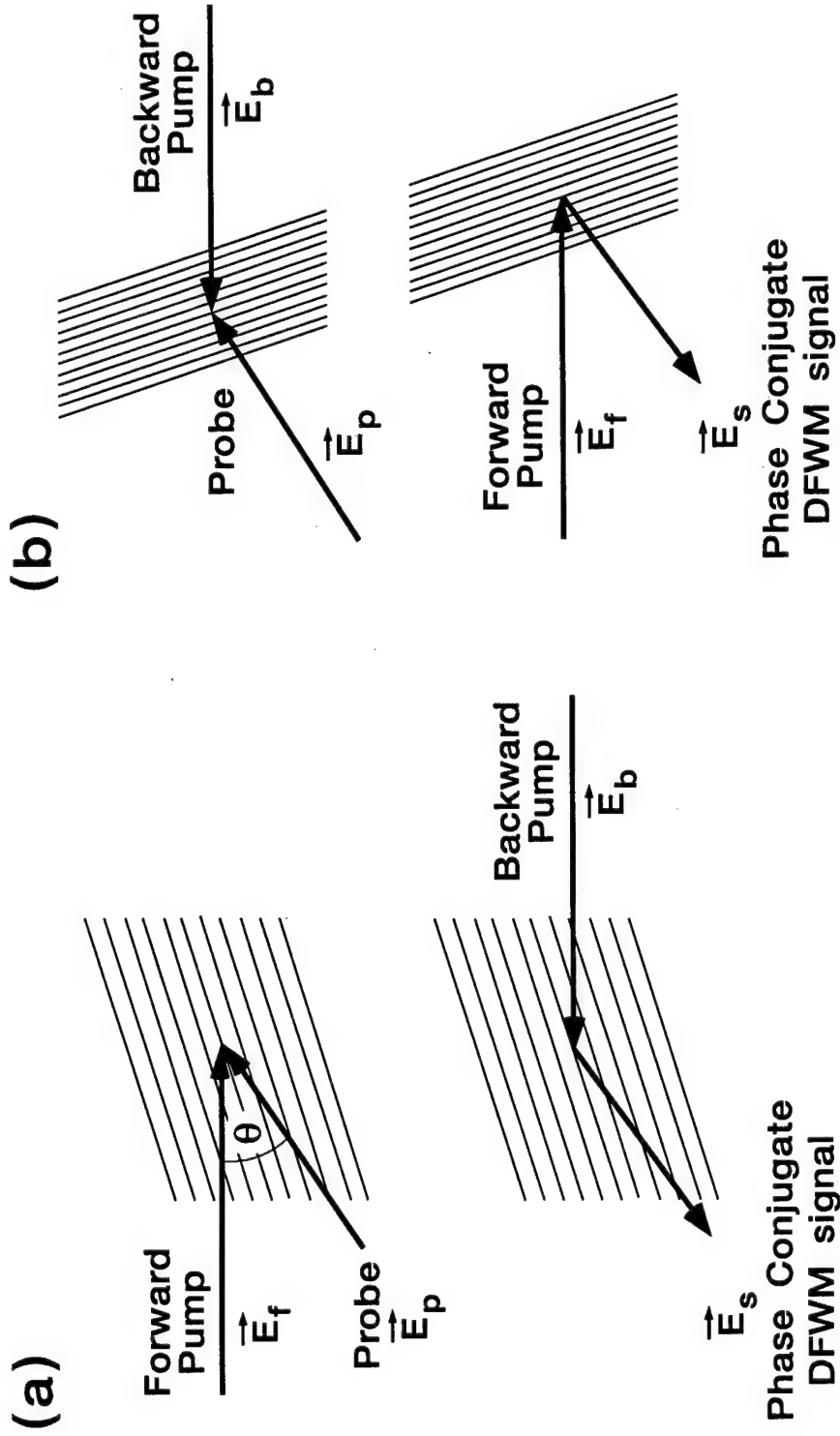
flames with high sensitivity. Ewart and O'Leary were the first to detect a molecular species, OH radical, by DFWM in an atmospheric-pressure flame,[14] and Rakestraw, Farrow and Dreier have quantified OH[15] in an atmospheric flame and NH[17] in a low-pressure flame.

We report here the first DFWM study of the CH radical, found as a trace species (30 ppm), in an atmospheric-pressure oxyacetylene flame. From these measurements, we estimate a detection limit (signal-to-noise ratio of 1) of 4×10^{11} molecules/cm^3 (4×10^9 molecules/cm^3 per quantum state) for CH. At high pressures, rotational distributions from LIF measurements become difficult to interpret because of the rotational level dependence of the fluorescence quantum yield, which results from collisions.[22,23] Therefore to make a direct comparison between DFWM and LIF, we compare the (0,0) and (1,1) intensities of a single rotational level of the CH $A^2\Delta$-$X^2\Pi$ system to obtain CH concentration profiles and vibrational temperatures. Saturation properties of DFWM and LIF signal intensities and line shapes are also presented.

II. EXPERIMENTAL SECTION

A. Experimental Apparatus

Figure 2 shows the experimental configuration in which three fields of the same frequency overlap in the reaction zone of an atmospheric-pressure oxyacetylene flame to generate a fourth field (the DFWM signal). The two coaxial and counterpropagating pump fields, denoted E_f (forward) and E_b (backward), are crossed at a small angle, $\theta=2°$, by a probe field, E_p. The DFWM signal field, E_s, is coherently generated and propagates 6 m to a photomultiplier where it is detected. At the same time, the LIF signal is obtained by imaging the reaction zone of the flame on the entrance slit of a 0.75-m monochromator and is detected with a photomultiplier. The specific details of the experiment are given below.

Excitation is provided by a KrF excimer-pumped dye laser system (Lambda Physik EMG 102 MSC and FL 2002) operated over the wavelength range of 425-450 nm with a bandwidth of 0.18 ± 0.02 cm^{-1} and a pulse width of 16.3 ± 1 ns (fwhm). The bandwidth was measured with an etalon, and the pulse width was measured with a fast photodiode and a digitizing oscilloscope (HP54510A). The output beam of the dye laser is spatially filtered to improve the beam profile. The beam profile was measured by the

FIG 2.2. Experimental configuration for the simultaneous measurement of DFWM and LIF signals. Spectra are recorded with unfocused beams (diameter ~ 0.5 mm) having energies of 12 μJ for the forward and backward pump beams and 3 μJ for the probe beam. The flame consists of a standard welding torch fitted with a 0.94 mm diameter nozzle. The oxygen to acetylene volumetric flow ratio, $R = O_2/C_2H_2$, is 0.947. The abbreviations used in the figure are defined as follows: M: mirror, P: polarizer, L: lens, PH: diamond pinhole, PEM: photoelastic modulator, BS: beamsplitter, EM: energy meter, BPF: bandpass filter, PMT: photomultiplier tube.
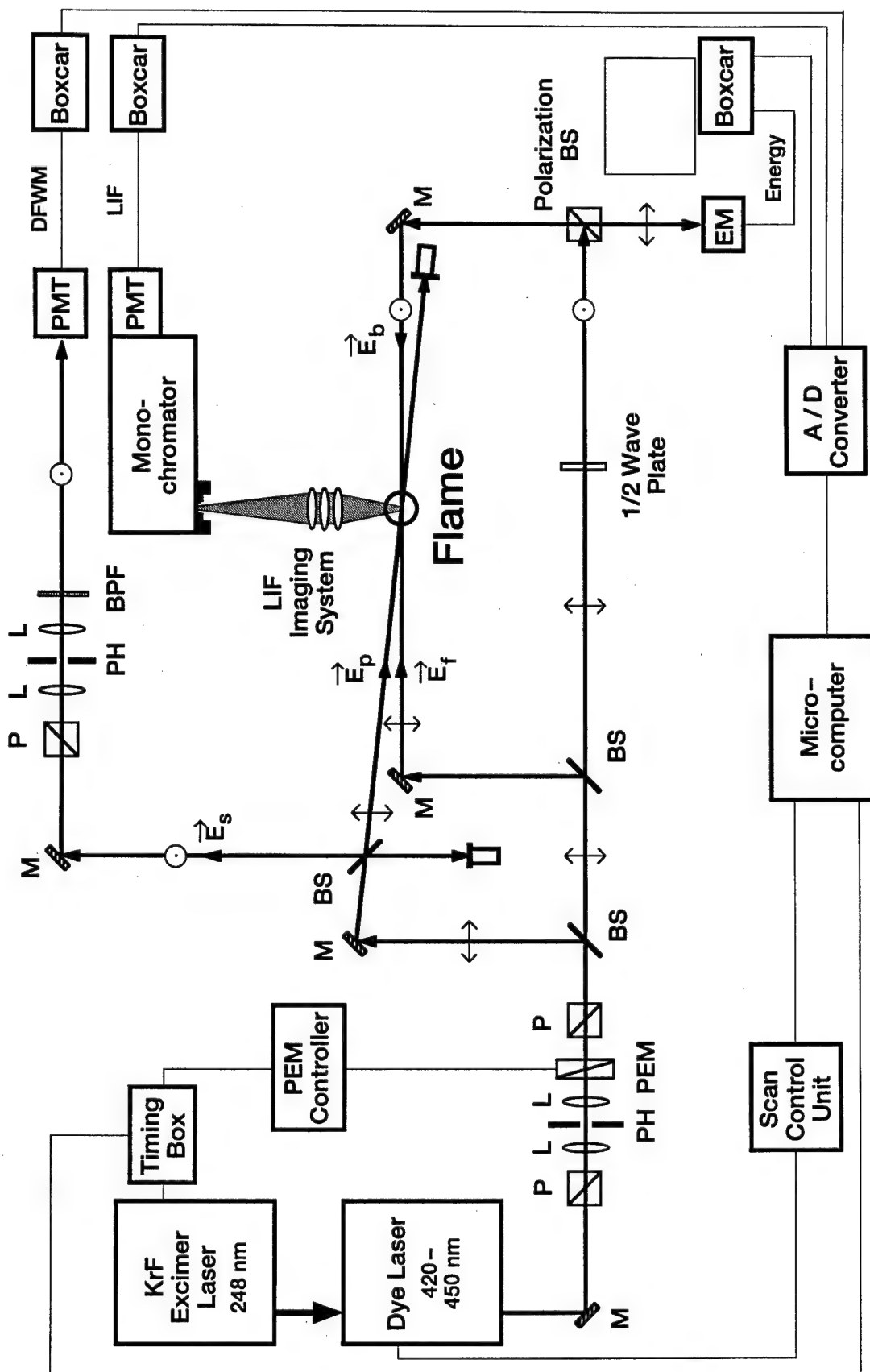
procedure outlined in reference 24 and was found to be well described by a cylindrical Gaussian beam profile with a fwhm of 0.47 mm. The laser energy is controlled using a photoelastic modulator (Hinds International PEM-CF4) between two crossed polarizers which allows the laser energy to be adjusted between 1 and 800 μJ with no significant beam walk over distances of several meters. The energy of the probe beam is one quarter of the forward pump beam, and the energy of the backward pump beam is adjusted to the value of the forward pump beam using a half-wave plate and a polarization beamsplitter which reflects S-polarized and transmits P-polarized light. We measure the forward pump beam energy by placing an energy meter (Molectron J4-09) after the polarization beamsplitter, which allows the energy of the forward pump to be measured directly and accurately to a few microjoules. In calculating the laser spectral intensity for these experiments from the measured beam energies, we use $\Delta \overline{v} = 0.18 \pm 0.02$ cm^{-1}, $\Delta \tau = 16.3 \pm 1$ ns, and $A=\pi(d/2)^2$ where $d/2$ is the 1/e intensity radius of a cylindrical Gaussian beam ("top hat" beam diameter).[25] For example, the beam energies employed in these experiments are 12 μJ for the forward and backward pump beams and 3 μJ for the probe beam, which correspond to 1.65×10^6 W/cm^2-cm^{-1} and 0.41×10^6 W/cm^2-cm^{-1}, respectively.

The experiment is configured with the forward pump and probe (E_f and E_p) having the same linear polarization (P plane) and backward pump (E_b) having a linear polarization rotated by 90° with respect to the forward pump and probe (S plane). The DFWM signal (E_s) has the same linear polarization as the backward pump (S plane) and propagates along the same axis but in the opposite direction of the probe. Since the signal (E_s) is produced in a known direction, ($k_s = -k_p$), alignment of the detection axis can easily be achieved by retro-reflecting the probe beam through a retardation plate. The DFWM signal is collected with a 40% beamsplitter and passes through a series of apertures, a polarizer and a bandpass filter before being detected with a photomultiplier (Hamamatsu R2393P).

The LIF signal is collected with f/1 optics at 90° with respect to the pump beam axis and focused on the entrance slit of a 0.75 m single monochromator (Spex 1702) with a 1800 gr/mm grating. The entrance slit of the monochromator is set at 1 mm x 2 mm (width x height), and the exit slit width is set at 2.5 mm, which results in a trapezoidal-shaped spectral bandpass function with a 1.4 nm bandpass at the top and a 2.2 nm bandpass at the base. When the grating is tilted, the monochromator functions as a narrow variable bandpass filter though which the LIF light passes before being detected with a photomultiplier (Thorn EMI 9558). The grating of the monochromator is

positioned to give a flat bandpass response from 430.4 to 431.8 nm (λ/vac) which passes the Q(2-12) transitions of both the (0,0) and (1,1) bands while discriminating against the P and R branches.

Signals from DFWM and LIF are amplified (Lecroy VV100BTB) before being processed by separate boxcar averagers (SRS SR250). The laser energy is processed directly by a boxcar averager (SRS SR250). The three channels are read at each wavelength, digitized and averaged over 30 laser shots. The data is then stored on a microcomputer (IBM XT) for further analysis.

B. Flame

The atmospheric-pressure oxyacetylene flame consists of a standard welding torch fitted with a 0.94 mm diameter nozzle operated in the open air. The flows of acetylene and oxygen are maintained with mass flow controllers (MKS) at 380 cc/min and 360 cc/min respectively. This results in an oxygen to acetylene volumetric flow ratio, $R = O_2/C_2H_2$, of 0.947 and an equivalence ratio, Φ, of 2.63 (fuel rich) with respect to the combustion reaction

$$C_2H_2 + 5/2\ O_2 = 2\ CO_2 + H_2O.$$
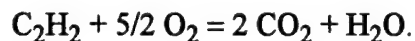
Joklik[26] has extensively studied the CH radical in an oxyacetylene flame at low pressure. At a pressure of 40 Torr the CH concentration decreased from 23.6 ppm at Φ=1 to 11.0 ppm at Φ=1.4, as measured by absorption. Similarly, the CH^* ($A^2\Pi$) concentration measured by emission decreased from 0.018 ppm at Φ=1 to 0.009 ppm at Φ=1.4. Furthermore, the CH and CH^* concentrations in ppm were found to be independent of pressure from 20 to 100 Torr and to increase with temperature. These low-pressure studies give much insight into the production of CH in oxyacetylene flames, but quantitative extrapolation of these findings to our experimental conditions at atmospheric-pressure is unreliable. However, Jessen and Gaydon[27] measured the CH concentration in a premixed atmospheric-pressure oxyacetylene torch by absorption spectroscopy and estimated the concentration to be tens of ppm. Bonczyk and Shirley[28] measured the CH concentration to be 23 ppm by saturated LIF and 57 ppm by absorption in a premixed atmospheric-pressure flame with Φ=1. Finally, Matsui, Yuuki, and Sahara[29] modeled a premixed atmospheric-pressure flame with $\Phi \geq 2.5$ and measured the relative C_2 concentration profiles in an oxyacetylene circular torch burner at atmospheric pressure. The agreement between the calculated C_2 concentration and their measured

values was good, and the code predicted C_2 concentrations in agreement with absolute measurements made by other workers. The equilibrium CH concentrations estimated from their code (see Fig. 10 of reference 29) is 20-30 ppm for $\Phi \sim 2.5$. Therefore, we estimate a CH concentration for $\Phi=2.63$ of 30 ppm in our atmospheric-pressure oxyacetylene flame.

C. CH Spectral Features

Vibrational temperatures and spatial profiles are derived from the integrated signal intensities of the well resolved $R_{1e}(8)$, $R_{1f}(8)$, $R_{2e}(8)$ and $R_{2f}(8)$ transitions of the (0,0) and (1,1) bands of the $A^2\Delta$-$X^2\Pi$ system.[30] Figure 3 shows DFWM and LIF spectra at 0.4 mm above the burner nozzle. The fine-structure components of the R(8) transition in Fig. 3 are distinguished as follows: $1 = {}^2\Delta_{5/2}$–${}^2\Pi_{3/2}$, $2 = {}^2\Delta_{3/2}$–${}^2\Pi_{1/2}$, and the Λ-doublets are labeled e and f. The A-X system is highly diagonal, i.e., the potential curves are nearly identical, causing the (0,0) and (1,1) bands to have essentially equal transition probabilities with values approximately two orders of magnitude larger than the off-diagonal transitions (0,1), (1,0), and (1,2).[31,32] Both the X and A states rapidly approach Hund's case (b) coupling as rotation increases. Therefore, the sets of Einstein emission and absorption coefficients are taken to be equal for all of the R(8) transitions.

III. QUANTIFICATION BY DFWM

Although a generalized description of DFWM including collisional, polarization, and saturation effects does not exist at the present time, Abrams and Lind (AL)[3,33,34] have presented a model of DFWM that has given much insight to the process, as has been shown by good agreement with experiments.[15,17,18,20,35] The model considers a nondegenerate two-level atomic system in the presence of arbitrary pump amplitudes and weak probe and signal amplitudes. The probe and signal amplitudes are weak in the sense that they do not significantly affect the level populations whereas the pump amplitudes can be well above saturation. In this model all fields have the same polarization and their *k*-vectors are configured in the collinear phase-conjugate geometry discussed above. For the case of equal intensity pumps and low absorption, the expressions presented by AL are easily reduced[18] to an expression for the line-center signal intensity given by

14
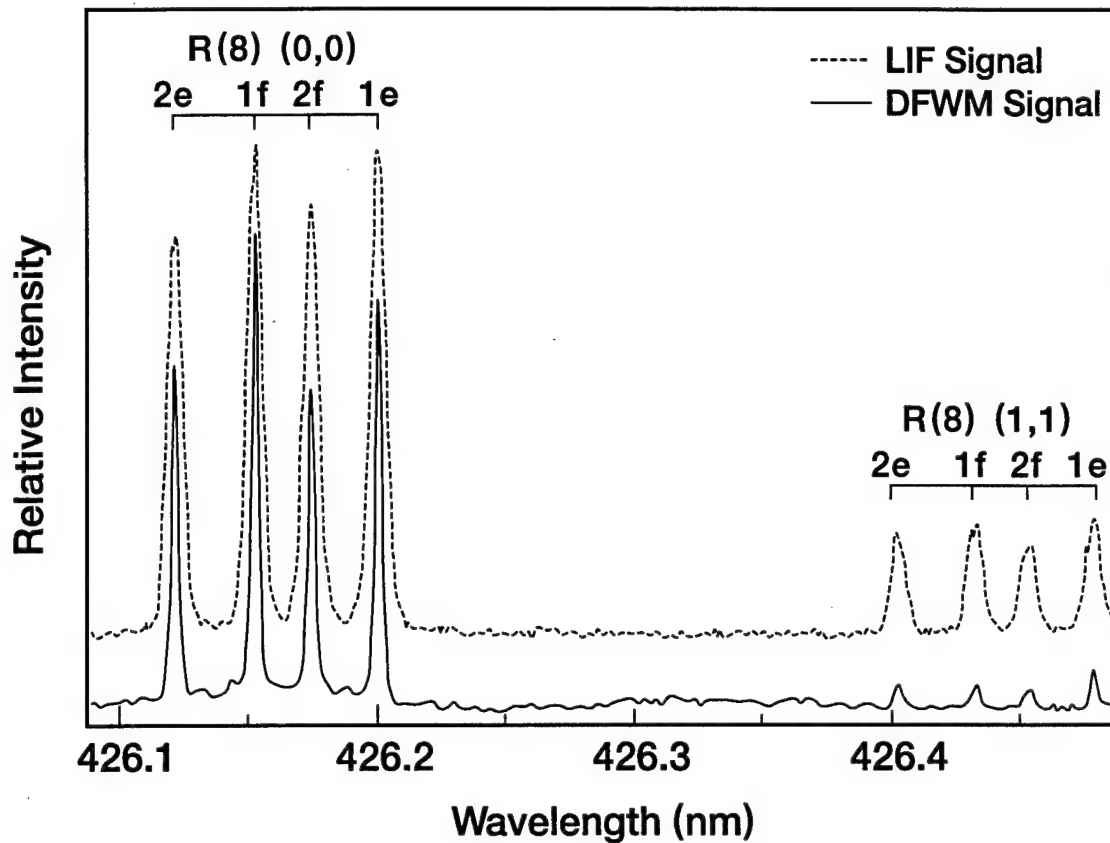
FIG. 2.3. DFWM and LIF spectra for the R(8) lines of the CH $A^2\Delta-X^2\Pi$ (0,0) and (1,1) bands at a position of 0.4 mm above the burner nozzle. These spectra are recorded simultaneously and represent an average of 30 laser shots. The fine-structure components are distinguished as follows: $1 = {}^2\Delta_{5/2}-{}^2\Pi_{3/2}$, $2 = {}^2\Delta_{3/2}-{}^2\Pi_{1/2}$, and the Λ doublets are labeled e and f. The small difference in the Boltzmann factors of the $R_1(8)$ and $R_2(8)$ transitions is enhanced in the DFWM spectrum compared to the LIF spectrum, because the DFWM intensities depend quadratically on the population difference whereas the LIF intensities depend linearly.

$$I_{DFWM} = 4\alpha_o^2 L^2 \frac{\left(I/I_{sat}\right)^2}{\left(1 + 4I/I_{sat}\right)^3} I_p, \tag{1}$$

where

$$\alpha_o = \frac{\omega_o \Delta N_o \left|\mu_{ge}\right|^2}{2nc\varepsilon_o \hbar \Gamma_{eg}} \tag{2}$$

is the line-center absorption coefficient, and

$$I_{sat} = \frac{c\varepsilon_o \hbar^2 \Gamma_o \Gamma_{eg}}{2\left|\mu_{ge}\right|^2} \tag{3}$$

is the line-center saturation intensity. Here $\Delta N_o = N_g - N_e$ is the population difference (molecules/cm^3) in the absence of applied fields, $\left|\mu_{ge}\right|^2$ is the square of the transition dipole moment (proportional to absorption cross-section) connecting the lower level (g) to the upper level (e), Γ_o and Γ_{eg} are the population and coherence decay rates respectively, n is the intensity-dependent index of refraction (reference 1, page 222, Eq. 19), and L is the effective interaction length of the radiation fields. All of the equations are in SI units, and the constants c, ε_o, and $\hbar$ have their usual meanings. The model predicts that the DFWM line-center intensity will be quadratic in the population difference of the transition. Equations (1)-(3) are used in this analysis, where we have replaced ΔN_o with the ground state population since $N_g(v'', J'') \gg N_e(v', J')$ at typical flame conditions. The widths of the DFWM lines for the (0,0) and (1,1) bands are found to be essentially the same. Thus we take the line-center peak heights as proportional to the integrated areas.

IV. QUANTIFICATION BY LIF

At high pressures, obtaining rovibrational distributions by LIF becomes difficult because of the dominating effect of collisions on the fluorescence quantum yield. However CH vibrational temperatures can be obtained relatively free from collisional effects because of the highly diagonal character of the CH A$^2\Delta$-X$^2\Pi$ transition and the similar energy transfer rates for the A$^2\Delta(v'=0, N')$ and A$^2\Delta(v'=1, N')$ states.[36] If the assumption is made that the collisional redistribution of population reaches steady state over the time period of the laser excitation, then the following relation for the fluorescence signal intensity is obtained for a two level system

$$I_{LIF} = Cf_B N_t \frac{A_{21}\left(IB_{ge}\right)}{Q+V+R+E+I\left(B_{ge}+B_{eg}\right)+A_{eg}}, \qquad (4)$$

where C is combined proportionality constant that includes the LIF collection efficiency, N_t is the total species population, and f_B is the Boltzmann factor for the rovibrational state being excited. The competing population transfer rates are defined as follows: A_{eg} is the rate of spontaneous emission; Q is the collision quenching rate; V is the vibrational energy transfer rate; R is the rotational energy transfer rate; E is the electronic energy transfer rate; IB_{ge} is the rate of absorption; and IB_{eg} is the rate of stimulated emission. The assumption of steady-state populations over the duration (~ 20 ns) of the laser pulse is a good one for CH in an atmospheric-pressure flame because the population redistribution is completed within a couple of nanoseconds.[36]

In general the energy transfer rates in Eq. (4) are dependent on temperature, collision partner and quantum state, and therefore, are not known for a wide range of conditions. This dependence has precluded the application of quantitative LIF at high pressures (several hundred Torr and above) because the detailed energy transfer rates as a function of theses variables are not known. However, Eq. (4) can be simplified for CH detection. The first simplification is that only the (0,0) and (1,1) bands need to be considered since they are approximately two orders of magnitude larger than the off-diagonal (0,1), (1,0) and (1,2) bands. In addition, the spontaneous emission, stimulated emission, and absorption rates are the same for the (0,0) and (1,1) bands.[31] Furthermore, vibrational energy transfer between the $A^2\Delta(v'{=}0)$ and $A^2\Delta(v'{=}1)$ states is insignificant for this system, however, rotational and electronic energy transfer rates are appreciable.[36] Since the monochromator bandpass is sufficiently large to collect all relevant Q-branch transitions for both the $A^2\Delta$-$X^2\Pi$ (0,0) and (1,1) transitions while discriminating against R- and P-branch transitions, the detected LIF signals for R(8) excitation will not be sensitive to rotational redistribution in the $A^2\Delta(v'{=}0)$ and $A^2\Delta(v'{=}1)$ states. Therefore, R can be eliminated in Eq. (4). Likewise, even if vibrational energy transfer between the $A^2\Delta(v'{=}0)$ and $A^2\Delta(v'{=}1)$ states occurs, the monochromator bandpass collects emission from both levels with equal efficiencies. Hence V can also be eliminated in Eq. (4). Electronic energy transfer, on the other hand, transfers population efficiently from the $A^2\Delta$ to the $B^2\Sigma^-$ state with significantly different rates for the $A^2\Delta(v'{=}0)$ and $A^2\Delta(v'{=}1)$ levels. Because the $B^2\Sigma^-$–$X^2\Pi$ fluorescence is outside of the monochromator bandpass, the rate of electronic energy transfer cannot be neglected.

Garland and Crosley[36] have measured the ratio of electronic energy transfer rate to the quenching rate for the $A^2\Delta(v'{=}0)$ and $A^2\Delta(v'{=}1)$ states and report values for E/Q of

17

0.025 ± 0.004 and 0.10 ± 0.02, respectively. The variation of E/Q as a function of N' was not statistically significant for these states. Finally, with $B_{eg} = (2J_g + 1/2J_e + 1)B_{ge}$, Eq. (4) reduces to

$$I_{LIF} = Cf_B(v'' = 0, J'')N_t \frac{A(IB)}{1.025\,Q(v' = 0) + IB\left[1 + (2J_g + 1/2J_e + 1)\right] + A} \qquad (5)$$

for LIF via the $A^2\Delta$-$X^2\Pi$ (0,0) band, and

$$I_{LIF} = Cf_B(v'' = 1, J'')N_t \frac{A(IB)}{1.10\,Q(v' = 1) + IB\left[1 + (2J_g + 1/2J_e + 1)\right] + A} \qquad (6)$$

for LIF via the $A^2\Delta$-$X^2\Pi$ (1,1) band where A is the Einstein emission coefficient, $A = A(1,1) = A(0,0)$, and B is the Einstein absorption coefficient, $B = B(1,1) = B(0,0)$. Equations (5) and (6) are used to relate the integrated LIF signal intensities to concentrations.

V. RESULTS AND DISCUSSION

A. CH Concentration Profiles

Emission from the CH radical is responsible for the blue coloration of hydrocarbon flames and essentially defines the reaction zone of these combustion systems. This emission originates primarily from chemiluminescence of $CH^*(A^2\Delta)$ produced from the reactions[26]

$$
\begin{array}{lr}
C_2 + OH = CH^* + CO & \text{(major)} \\
C_2H + O = CH^* + CO & \text{(major)} \\
C_2H + O_2 = CH^* + CO_2 & \text{(minor)}
\end{array}
$$
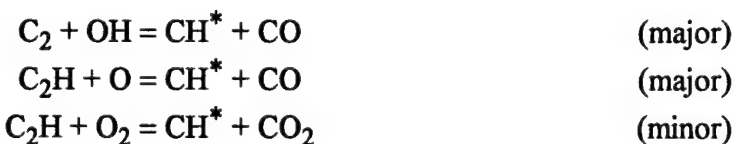
as opposed to thermally excited CH. The CH^* concentration, however, is much lower than the CH concentration, $N[CH^*]/N[CH] \sim 10^{-3}$, and thus justifies the approximation in section III that $\Delta N \sim N_g(v'', J'')$. Although this emission is abundant and easily detected, the CH molecules in the $A^2\Delta$ state are not thermalized, and rovibrational distributions are more indicative of the exothermicity of the above reactions rather than the translational temperature of the flame. In the flame studied here the CH^* emission outlines a small conical blue primary reaction zone, of 1.2 mm diameter and 1.6 mm in height, and a diffuse blue-green secondary reaction zone of approximately 6 mm in height.

18

Relative CH ground-state concentration information is obtained by measuring the DFWM and LIF integrated intensities of the four R(8) transitions as a function of height in the flame. The Boltzmann factors for the $N''=8$ levels of the CH $X^2\Pi$ state are relatively constant for temperatures ranging from 2300-3300 K, i.e., the integrated line intensities of transitions originating from these levels are weak functions of temperature. Therefore, the relative [CH($v''=0$, $N''=8$)] concentration profiles are representative of the CH relative concentration profile and can be obtained directly from the integrated line intensities of individual fine-structure components of transitions originating from $v''=0$, $N''=8$. From Eq. (1), the relative DFWM concentration profile can be obtained simply and is given by

$$\frac{N[CH(y)]}{N[CH(y=y_{max})]} = \frac{[I_{DFWM}(y)]^{1/2}}{[I_{DFWM}(y=y_{max})]^{1/2}}. \qquad (7)$$

Likewise, the LIF concentration profile is obtained from Eq. (5) and is given by

$$\frac{N[CH(y)]}{N[CH(y=y_{max})]} = \frac{I_{LIF}(y)}{I_{LIF}(y=y_{max})}. \qquad (8)$$

In both Eqs. (7) and (8), y_{max} is the position above the burner nozzle of maximum CH concentration. In addition, the DC level of the LIF signal is recorded at each position which provides a measure of the CH* emission from the flame. The emission is normalized at the same position as the LIF profile, $y = y_{max}$ (LIF), and is shown with the DFWM and LIF concentration profiles in Fig. 4. Each data point in Fig. 4 represents the average of the normalized profile for all four fine-structure components. The DFWM profile has been shifted by 160 µm to longer distance (approximately 20% of the beam waist) with respect to the LIF profile to give the best agreement. Because of the quadratic fall off of DFWM signal strength with concentration, the DFWM data points for positions greater than 2.5 mm are omitted. The first point in the emission profile is higher than the DFWM and LIF profiles because of laser light scattering from the burner nozzle. This is the only data point affected in this manner because all other points are at least one beam waist from the nozzle.

The spatial resolution of the LIF and emission measurements is determined by the magnification of the imaging system and the monochromator slits and is 50 µm x 100 µm (width x height). The DFWM profile has a spatial resolution limited by the overlap region of the three beams each having a full-width-at-half-maximum of 470 µm. Under these conditions, both the LIF and DFWM signals spatially average over species concentration and temperature gradients, and therefore represent the average CH concentration as a function of height. The distance between points in the spatial profile is 250 µm (height) as

FIG. 2.4. Relative CH concentration profile obtained by DFWM, LIF and CH^* ($A^2\Delta$) emission as a function of height above the burner nozzle. The CH concentration reaches a maximum in the primary reaction zone, region 1, and extends into the secondary reaction zone, region 2, as a result of excess fuel and fuel fragments reacting with diffused oxygen from the laboratory air.

Distance Above Burner Nozzle (mm)

Relative CH Concentration

Region 2
Region 1
Burner Nozzle
Region 1
Region 2
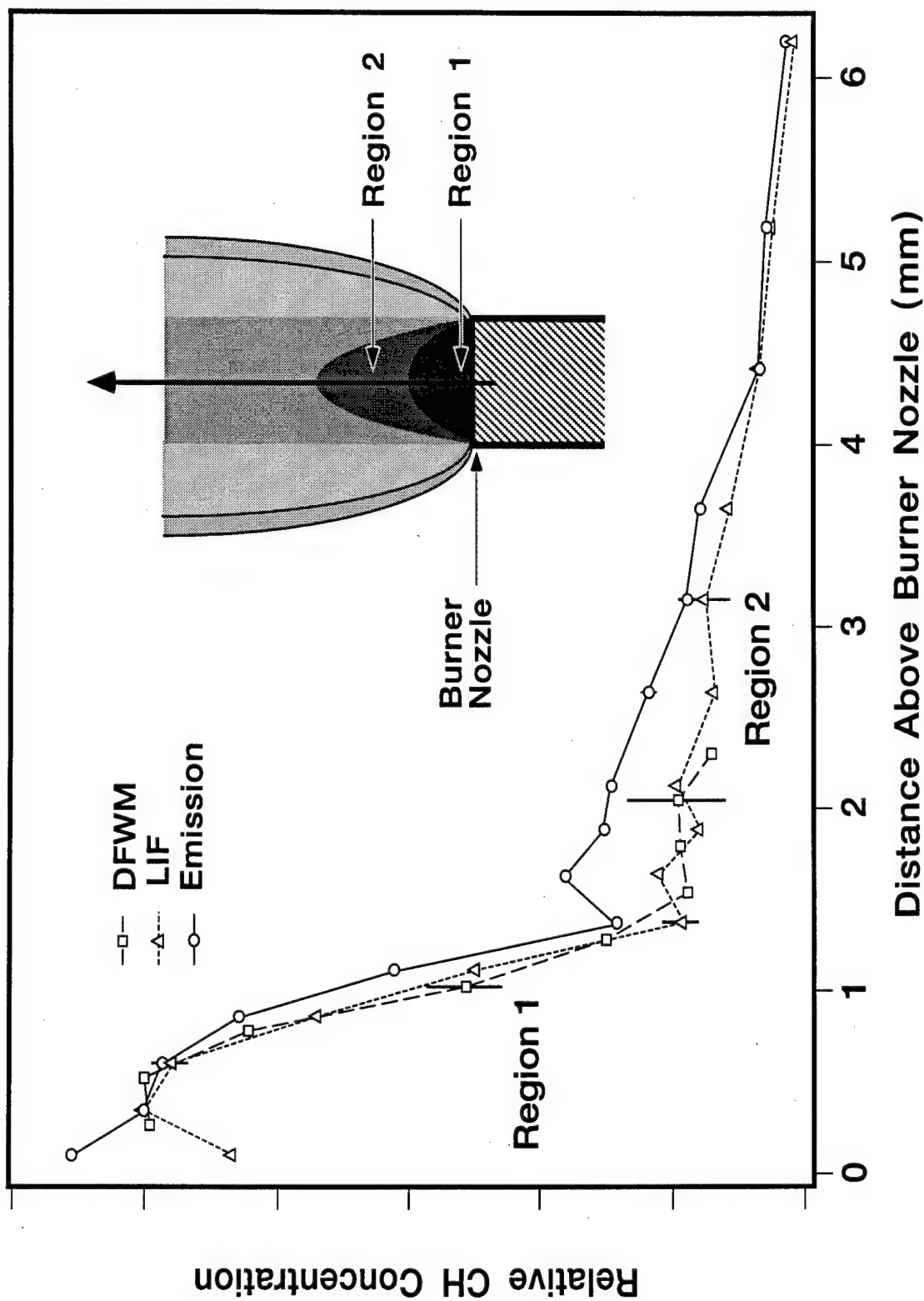
DFWM
LIF
Emission

measured by a micrometer. The DFWM profile is not significantly broadened with respect to the LIF profile obtained at a spatial resolution more than 2 times smaller than the step size. This suggests that the effective interaction diameter of the DFWM beams is on the order of 250 μm.

There is good agreement between the DFWM, the LIF, and the emission profiles which show the CH concentration increasing to a maximum in the primary reaction zone and then rapidly decreasing at the boundary between the primary and secondary reaction zones. This profile defines the primary reaction zone, region 1, and the small hump at 1.6 mm in the CH* emission marks its boundary. Since the flame is fuel rich, $\Phi = 2.64$ for $R = 0.947$, the CH concentration extends past the primary reaction zone to the secondary reaction zone, region 2, of the flame owing to excess fuel and fuel fragments reacting with oxygen that has diffused into the flame from the surrounding laboratory air.

B. CH Vibrational Temperatures

In calculating the CH vibrational temperatures, we take advantage of the fact that the (0,0) and (1,1) bands have the same transition probabilities,[31] and that the ratio of the rotational energy transfer rate, R, to the to the quenching rate, Q, for a given N' is nearly the same for the $v'=0$ and $v'=1$ levels of the $A^2\Delta$ state. For example, Garland and Crosley[36] report a R/Q value of 2.4 ± 0.1 for the $N'=6$, $v'=0$ level and 2.8 ± 0.2 for the $N'=6$, $v'=1$ level of the $A^2\Delta$ state. These R/Q values suggest that the saturation properties of the (0,0) and (1,1) transitions are nearly identical. Furthermore, when specific fine-structure components of these bands are compared, i.e., the $R_{1e}(v''=0)$ is compared to the $R_{1e}(v''=1)$, any effects arising from polarization will affect both transitions identically and cancel. Therefore, from Eq. (1) we can write

$$\frac{I_{DFWM}\left(R_{1,2;e,f};v''=1\right)}{I_{DFWM}\left(R_{1,2;e,f};v''=0\right)} = \frac{\left[N\left(F_{1,2;e,f};v''=1\right)\right]^2}{\left[N\left(F_{1,2;e,f};v''=0\right)\right]^2}, \tag{9}$$

where $R_{1,2;e,f}$ and $F_{1,2;e,f}$ correspond to the particular R-branch transition originating in a specific spin-orbit state, either $F_1(J''=N''+1/2)$ or $F_2(J''=N''-1/2)$, and Λ-doublet level, either e or f. Notice that since the transition probabilities, degeneracies, and collisional widths are the same, the DFWM signal ratio depends exclusively on the square of the concentration ratio.

The LIF expressions can be simplified in a like manner. The first reduction results from the fact that the spectra are recorded at approximately 8 times the LIF saturation

22

intensity, which is discussed in Sec. VC In this case the small electronic energy transfer rate corrections to the LIF intensity in the denominators of Eqs. (5) and (6) can be ignored. Furthermore, since the rotational energy spacing of the $v'=0$ and $v'=1$ levels are very similar, and the R/Q ratios are almost equivalent for a given N' in either $v'=0$ or $v'=1$, we make the assumption that $Q(A^2\Delta;v'=0) = Q(A^2\Delta;v'=1)$. In this case, the ratio of Eq. (6) to Eq. (5) reduces to

$$\frac{I_{LIF}\left(R_{1,2;e,f};v''=1\right)}{I_{LIF}\left(R_{1,2;e,f};v''=0\right)} = \frac{N\left(F_{1,2;e,f};v''=1\right)}{N\left(F_{1,2;e,f};v''=0\right)}, \tag{10}$$

where $R_{1,2;e,f}$ and $F_{1,2;e,f}$ have the same definitions as in Eq. (9). Note that the LIF signal ratio depends only on the concentration ratio.

For an assumed Boltzmann distribution, a vibrational temperature can be obtained directly from the ratio of the DFWM intensities of the same fine-structure component of the (0,0) and (1,1) transitions by

$$\frac{\left[I_{DFWM}\left(R_{1,2;e,f};v''=1\right)\right]^{1/2}}{\left[I_{DFWM}\left(R_{1,2;e,f};v''=0\right)\right]^{1/2}} = \exp(-\Delta E_{VIB} / k_B T_V), \tag{11}$$

and from the LIF intensities by

$$\frac{I_{LIF}\left(R_{1,2;e,f};v''=1\right)}{I_{LIF}\left(R_{1,2;e,f};v''=0\right)} = \exp(-\Delta E_{VIB} / k_B T_V), \tag{12}$$

where ΔE_{VIB} is the energy difference between $v''=1$ and $v''=0$ for a given Λ component and J'', k_B is the Botlzmann constant, and T_V is the vibrational temperature. Spectra like the one shown in Fig. 3 were recorded at the region of maximum CH concentration, and Eqs. (11) and (12) were used to obtain CH vibrational temperatures. An average of six scans gave a ratio of $N[CH(v''=1)]/N[CH(v''=0)]$ equal to 0.260 ± 0.015 for DFWM and 0.230 ± 0.012 for LIF, which correspond to vibrational temperatures of 2882 ± 123 K and 2642 ± 99 K, respectively. The reported error bars represent one standard deviation and are more indicative of the precision of the measurements rather than their accuracy considering the fact both the DFWM and LIF spectra spatially average over concentration and temperature in the flame. This is perhaps the chief reason for any difference between the results, since the DFWM and LIF spectra represent spatial averages arising from different sampling volumes. The relative CH concentration measurements are not as sensitive to this effect because the comparison is between relative values of the same measurement (DFWM or LIF) over the same sampling volume.

23

These vibrational temperatures can be used in conjunction with the estimated CH concentration of 30 ppm to determine the sensitivity. For an average temperature of 2760 K, 30 ppm corresponds to a CH number density of 8 x 10^{13} molecules/cm^3 (8 x 10^{11} molecules/cm^3 per quantum state). The data shown in Fig. 3 represents a signal-to-noise ratio approaching 500:1, resulting in a sensitivity limit (signal-to-noise ratio of 1) for CH of 4x10^{12} molecules/cm^3 (4x10^{10} molecules/cm^3 per quantum state) under the present conditions. In reporting this number one must consider the fact that the actual flame dimensions limit the interaction length, L, of Eq. (1) to approximately 1 mm. The coherence length of the laser, on the other hand, is on the order of a centimeter, and at 2° incidence angle, the effective overlap length of the beams is approximately 15 mm. This implies that in an environment that does not limit the interaction length, the DFWM signal intensity could increase from the L^2 dependence by as much as 2 orders magnitude. Since the DFWM signal increase quadratically with concentration, an increase in signal intensity by two orders of magnitude results in only an order of magnitude increase in sensitivity. Therefore, a more reasonable estimate of the CH detection limit is 4x10^{11} molecules/cm^3 (4x10^9 molecules/cm^3 per quantum state).

C. DFWM and LIF Power Dependence

The effect of laser power on DFWM and LIF integrated signal intensities for the R(8) transition of the (0,0) band was determined for pump beam energies of 1.3 to 81.3 μJ (spectral intensities of 0.17 to 11.2 x 10^6 W/cm^2-cm^{-1}). This range corresponds to total energies of all three beams from 2.8 to 183 μJ (spectral intensities of 0.39 to 25.2 x 10^6 W/cm^2-cm^{-1}). Figures 5a and 6a show the DFWM and LIF integrated signal intensities as a function of total laser energy (bottom axis) and spectral intensity (top axis). Figures 5b and 6b are log-log plots for DFWM and LIF, respectively. The integrated intensities in these graphs represent an average of the integrated signal intensity of the four-fine structure components weighted linearly (LIF) and quadratically (DFWM) by the relative Boltzmann factors using an average vibrational temperature of 2670 K. Since the term energies only vary by 4 cm^{-1} in 1014 cm^{-1} for the $F_{1e,f}(J''=N''+1/2)$ and $F_{2e,f}(J''=N''-1/2)$ components,[37] the normalization is determined primarily by the relative degeneracy factors (2J''+1).

The DFWM integrated signal intensities of Fig. 5a are linear over a wide range of laser intensities. The slope of the line in Fig. 5b resulting from a linear least squares fit of the data between 28.1 and 154.7 μJ (3.9 and 21.3 x 10^6 W/cm^2-cm^{-1}) is 0.87 ± 0.07
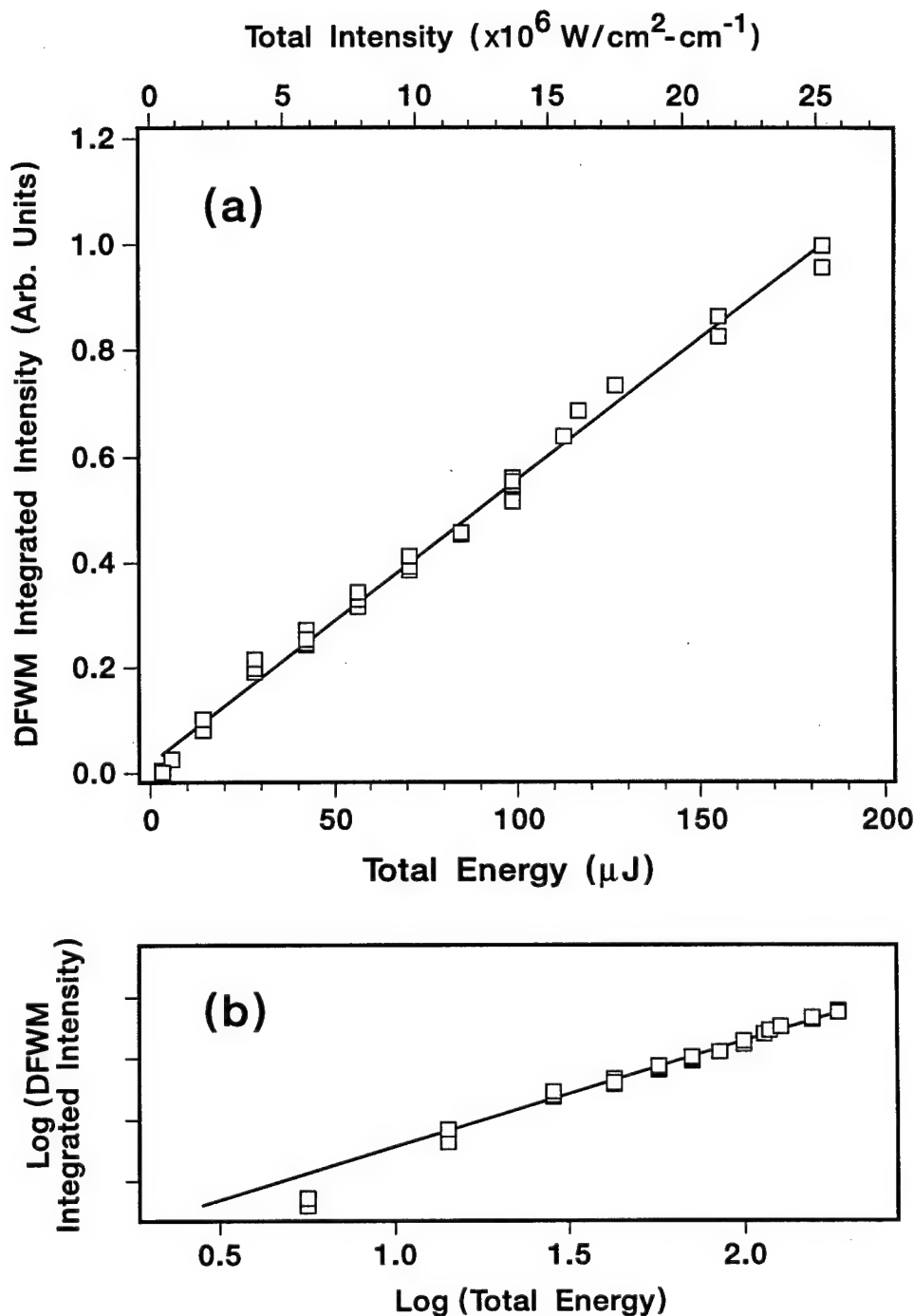
FIG. 2.5. (a) DFWM integrated signal intensity as a function of total laser energy (bottom) and spectral intensity (top), and (b) Log[DFWM integrated intensity] vs. Log[total energy]. The DFWM integrated signal intensity is linear over a large range of laser energies. The slope of the line in (b) resulting from a linear least squares fit of the data between 28.1 and 154.7 μJ (3.9 and 21.3 x 10^6 W/cm^2-cm^{-1}) is 0.87 $\pm$ 0.07 corresponding to an average power dependence in this region of $I_{DFWM} \propto I^{0.9}$.
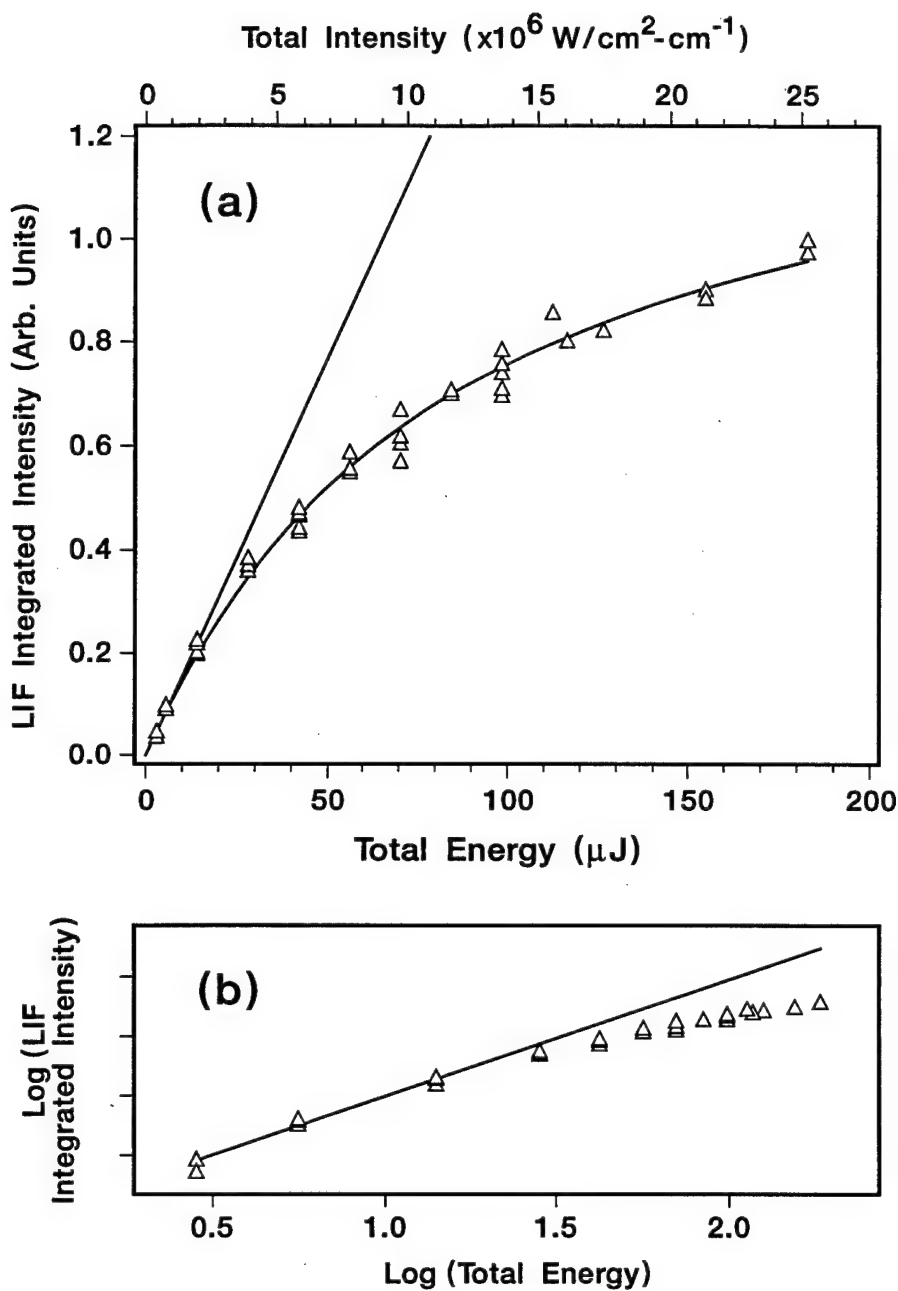
FIG. 2.6. (a) LIF integrated signal intensity as a function of total laser energy (bottom) and spectral intensity (top), and (b) Log[LIF integrated intensity] vs. Log[total energy]. The line resulting from a linear fit to the data points below 14.1 μJ (1.9 x 10^6 W/cm^2-cm^{-1}) is shown in (a) as well as a fit of the data to the power dependence predicted by Eq. (5). The LIF integrated signal intensities in (a) show a deviation from linearity beginning at 14.1 μJ (1.9 x 10^6 W/cm^2-cm^{-1}) resulting from saturation. The slope of the line shown in (b) for the data points below 14.1 μJ (1.9 x 10^6 W/cm^2-cm^{-1}) is 0.98 ± 0.05 indicating at most only a slight degree of saturation in this energy regime.

corresponding to an average power dependence in this region of $I_{DFWM} \propto I^{0.9}$. This is significantly less than the I^3 power dependence for unsaturated DFWM. The LIF integrated signal intensities in Fig. 6a show a deviation from linearity beginning at 14.1 µJ (1.9×10^6 W/cm^2-cm^{-1}). The slope of Fig. 6b for the points below this energy is 0.98 ± 0.05 indicating that the LIF signals are at most only slightly saturated in this intensity regime. Bonczyk and Shirley[28] have measured the LIF saturation intensity for CH in an atmospheric-pressure oxyacetylene flame to be 0.34×10^6 W/cm^2-cm^{-1}, and Takubo, Yano, Matsuoka, and Shimazu[38] measured 0.33×10^6 W/cm^2-cm^{-1} in an atmospheric-pressure propane-air flame. These results are consistent with the data of Figs. 6a, and 6b which suggest that saturation for CH in an atmospheric-pressure flame occurs at spectral intensities on the order of 0.5×10^6 W/cm^2-cm^{-1}.

Another indication of saturation is power broadening of spectral lines. Figure 7 shows the line widths (fwhm) for both the DFWM and LIF spectral lines as a function of total energy (bottom) and spectral intensity (top) with each data point representing an average over all four fine-structure components. Both the DFWM and the LIF line widths are power dependent even at the lowest total energies studied 2.8 µJ (0.39×10^6 W/cm^2-cm^{-1}) In Fig. 7, it is immediately apparent that the DFWM line widths are substantially narrower than the Doppler-broadened LIF line widths at low laser intensities, and that at high laser intensities, the power-broadened line shapes of both techniques are approximately equal. The sub-Doppler DFWM line shape is limited by the large laser bandwidth of 0.18 cm^{-1} as opposed to the estimated collisional width (fwhm) of 0.02 cm^{-1}.[39] At total laser energies lower than 28.1 µJ (3.9×10^6 W/cm^2-cm^{-1}) the DFWM line width is smaller than the laser bandwidth and has a value of 0.12 ± 0.02 cm^{-1} at the lowest total laser energy.

Figure 8a shows the LIF and DFWM line shapes for the $R_{1e}(8)$ transition at a total laser energy of 28.1 µJ (3.9×10^6 W/cm^2-cm^{-1}). The LIF line shape is Gaussian owing to the large Gaussian laser bandwidth of 0.18 cm^{-1} and Doppler width of 0.24 cm^{-1} (2760 K) compared to the collisional width of 0.02 cm^{-1}. The DFWM line shape is fit in Fig. 8a to a Lorentzian-cubed line shape. Figure 8b shows the best fit results to the DFWM line shape for a Gaussian, Lorentzian, and Lorentzian-cubed profile. The Lorentzian-cubed profile gives the best fit to the line shape in agreement with the AL model predictions,[3,35] although experimental conditions appear to be outside of the model.
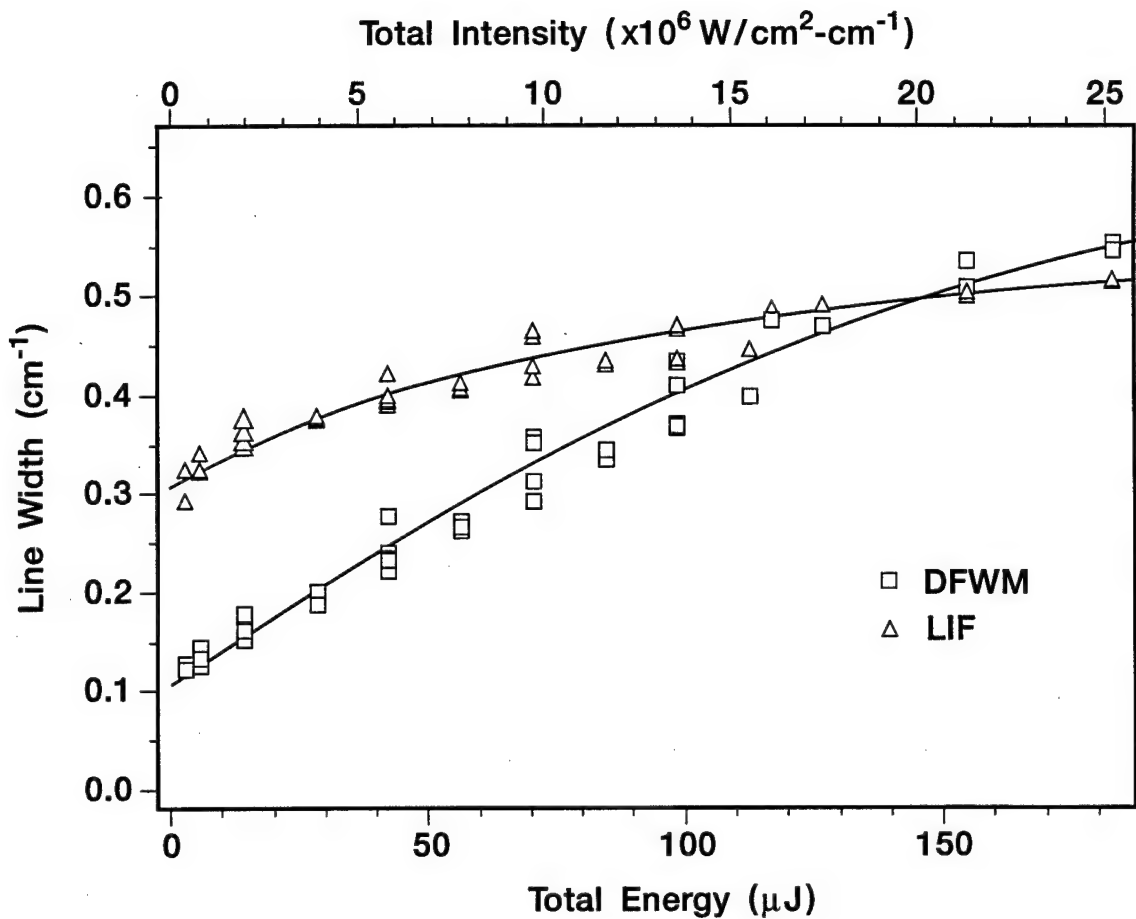
FIG. 2.7. DFWM and LIF line widths (fwhm) as a function of total laser energy (bottom) and spectral intensity (top). Curves are drawn as a guide to the eye. At low energy, the sub-Doppler DFWM line widths are significantly narrower than the Doppler-broadened LIF line widths, and at high laser intensities, both techniques have comparable power-broadened line widths. The DFWM line width is smaller than the laser bandwidth (0.18 cm^{-1}) for total laser energies lower than 28.1 μJ (3.9 x 10^6 W/cm^2-cm^{-1}) and has a minimum value of 0.12 ± 0.02 cm^{-1} at 2.8 μJ (0.39 x 10^6 W/cm^2-cm^{-1}).

FIG. 2.8. (a) DFWM and LIF line shapes for the $R_{1e}(8)$ transition of the CH $A^2\Delta - X^2\Pi$ (0,0) band at 28.1 μJ (3.9 x 10^6 W/cm^2-cm^{-1}). The DFWM line shape is fit to a Lorentzian-cubed profile as predicted by the AL model, and the LIF line shape is fit to a Gaussian profile owing to the large Gaussian widths (0.18 cm^{-1} laser bandwidth and 0.24 cm^{-1} Doppler width). (b) Comparison of the best fit results to the DFWM line shape for a Gaussian, Lorentzian, and Lorentzian-cubed profile.

(a) DFWM 0.19 cm^{-1} LIF 0.37 cm^{-1}

(b) Lorentzian-cubed / Gaussian / Lorentzian

Wavelength (nm)
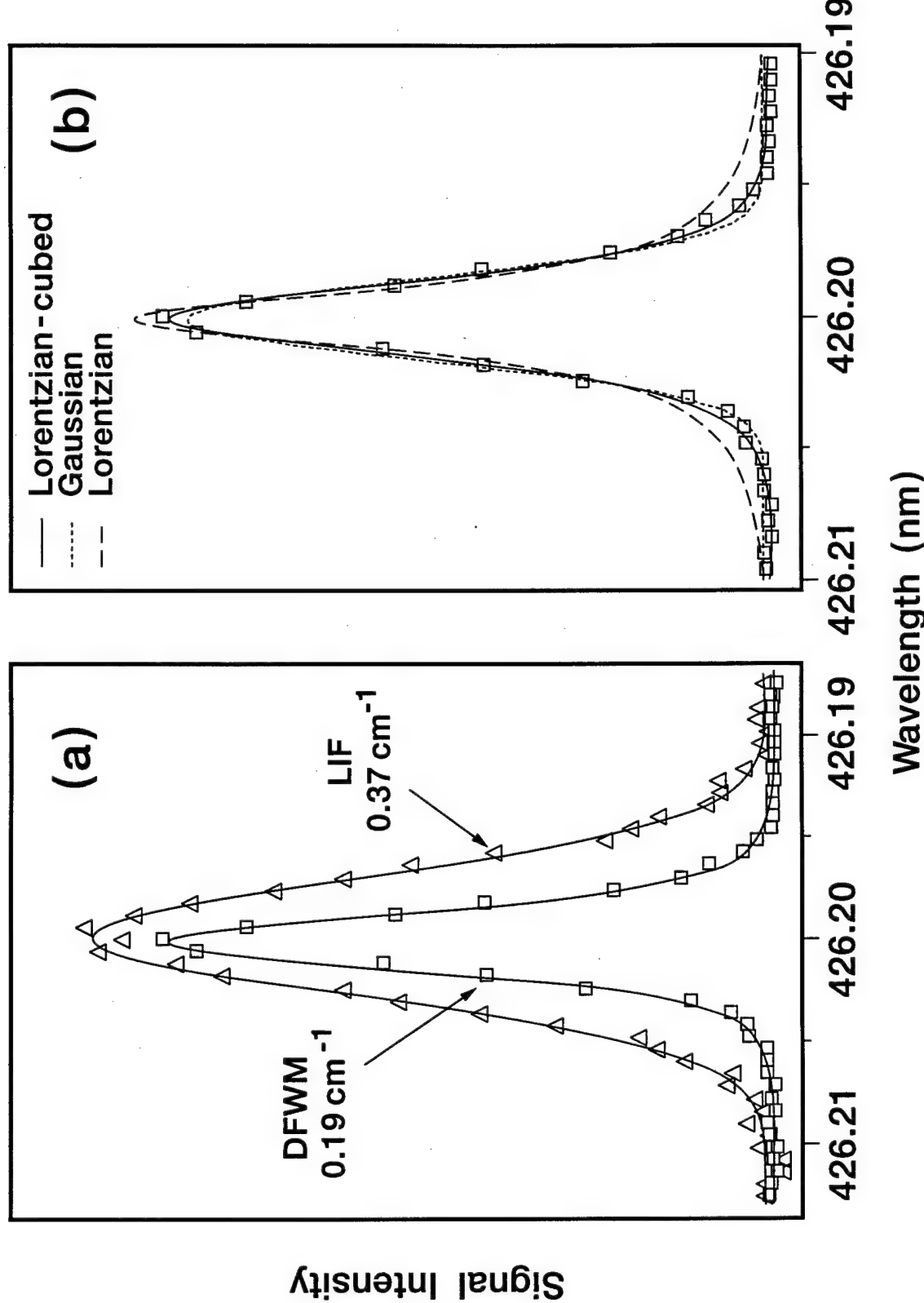
Signal Intensity

The DFWM integrated signal intensities are essentially linear in laser energy over the range (two orders of magnitude) studied. However, if the line-center peak height as a function of pump laser intensity is plotted, the effect of saturation is more apparent. See Fig. 9. The line-center signal intensity rolls off very rapidly to nearly a constant value as predicted by Eq (1). From Eq. (1), the DFWM line-center power dependence is of the form

$$I_{DFWM} \propto \frac{I^3/I_{sat}^2}{\left(1+4 I/I_{sat}\right)^3} \tag{13}$$

where I is the intensity of the forward pump field and $I_f = I_b = 4 I_p$ in our experimental configuration. The line-center peak heights were fit to Eq. (13), and the fit is also shown in Fig. 9. The fit gave an experimentally determined value of $I_{sat}^{ex} = 11.7 \pm 1.1$ μJ $(1.61 \pm 0.15 \times 10^6$ W/cm^2-cm^{-1}).

Contrary to naive first impressions, the sensitivity of DFWM does not increase without limit as a function of laser power. A measure of the signal-to-noise ratio in these experiments is the DFWM reflectivity, R_{AL},[3] which can be obtained by rearranging Eq. (1) to give

$$R_{AL} = \frac{I_{DFWM}}{I_p} = 4\alpha_o^2 L^2 \frac{\left(I/I_{sat}\right)^2}{\left(1+4 I/I_{sat}\right)^3} \tag{14}$$

Equation (14) represents the ratio of the DFWM signal intensity to the input probe field intensity, and this equation is a good measure of the signal-to-noise ratio because scattered laser light from the probe beam is the largest source of noise. If only the laser intensity is varied in a series of experiments, as was done for the power dependence of Fig. 9, Eq. (14) can be simplified to give

$$R_{AL} = \frac{I_{DFWM}}{I_p} = \eta \frac{\left(I/I_{sat}\right)^2}{\left(1+4 I/I_{sat}\right)^3} \tag{15}$$

where η is a combined constant that represents the DFWM signal intensity for a given set of conditions and can be measured experimentally. The DFWM reflectivity curve was generated using Eq. (15) and the experimentally determined value of I_{sat}, and the data of Fig. 9 was divided by the probe field intensity. The theoretical and experimental reflectivity has been scaled to a value of η defined here as

$$\eta = 125 \left(\frac{\text{no. signal photons collected}}{\text{collection efficiency}} \right) \Big/ \left(\text{no. input probe photons} \right) \tag{16}$$

31

FIG. 2.9. DFWM line-center signal intensity as a function of pump beam energy (bottom) and spectral intensity (top). The error bars are $\pm$ 10 % resulting primarily from the shot-to-shot laser energy fluctuations. The line-center peak heights were fit to the power dependence predicted by Eq. (13). The fit (solid curve) gave an experimentally determined value of $I_{sat}^{ex} = 1.7 \pm 1.1$ μJ (1.61 ± 0.15 x 10^6 W/cm^2-cm^{-1}).
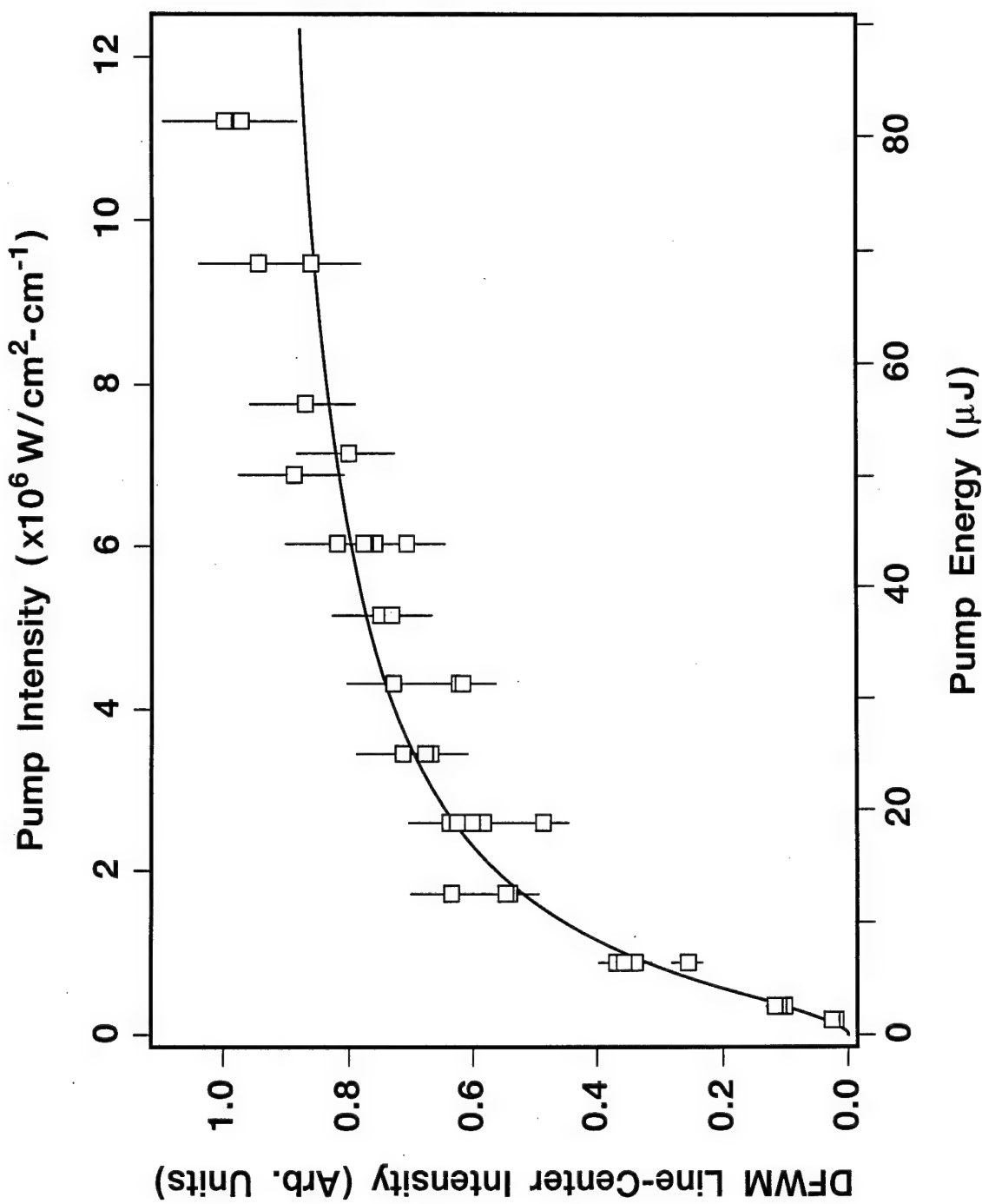
FIG. 2.10. DFWM reflectivity, R_{AL}, as a function of I / I_{sat} for the value of $I_{sat}^{ex} = 1.61 \pm 0.15 \times 10^6$ W/cm^2-cm^{-1} (11.7 ± 1.1 µJ) determined from the fit shown in Fig. 9. The reflectivity has been scaled to an experimentally determined value of $\eta = 1.14 \times 10^{-7}$ defined by Eq. (16). The reflectivity is indicative of the signal-to-noise ratio for these experiments and is a maximum for laser intensities approximately equal to I_{sat}^{ex}.

Figure showing DFWM Reflectivity (R) versus I/I_{sat}.
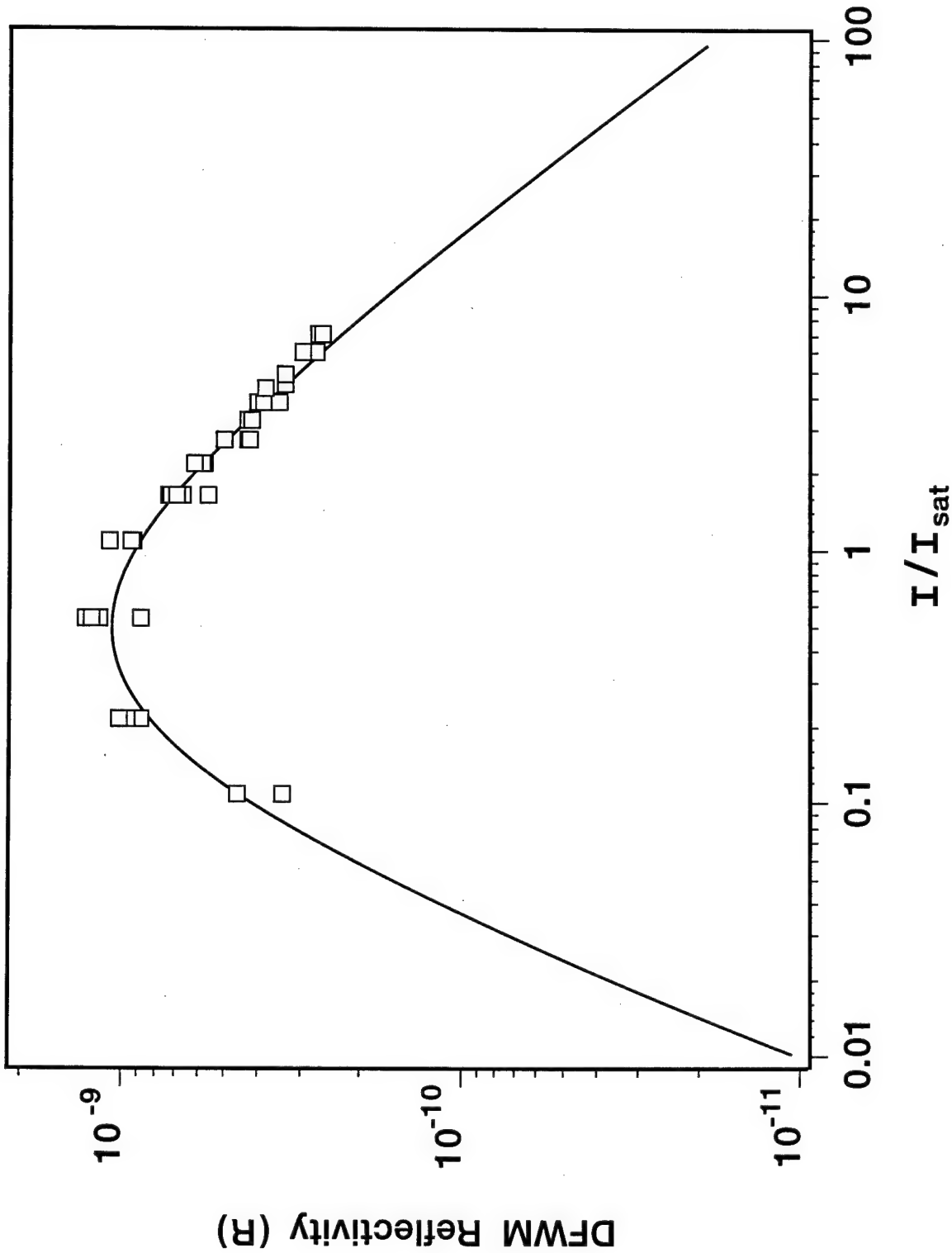
that was measured at $I / I_{sat}^{ex} = 1$ and are plotted as a function of I / I_{sat} in Fig. 10. Figure 10 shows that the maximum reflectivity, hence signal-to-noise ratio, is obtained at spectral intensities approximately equal to I_{sat}. The highest signal-to-noise ratios also were observed experimentally at these energies. As the laser intensity (energy) increases above I_{sat}, the line-center signal intensity becomes constant, the peak profiles power broaden, and the scattered-light-noise-baseline increases. The combined result is that the signal-to-noise ratio decreases. Working at powers much greater than I_{sat} will not improve the detection limit of DFWM, but will only diminish the advantages of the technique, such as narrow sub-Doppler line shapes.

VI. CONCLUSIONS

In this chapter we report the first DFWM study of the CH radical and have demonstrated that trace flame species can be detected at atmospheric pressure with high sensitivity using DFWM. Accurate CH concentration profiles and vibrational temperatures with regard to LIF results have been obtained without having to make corrections for collisional processes. At atmospheric pressure the DFWM and LIF intensities are comparable; however, at higher pressures DFWM should prove to be more sensitive than LIF because of the effect of quenching collisions on the LIF signal. An additional advantage of DFWM is that it generates a coherent signal beam that can be remotely detected with high efficiency. This attribute enables nonintrusive investigation of many important chemical environments that suffer from limited optical access, high levels of emitted radiation, and high pressures, such as plasmas, flashes, flames, and discharges. DFWM will be especially advantageous for the detection of molecular species that do not fluoresce or whose fluorescence is complicated by collisional effects.

References

(1)   A. C. Eckbreth, *Laser Diagnostics for Combustion Temperature and Species* (Abacus, Cambridge, MA, 1988).

(2)   A. C. Eckbreth and J. H. Stufflebeam, *Mater. Res. Soc. Symp. Proc.* **117**, 217 (1988).

(3)   R. L. Abrams, J. F. Lam, R. C. Lind, D. G. Steel and P. F. Liao, in *Optical Phase Conjugation*, edited by R. A. Fisher (Academic Press, New York, 1983), Chapter 8.

(4)   J. Pender and L. Hesslink, *Opt. Lett.* **10**, 264 (1985).

(5)   J. M. Ramsey and W. B. Whitten, *Anal. Chem.* **59**, 167 (1987).

(6)   W. G. Tong, J. M. Andrews and Z. Wu, *Anal. Chem.* **59**, 896 (1987).

(7)   W. G. Tong and D. A. Chen, *Appl. Spectrosc.* **41**, 586 (1987).

(8)   D. A. Chen and W. G. Tong, *J. Anal. At. Spectrom.* **3**, 531 (1988).

(9)   J. M. Andrews and W. G. Tong, *Spectrochim. Acta* **44B**, 101 (1989).

(10) G. A. Luena and W. G. Tong, *Appl. Spectrosc.* **44**, 1668 (1990).

(11) Z. Wu and W. G. Tong, *Anal. Chem.* **63**, 899 (1991).

(12) Z. Wu and W. G. Tong, *Anal. Chem.* **63**, 1943 (1991).

(13) Z. Wu and W. G. Tong, *Anal. Chem.* **61**, 998 (1989).

(14) P. Ewart and S. V. O'Leary, *Opt. Lett.* **11**, 279 (1986).

(15) T. Dreier and D. J. Rakestraw, *Opt. Lett.* **15**, 72 (1990).

(16) D. J. Rakestraw, R. L. Farrow and T. Dreier, *Opt. Lett.* **15**, 709 (1990).

(17) T. Dreier and D. J. Rakestraw, *Appl. Phys. B* **50**, 479 (1990).

(18) R. L. Farrow, D. J. Rakestraw and T. Dreier, *J. Opt. Soc. Am. B* **9**, 1770 (1992).

(19) R. L. Vander Wal, B. E. Holmes, J. B. Jeffries, P. M. Danehy, R. L. Farrow and D. J. Rakestraw, *Chem. Phys. Lett.* **191**, 251 (1992).

(20) R. L. Vander Wal, R. L. Farrow and D. J. Rakestraw, *Twenty-Fourth Symposium (International) on Combustion,* **The Combustion Institute, Pittsburgh, PA**, 1653 (1992).

(21) Q. Zhang, S. A. Kandel, T. A. W. Wasserman and P. H. Vaccaro, *J. Chem. Phys.* **96**, 1640 (1992).

(22) D. R. Crosley, *Opt. Eng.* **20**, 511 (1981).

(23) K. J. Rensberger, J. B. Jeffries, R. A. Copeland, K. Kohse-Hoinghaus, M. L. Wise and D. R. Crosley, *Appl. Opt.* **28**, 3556 (1989).

(24) J. M. Khosrofian and B. A. Garetz, *Appl. Opt.* **22**, 3406 (1983).

(25) A. E. Siegman, *Lasers* (University Science Books, Mill Valley, CA, 1986).

(26) R. G. Joklik microfilm, Thesis, Univ. of California, Berkeley, 1985. Avail. Univ. Microfilms Int. Order No. DA8610071 From: Diss. Abstr. Int. B 1986, 47 (3), 1212.

(27) P. F. Jessen and A. G. Gaydon, *The Twelfth Symposium (International) on Combustion,* **The Combustion Institute, Pittsburgh, PA**, 481 (1969).

(28) P. A. Bonczyk and J. A. Shirley, *Combust. Flame* **34**, 253 (1979).

(29) Y. Matsui, A. Yuuki, M. Sahara and Y. Hirose, *Jpn. J. of Appl. Phys.* **28**, 1718 (1989).

(30) P. F. Bernath, C. R. Brazier, T. Olsen, R. Hailey, W. T. M. L. Fernando, C. Woods and J. L. Hardwick, *J. Molec. Spectrosc.* **147**, 16 (1991).

(31) N. L. Garland and D. R. Crosley, *J. Quant. Spectrosc. Radiat. Transfer* **33**, 591 (1985).

(32) J. Hinze, G. C. Lie and B. Liu, *Astrophys. J.* **196**, 621 (1975).

(33) R. L. Abrams and R. C. Lind, *Opt. Lett.* **2**, 94 (1978).

(34) Ibid., erratum **3**, 205 (1978).

(35) M. S. Brown and L. A. Rahn, *Opt. Lett.* **17**, 76 (1992).

(36) N. L. Garland and D. R. Crosley, *Appl. Opt.* **24**, 4229 (1985).

(37) P. F. Bernath, *J. Chem. Phys.* **86**, 4838 (1987).

(38) Y. Takubo, H. Yano, H. Matsuoka and M. Shimazu, *J. Quant. Spectrosc. Radiat. Transfer* **30**, 163 (1983).

(39) The collisional width was calculated using the energy transfer rates reported by the following references (See Chapter 4, Sec. IIC): R. J. Cattolica, D. Stepowski, D. Puecheberty and M. Cottereau, *J. Quant. Spectrosc. Radiat. Transfer* **32**, 363 (1984). N. L. Garland and D. R. Crosley, *Appl. Opt.* **24**, 4229 (1985). N. L. Garland and D. R. Crosley, *Chem. Phys. Lett.* **134**, 189 (1987). R. G. Joklik and J. W. Daily, *Combust. Flame* **69**, 211 (1987). K. J. Rensberger, M. J. Dyer and R. A. Copelend, *Appl. Opt.* **27**, 3679 (1988). D. E. Heard, J. B. Jeffries and D. R. Crosley, *Chem. Phys. Lett.* **178**, 533 (1991).

CHAPTER 3

Theoretical Development of the Reduction of DFWM Spectra to Relative Populations in the Weak-Field Limit

".... it may be remarked that the main object of physical science is not the provision of pictures, but is the formulation of laws governing phenomena and the application of these laws to the discovery of new phenomena. If a picture exists, so much the better; but whether a picture exists or not is a matter of only secondary importance. In the case of atomic phenomena no picture can be expected to exist in the usual sense of the word 'picture' by which is meant a model functioning essentially on classical lines. One may, however, extend the word 'picture' to include any way of looking at the fundamental laws which makes their self-consistency obvious. With this extension, one may gradually acquire a picture of atomic phenomena by becoming familiar with the laws of quantum theory."

P. A. M. Dirac

I. INTRODUCTION

LIF is a powerful spectroscopic technique for analyzing molecular species in experiments that range from chemical reaction dynamics to plasma physics. A common goal of these experiments is to extract accurate values for relative populations from the relative intensity distribution of the emitted light. Several authors have shown how the emitted light intensity depends on the excitation/detection geometry (polarization),[1-3] the temperature, pressure, and chemical composition of the experiment (collisional relaxation),[4-6] and the laser power employed (saturation).[7-9] In general, the population as well as the elements of the first- and second-rank multipole moments of the total angular momentum, called the orientation and the alignment, respectively, can be determined from low-pressure experiments performed under single-collision conditions. In collisionally dominated environments, however, the determination of these quantities becomes extremely difficult.

An appealing alternative approach to the study of collisionally dominated environments is DFWM.[10] DFWM uniquely provides information regarding the chemical composition, kinetics, and dynamics of environments that are inherently difficult to study because of radiant interference from the emission of excited species.[11] One of the most important features of DFWM is the large four-wave mixing enhancement exhibited when the laser frequency is tuned to a molecular one-photon resonance (this includes electronic, vibrational, and rotational transitions); this feature makes DFWM a very sensitive molecular probe. Other important features include sub-Doppler spectral resolution, excellent spatial and temporal resolution, imaging capabilities, nonintrusive detection, and remote sensing. Because of these attributes, the potential of DFWM spectroscopy to obtain chemical and dynamical information has generated much excitement. Like LIF, however, DFWM requires an understanding of polarization, collisional, and saturation effects before information can be extracted from the signal intensities.

At present, DFWM signal intensities are most commonly interpreted by applying the stationary absorber model proposed by Abrams and Lind,[10,12] which considers a nondegenerate two-level system in the presence of arbitrarily strong pump fields. This model accounts only for population contributions to the DFWM response and neglects contributions from orientation and alignment. This model's predictions have been applied with much success to relate saturated DFWM signal intensities to populations in experiments performed under collisionally dominated conditions.[11,13-16] Note, however, that signals from a single rotational branch and polarization configuration were used in

40

these experiments. These conditions serve to minimize the error introduced from applying this model to molecular systems with degenerate magnetic sublevels.[17]

To date, attempts to formulate a complete model that includes polarization, collisional, and saturation effects have been unsuccessful. Studies that emphasize saturation effects[18-27] are limited to level degeneracies in the range of 1 to 3. Even numerical approaches[28] are computationally impractical at present for level degeneracies typical of molecular species. Many authors[20,29-39] have thus resorted to perturbative treatments (no saturation) to gain insight into the DFWM response of degenerate systems.

The aim of this chapter is to present a theory of DFWM that can be used to interpret the spectra of molecular species. This goal is accomplished by deriving expressions via time-independent diagrammatic perturbation theory that account for the DFWM polarization, collisional, and velocity effects in the weak-field limit. In our treatment, we assume that the DFWM process couples levels of sharp (definite) angular momentum J (omitting nuclear spin). We consider three input fields of arbitrary polarization that interact with an isotropic sample to produce a fourth field. Therefore, our treatment is general in that it applies to molecular species for which J is a good quantum number. The general result is specialized to apply to circularly and linearly polarized fields that interact in nearly collinear phase matching geometries in collisional environments where the multipole moments of the total angular momentum distribution relax independently (isotropic relaxation) and at the same rate. Figure 1 shows the three specific geometries we treat. In the following chapter, we extend the key results presented here to interpret data taken under saturated conditions.

The remainder of this chapter is organized into four sections and one appendix. In Sec. II we present expressions for the DFWM signal intensity as a function of input polarization, collisional dephasing, and experimental geometry under the assumption that the rates of collisional relaxation of the population, the orientation, and alignment are the same. This section is intended as a guide for the experimentalist. In Sec. III we interpret the DFWM signal intensity, as has been done for LIF, in terms of the population, the orientation, and the alignment. In Sec. IV we compare our results with those of other treatments, and in Sec. V we present conclusions of our findings. In the Appendix expressions are presented for the polarization tensor products necessary to extend this treatment to other experimental configurations.

41
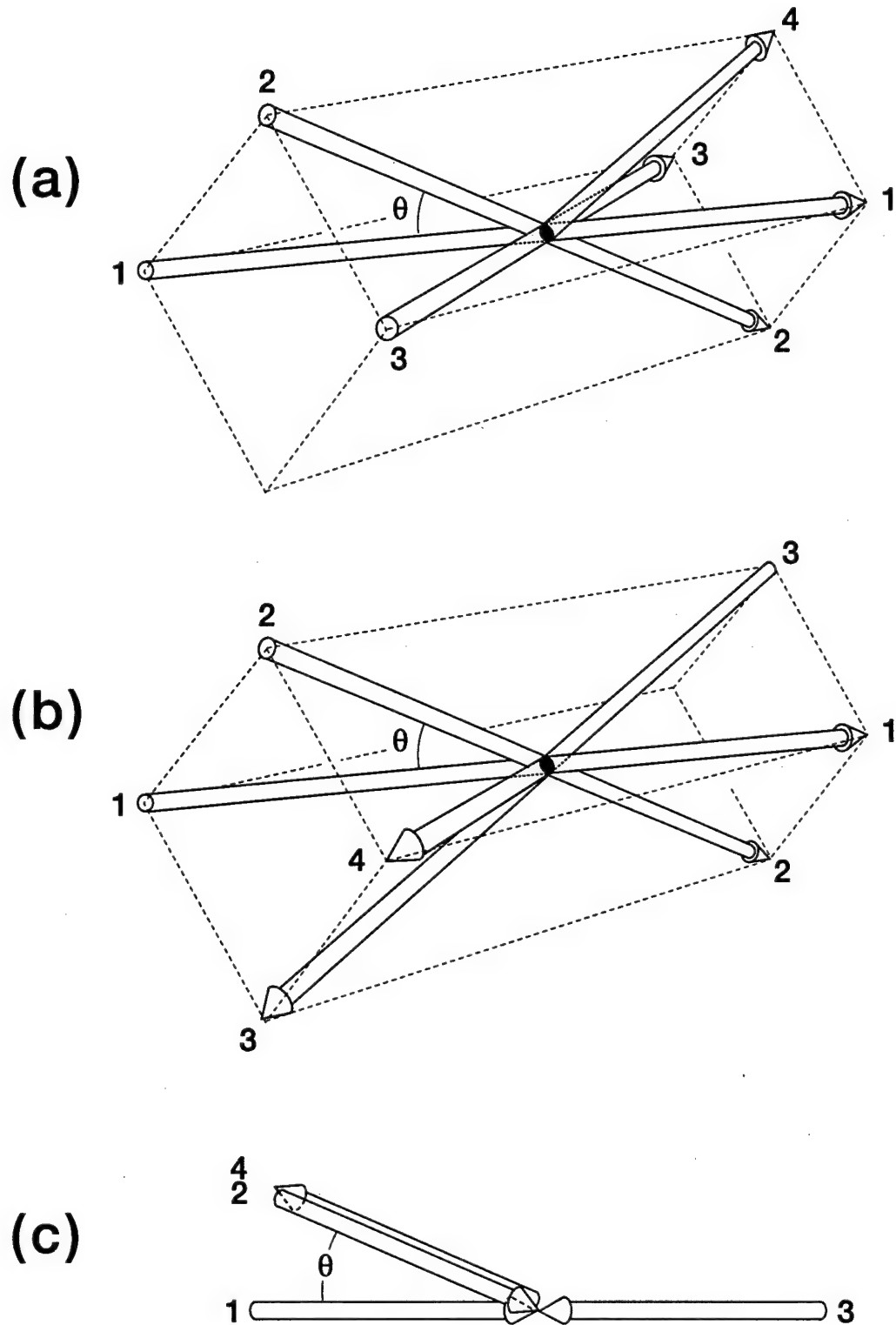
FIG. 3.1. Phase matching geometries: (a) Forward box, FB-DFWM; (b) Backward box, BB-DFWM; (c) Phase conjugate, PC-DFWM.

II. DEPENDENCE OF DFWM SIGNAL INTENSITIES ON POLARIZATION, COLLISIONS, AND PHASE MATCHING GEOMETRY

A. General Expressions and Discussion

In four-wave mixing three incoming waves with electric fields $E_1(r,t)$, $E_2(r,t)$, and $E_3(r,t)$, propagation vectors k_1, k_2, and k_3, and frequencies ω_1, ω_2, and ω_3 interact through the third-order nonlinear susceptibility $\chi^{(3)}$ to generate a fourth field, E_4, with propagation vector k_4 and frequency ω_4. The electric fields are defined as

$$E_j(r,t) = \frac{1}{2} E_j e^{-i(\omega_j t - k_j \cdot r)} + c.c. \quad ; \quad E_j = \mathcal{E}_j \varepsilon_j, \tag{1}$$

where E_j is the vector amplitude, $\mathcal{E}_j$ is the scalar amplitude, and ε_j is the normalized $(\varepsilon_j \cdot \varepsilon_j^* = 1)$ polarization unit vector of the electric field labeled j. The conventions for expressing the unit vectors are given in the Appendix.

For fully resonant DFWM $\omega_1 = \omega_2 = \omega_3 = \omega_4 = \omega$, and we assume that the excitation bandwidth is sufficiently narrow compared with the density of states (including Doppler broadening) of the absorbing molecules so that the interaction is exclusively between the degenerate magnetic sublevels of the two levels involved in the one-photon resonant transition. These levels are assumed to be characterized by total angular momentum **J**. Figure 2 shows a schematic energy-level diagram of the process described above. In this figure we restrict the letters g and g' to refer to two degenerate magnetic sublevels (either the same or different) of the lower level (usually the ground electronic state), and the letters e and e' refer to two degenerate magnetic sublevels (either the same or different) of the upper level (usually another electronic state). In the following discussion we adopt the standard nomenclature for the four fields involved in four-wave mixing: 1 and 3 refer to the two pump fields, 2 refers to the probe field, and 4 refers to the signal field.

The general expression for $\chi^{(3)}$ that applies here consists of 96 terms (48 for the upper level and 48 for the lower level) that completely describe the interaction of the electric fields with the molecular system.[40,41] These terms differ in the time ordering of the interaction fields and the permutations of the quantum states involved. Evaluating all of these terms is a formidable task in general; however, in a fully resonant four-wave mixing experiment, the intensity at a particular resonance in the spectrum is dominated by only sixteen terms.. This result is well established in the literature on resonant coherent CARS.[33,40] These terms are represented using double-sided Feynman diagrams in Fig. 3.

43
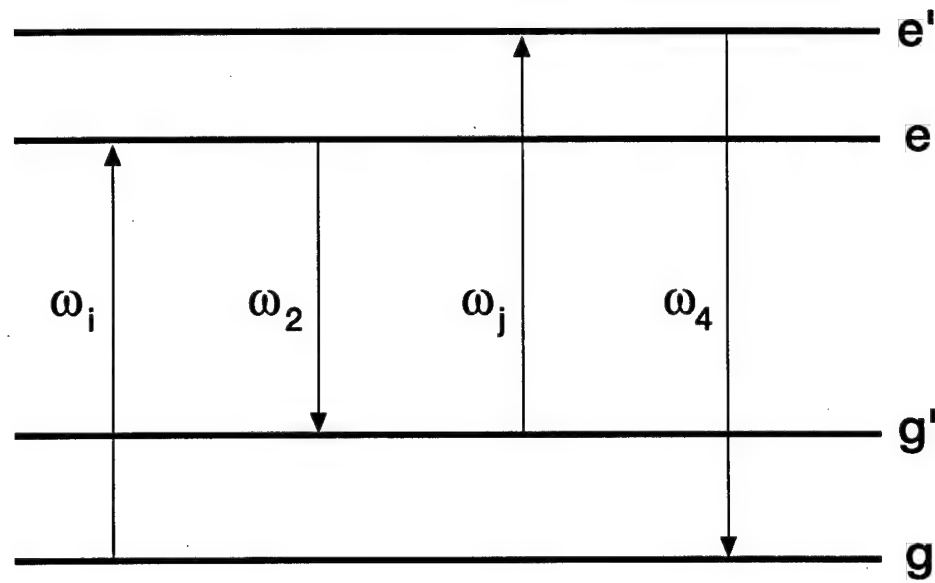
FIG. 3.2. Energy-level diagram for DFWM of a degenerate two-level system. In the figure $i = 1, j = 3$ or $i = 3, j = 1$.
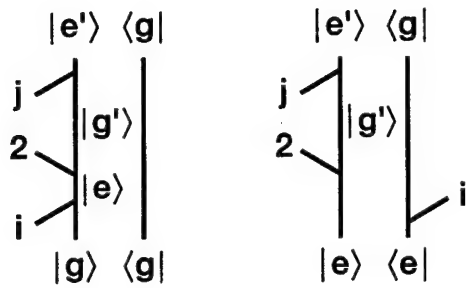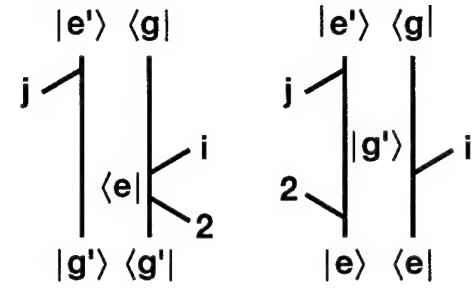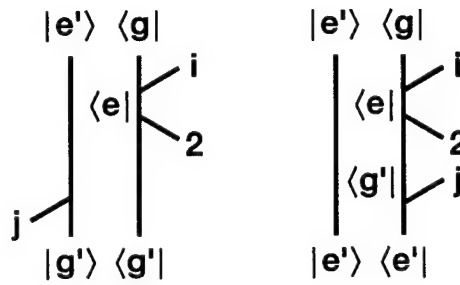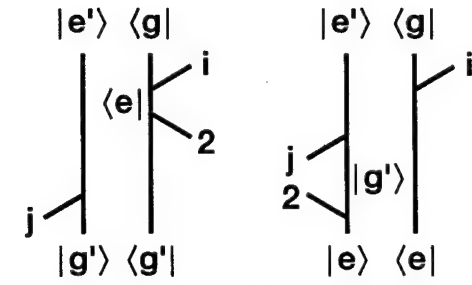
FIG. 3.3. Double-sided Feynman diagrams used to construct the DFWM third-order susceptibility. The first set of eight resonant contributions is formed by substituting $i = 1$, $j = 3$ and the second by $i = 3$, $j = 1$. The energy-resonant denominators (Eq. (23)) associated with each set of diagrams is indicated.

For fully resonant DFWM the summation over all state permutations reduces to a summation over the magnetic sublevels M_g, $M_{g'}$, M_e, and $M_{e'}$ of the two levels involved. Furthermore, if the initial magnetic sublevel distribution is isotropic, i.e., all degenerate M levels are equally populated and no phase relation exists between them, the summation is equally weighted. Taking these aspects into consideration, we write the DFWM signal intensity as

$$I_{DFWM}(\omega) \propto I_1 I_2 I_3 \left[N_g - \frac{(2J_g+1)}{(2J_e+1)} N_e \right]^2 \left[B_{ge}(J_g, J_e) \right]^4 \left| \mathcal{L}(\omega) \right|^2 \left| G_F^T(\varepsilon_4, \varepsilon_1, \varepsilon_3, \varepsilon_2; J_g, J_e; \omega) \right|^2, \quad (2)$$

where

$$\mathcal{L}(\omega) = \left[L_{12}^g(\omega) + L_{32}^g(\omega) + L_{12}^e(\omega) + L_{32}^e(\omega) \right] \quad (3)$$

is the total line shape function and

$$G_F^T(\varepsilon_4, \varepsilon_1, \varepsilon_3, \varepsilon_2; J_g, J_e; \omega) = W_{13}(\omega) G_F(\varepsilon_4, \varepsilon_1, \varepsilon_3, \varepsilon_2; J_g, J_e) + W_{31}(\omega) G_F(\varepsilon_4, \varepsilon_3, \varepsilon_1, \varepsilon_2; J_g, J_e) \quad (4)$$

is the total geometric factor. In Eq. (2) I_j is the intensity of the electric field labeled j, N_g and N_e are the total populations of the levels g and e, respectively, in the absence of applied fields, and $B_{ge}(J_g, J_e)$ is the Einstein absorption coefficient that connects the level with total angular momentum $\mathbf{J_g}$ to the level with $\mathbf{J_e}$. In Eq. (3) the $L_{j2}^n(\omega)$ are complex line shape functions. In Eq. (4) the $G_F(\varepsilon_4, \varepsilon_i, \varepsilon_j, \varepsilon_2; J_g, J_e)$ are geometric factors and depend solely on the polarization unit vectors of the electric fields ε_j and the total angular momentum quantum numbers J_e and J_g. The dimensionless weighting factors $W_{13}(\omega)$ and $W_{31}(\omega)$ of Eq. (4) are defined as

$$W_{13}(\omega) = \frac{L_{12}^g(\omega) + L_{32}^e(\omega)}{\mathcal{L}(\omega)} \quad (5a)$$

and

$$W_{31}(\omega) = \frac{L_{32}^g(\omega) + L_{12}^e(\omega)}{\mathcal{L}(\omega)}, \quad (5b)$$

and they satisfy the condition

$$W_{13}(\omega) + W_{31}(\omega) = 1. \quad (6)$$

Equation (2) is the key result of this section and expresses the DFWM signal intensity as a product of a concentration part, ΔN^2, a one-photon molecular part, B_{ge}^4, a line shape part, $\left| \mathcal{L}(\omega) \right|^2$, and a laboratory-frame geometric part, $\left| G_F^T \right|^2$. These quantities relate to different aspects of the experiment, and the DFWM signal intensity is directly proportional to them.

The Einstein absorption coefficients describe the strength of the interaction of the molecule with the excitation fields in the molecular-frame. These coefficients can be related to other molecular parameters such as the absorption cross-section, the oscillator strength, the line strength, the spontaneous emission lifetime, and the transition-dipole moment.[42] The literature provides an extensive theoretical and experimental data base of these parameters. The physical interpretation of the geometric factors $G_F\left(\varepsilon_4, \varepsilon_i, \varepsilon_j, \varepsilon_2; J_g, J_e\right)$ is given in Sec. III. The crucial point here is that these factors are just real numbers that account for the geometry of the interaction of the molecule with the electric fields in the laboratory frame. These terms are given in Table 3.1 for the allowed polarization configurations of circularly and linearly polarized light for the phase matching geometries of Fig. 1. The angle θ in Fig. 1 is small, usually less than 2°, so we assume that all of the electric fields involved in the DFWM process (excitation and signal) propagate along the space-fixed Z-axis. The collinear beam approximation in turn restricts the electric fields to lie in the space-fixed XY-plane, and we use the following conventions: (R) for right circularly polarized, (L) for left circularly polarized, X for $\phi = 0$ linearly polarized, and Y for $\phi = \pi/2$ linearly polarized (Fig. 4). Finally, the line shape functions $L_{j2}^n(\omega)$ are defined as

$$L_{j2}^n(\omega) = \int \frac{f(\mathbf{v}) d^3 \mathbf{v}}{\left[(\mathbf{k}_j - \mathbf{k}_2) \cdot \mathbf{v} - i\Gamma_n\right]} \left\{ \frac{1}{\left[\omega_o - \omega + \mathbf{k}_j \cdot \mathbf{v} - i\Gamma_{eg}\right]} - \frac{1}{\left[\omega_o - \omega + \mathbf{k}_2 \cdot \mathbf{v} + i\Gamma_{eg}\right]} \right\} \frac{1}{\left[\omega_o - \omega + \mathbf{k}_4 \cdot \mathbf{v} - i\Gamma_{eg}\right]} \quad (7)$$

where $f(\mathbf{v})$ is the normalized (Maxwell-Boltzmann) velocity-distribution function, $\hbar\omega_o$ is the energy difference between the e and g levels, and $2\Gamma_{eg}$ is the homogeneous full-width (no Doppler broadening) of a dipolar transition between the e and g levels. The sub- and superscripts on L refer to the first terms of Eq. (7). Specifically for the line shape function $L_{j2}^n(\omega)$, n is the quantum-state label of Γ_n where $1/\Gamma_n$ is the total lifetime of the nth level, and j is the field label, either 1 or 3, that corresponds to the k vector difference $\Delta k_{j2} = (k_j - k_2)$. The velocity integration of Eq. (7) has been performed by many authors[10,29-31,40,43] and is not discussed here.

Only collisional relaxation is considered (no spontaneous emission) in Eq. (7), and we assume that the collisional relaxation of the population, the orientation, and the alignment can be represented by a single rate Γ_n. This "single relaxation" assumption is generally valid; however in experiments where efficient energy transfer collision partners such as water are absent, levels characterized by low values of $\mathbf{J}$ may relax with multiple rates. This topic is discussed in Sec. IIIC.

Table 3.1. Geometric factors for circular and linear polarization combinations with the following conventions: (R) for right circular polarization; (L) for left circular polarization; X for $\phi = 0$ linear polarization; and, Y for $\phi = \pi/2$ linear polarization. Permuting $R \leftrightarrow L$ or $X \leftrightarrow Y$ does not change the values of the geometric factors.

$\varepsilon_4\varepsilon_i\varepsilon_j\varepsilon_2$	P Branch $G_F(\varepsilon_4,\varepsilon_i,\varepsilon_j,\varepsilon_2;J,J-1)$	High-J Limit	Q Branch $G_F(\varepsilon_4,\varepsilon_i,\varepsilon_j,\varepsilon_2;J,J)$	High-J Limit	R Branch $G_F(\varepsilon_4,\varepsilon_i,\varepsilon_j,\varepsilon_2;J,J+1)$	High-J Limit
RRRR	$\dfrac{1}{15}\dfrac{(6J^2-1)}{J(2J-1)}$	$\dfrac{1}{5}$	$\dfrac{1}{15}\dfrac{(2J^2+2J+1)}{J(J+1)}$	$\dfrac{2}{15}$	$\dfrac{1}{15}\dfrac{(6J^2+12J+5)}{(2J+3)(J+1)}$	$\dfrac{1}{5}$
RLRL	$\dfrac{1}{30}\dfrac{(2J^2-5J+3)}{J(2J-1)}$	$\dfrac{1}{30}$	$\dfrac{1}{30}\dfrac{(4J^2+4J-3)}{J(J+1)}$	$\dfrac{2}{15}$	$\dfrac{1}{30}\dfrac{(2J^2+9J+10)}{(2J+3)(J+1)}$	$\dfrac{1}{30}$
RRLL	$\dfrac{1}{30}\dfrac{(2J^2+5J+3)}{J(2J-1)}$	$\dfrac{1}{30}$	$\dfrac{1}{30}\dfrac{(4J^2+4J-3)}{J(J+1)}$	$\dfrac{2}{15}$	$\dfrac{1}{30}\dfrac{(2J^2-J)}{(2J+3)(J+1)}$	$\dfrac{1}{30}$
YYYY	$\dfrac{1}{15}\dfrac{(4J^2+1)}{J(2J-1)}$	$\dfrac{2}{15}$	$\dfrac{1}{15}\dfrac{(3J^2+3J-1)}{J(J+1)}$	$\dfrac{1}{5}$	$\dfrac{1}{15}\dfrac{(4J^2+8J+5)}{(2J+3)(J+1)}$	$\dfrac{2}{15}$
YXYX	$\dfrac{1}{30}\dfrac{(6J^2-5J-1)}{J(2J-1)}$	$\dfrac{1}{10}$	$\dfrac{1}{30}\dfrac{(2J^2+2J+1)}{J(J+1)}$	$\dfrac{1}{15}$	$\dfrac{1}{30}\dfrac{(6J^2+17J+10)}{(2J+3)(J+1)}$	$\dfrac{1}{10}$
YYXX	$\dfrac{1}{30}\dfrac{(6J^2+5J-1)}{J(2J-1)}$	$\dfrac{1}{10}$	$\dfrac{1}{30}\dfrac{(2J^2+2J+1)}{J(J+1)}$	$\dfrac{1}{15}$	$\dfrac{1}{30}\dfrac{(6J^2+7J)}{(2J+3)(J+1)}$	$\dfrac{1}{10}$
YXXY	$-\dfrac{2}{15}\dfrac{(J^2-1)}{J(2J-1)}$	$-\dfrac{1}{15}$	$\dfrac{1}{15}\dfrac{(J^2+J-2)}{J(J+1)}$	$\dfrac{1}{15}$	$-\dfrac{2}{15}\dfrac{(J^2+2J)}{(2J+3)(J+1)}$	$-\dfrac{1}{15}$
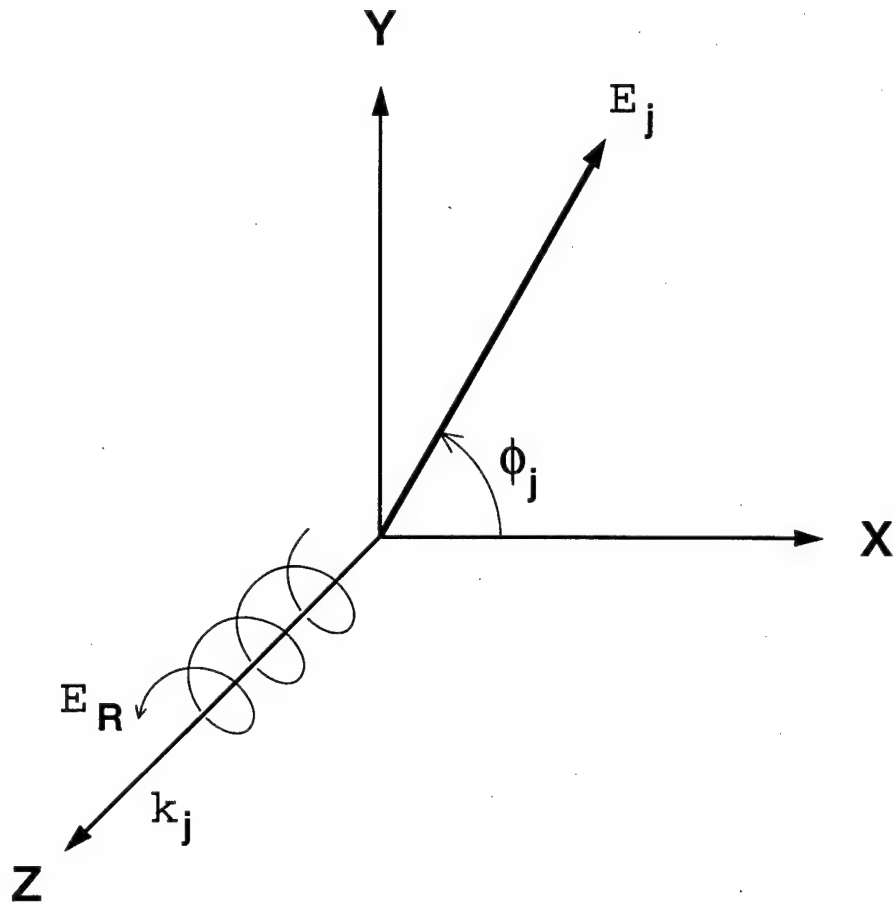
FIG. 3.4. Electric field vectors E_j and E_R in the laboratory frame for linear and right circular polarized light waves, respectively. The propagation direction is the Z-axis.

In Eq. (4), the geometric factors are weighted by the line shape functions defined in Eq. (7). Therefore, the total DFWM polarization dependence for a given experiment is sensitive to more than the polarizations of the excitation fields; it is also sensitive to the phase matching geometry, the velocity distribution of the absorbing molecules, and the collisional dynamics caused by the environment. This interdependence is an important aspect of DFWM.

For many cases the two geometric factors of Eq. (4) are equal or equally weighted. In these situations the total geometric factor becomes

$$G_F^T\left(\varepsilon_4,\varepsilon_1,\varepsilon_3,\varepsilon_2;J_g,J_e;\omega\right) = G_F^T(\varepsilon_4,\varepsilon_1,\varepsilon_3,\varepsilon_2;J_g,J_e),$$

$$= \frac{1}{2}\left[G_F(\varepsilon_4,\varepsilon_1,\varepsilon_3,\varepsilon_2;J_g,J_e) + G_F(\varepsilon_4,\varepsilon_3,\varepsilon_1,\varepsilon_2;J_g,J_e)\right] \quad (8)$$

and is independent of the velocity distribution of the absorbing molecules and the collisional dynamics caused by the environment. All of this information is then contained exclusively in the total line shape function $\mathcal{L}(\omega)$! This is a powerful result because the DFWM polarization dependence has been disentangled from the collisional dynamics of the experimental environment and depends only on the polarization states of the incident fields and the total angular momentum of the levels involved. Equation (8) has been evaluated for all allowed polarization configurations for circularly and linearly polarized light, and the results are given in Table 3.2 as a function of transition type using the same conventions as in Table 3.1.

The total geometric factors of Table 3.2 can be related to what is more commonly referred to as four-wave mixing line strength factors $S_{FWM}(\varepsilon_4,\varepsilon_1,\varepsilon_3,\varepsilon_2;J_g,J_e)$[33,36,37] by

$$S_{FWM}(\varepsilon_4,\varepsilon_1,\varepsilon_3,\varepsilon_2;J_g,J_e) = (S_{J_g J_e}^R)^2\, G_F^T(\varepsilon_4,\varepsilon_1,\varepsilon_3,\varepsilon_2;J_g,J_e)/(2J_g+1), \quad (9)$$

where $S_{J_g J_e}^R$ is the molecular rotational line strength (Hönl-London factor) for a one-photon transition[3] and $G_F^T(\varepsilon_4,\varepsilon_1,\varepsilon_3,\varepsilon_2;J_g,J_e)$ is defined in Eq. (8). In the general case, population distributions cannot be extracted using the line strength factors of Eq. (9), because the total geometric factor depends on the line shape functions, i.e., the overall DFWM polarization response depends on more than the polarization of the excitation fields.

In our discussion of polarization effects, it is useful to derive expressions that relate how observed DFWM signals vary for a given transition as the polarization of the excitation fields is varied. This variation in DFWM signals is best expressed in terms of a polarization ratio defined as

Table 3.2. Total geometric factors for FB-DFWM and for BB-, PC-DFWM when Chapter 3 Eq. (8) is valid. The conventions are the same as Table 3.1, and permuting $R \leftrightarrow L$ or $X \leftrightarrow Y$ does not change the values of the total geometric factors.

| $\varepsilon_4\varepsilon_1\varepsilon_3\varepsilon_2$	P Branch $G_F^T(\varepsilon_4,\varepsilon_1,\varepsilon_3,\varepsilon_2;J,J-1)$	High-J Limit	Q Branch $G_F^T(\varepsilon_4,\varepsilon_1,\varepsilon_3,\varepsilon_2;J,J)$	High-J Limit	R Branch $G_F^T(\varepsilon_4,\varepsilon_1,\varepsilon_3,\varepsilon_2;J,J+1)$	High-J Limit
RRRR	$\dfrac{1}{15}\dfrac{(6J^2-1)}{J(2J-1)}$	$\dfrac{1}{5}$	$\dfrac{1}{15}\dfrac{(2J^2+2J+1)}{J(J+1)}$	$\dfrac{2}{15}$	$\dfrac{1}{15}\dfrac{(6J^2+12J+5)}{(2J+3)(J+1)}$	$\dfrac{1}{5}$
RLRL	$\dfrac{1}{30}\dfrac{(2J^2+3)}{J(2J-1)}$	$\dfrac{1}{30}$	$\dfrac{1}{30}\dfrac{(4J^2+4J-3)}{J(J+1)}$	$\dfrac{2}{15}$	$\dfrac{1}{30}\dfrac{(2J^2+4J+5)}{(2J+3)(J+1)}$	$\dfrac{1}{30}$
RRLL	$\dfrac{1}{30}\dfrac{(2J^2+3)}{J(2J-1)}$	$\dfrac{1}{30}$	$\dfrac{1}{30}\dfrac{(4J^2+4J-3)}{J(J+1)}$	$\dfrac{2}{15}$	$\dfrac{1}{30}\dfrac{(2J^2+4J+5)}{(2J+3)(J+1)}$	$\dfrac{1}{30}$
YYYY	$\dfrac{1}{15}\dfrac{(4J^2+1)}{J(2J-1)}$	$\dfrac{2}{15}$	$\dfrac{1}{15}\dfrac{(3J^2+3J-1)}{J(J+1)}$	$\dfrac{1}{5}$	$\dfrac{1}{15}\dfrac{(4J^2+8J+5)}{(2J+3)(J+1)}$	$\dfrac{2}{15}$
YXYX	$\dfrac{1}{30}\dfrac{(6J^2-1)}{J(2J-1)}$	$\dfrac{1}{10}$	$\dfrac{1}{30}\dfrac{(2J^2+2J+1)}{J(J+1)}$	$\dfrac{1}{15}$	$\dfrac{1}{30}\dfrac{(6J^2+12J+5)}{(2J+3)(J+1)}$	$\dfrac{1}{10}$
YYXX	$\dfrac{1}{30}\dfrac{(6J^2-1)}{J(2J-1)}$	$\dfrac{1}{10}$	$\dfrac{1}{30}\dfrac{(2J^2+2J+1)}{J(J+1)}$	$\dfrac{1}{15}$	$\dfrac{1}{30}\dfrac{(6J^2+12J+5)}{(2J+3)(J+1)}$	$\dfrac{1}{10}$
YXXY	$-\dfrac{2}{15}\dfrac{(J^2-1)}{J(2J-1)}$	$-\dfrac{1}{15}$	$\dfrac{1}{15}\dfrac{(J^2+J-2)}{J(J+1)}$	$\dfrac{1}{15}$	$-\dfrac{2}{15}\dfrac{(J^2+2J)}{(2J+3)(J+1)}$	$-\dfrac{1}{15}$

$$P\left(\frac{\varepsilon'_4,\varepsilon'_1,\varepsilon'_3,\varepsilon'_2}{\varepsilon_4,\varepsilon_1,\varepsilon_3,\varepsilon_2}\right) = \frac{I'_{DFWM}}{I_{DFWM}} \qquad (10)$$

which is merely the ratio of the DFWM signal intensities for two different polarization configurations in which all other aspects of the experiment are the same. The three fundamental polarization ratios for circularly and linearly polarized light that can be derived using the values of Table 3.2 in Eq. (10) are given in Table 3.3. Note that more ratios can be formed by permuting $R \leftrightarrow L$ and $X \leftrightarrow Y$, but they are identical to those given in Table 3.3. The polarization ratios rapidly approach a high-J limit, and therefore, these values generally describe the DFWM signal variation, as the polarization configuration is changed for those systems for which Eq. (8) is valid.

We turn to a discussion of specific experimental conditions in which we point out the cases for which Eq. (4) reduces to Eq. (8). Here, we invoke the grating picture of DFWM to gain some insight as to the relative magnitude of the line shape functions $L^n_{j2}(\omega)$. The grating picture of DFWM involves the interference of the excitation fields. When the excitation fields are tuned to a one-photon resonance, the interference between two of the fields, E_2 and E_j ($j=1$ or 3), leads to a spatial modulation in the (complex) refractive index and hence forms a grating that can scatter the third field into a fourth field (DFWM signal).[10,44] The grating is characterized by the grating k-vector, $\Delta k_{j2} = (k_j - k_2)$, which describes the grating's orientation and spacing in the laboratory frame. The grating spacing D_{j2} is given by

$$D_{j2} = \frac{2\pi}{|\Delta k_{j2}|} = \frac{\lambda}{2\sin(\theta/2)} \qquad (11)$$

where $|\Delta k_{j2}|$ is the magnitude of the grating k-vector and θ is the angle between the two propagation vectors, k_j and k_2, of the fields forming the grating ($0 \le \theta \le \pi$). When θ is small the grating spacing is large, and when θ is large the grating spacing is small. If the absorbers involved in forming the grating are moving, such as in a gas, the grating with the smallest spacing is "washed out" to a higher degree when Doppler broadening is significant.[45] This argument is useful in predicting the general DFWM polarization dependence and is substantiated by evaluating the integrals of Eq. (7).[43]

Table 3.3. [a]Polarization ratios calculated using the values of Table 3.2 with $J=J_g$.

	P Branch	High-J Limit	Q Branch	High-J Limit	R Branch	High-J Limit
$P(I)$	$\frac{1}{4}\left[\frac{(J^2-1)}{(J^2+\frac{1}{4})}\right]^2$	$\frac{1}{4}$	$\frac{1}{9}\left[\frac{(J^2+J-2)}{(J^2+J-\frac{1}{3})}\right]^2$	$\frac{1}{9}$	$\frac{1}{4}\left[\frac{(J^2+2J)}{(J^2+2J+\frac{3}{4})}\right]^2$	$\frac{1}{4}$
$P(II)$	$\frac{9}{16}\left[\frac{(J^2-\frac{5}{9})}{(J^2+\frac{1}{4})}\right]^2$	$\frac{9}{16}$	$\frac{1}{9}\left[\frac{(J^2+J+\frac{1}{2})}{(J^2+J-\frac{1}{3})}\right]^2$	$\frac{1}{9}$	$\frac{9}{16}\left[\frac{(J^2+2J+\frac{5}{9})}{(J^2+2J+\frac{3}{4})}\right]^2$	$\frac{9}{16}$
$P(III)$	$\frac{1}{36}\left[\frac{(J^2+\frac{3}{2})}{(J^2-\frac{5}{6})}\right]^2$	$\frac{1}{36}$	$\left[\frac{(J^2+J-\frac{3}{4})}{(J^2+J+\frac{1}{2})}\right]^2$	1	$\frac{1}{36}\left[\frac{(J^2+2J+\frac{5}{2})}{(J^2+2J+\frac{5}{6})}\right]^2$	$\frac{1}{36}$

$^a P(I)=P\left(\frac{YXXY}{YYYY}\right)$, $P(II)=P\left(\frac{YXYX}{YYYY}\right)=P\left(\frac{YYXX}{YYYY}\right)=\frac{1}{4}P\left(\frac{RRRR}{YYYY}\right)$, and

$P(III)=P\left(\frac{RLRL}{RRRR}\right)=\frac{1}{4}P\left(\frac{RLRL}{YXYX}\right)=\frac{1}{4}P\left(\frac{RLRL}{YXYX}\right)=P\left(\frac{RRLL}{YYXX}\right)=\frac{1}{4}P\left(\frac{RRLL}{RRRR}\right)=\frac{1}{4}P\left(\frac{RRLL}{YXYX}\right)=\frac{1}{4}P\left(\frac{RRLL}{YYXX}\right)$

B. Phase Matching Geometry 1: Forward Box DFWM (FB-DFWM)

We are prepared to consider the polarization effects for specific phase matching geometries and the relative sensitivity of these effects to the collisional environment. For the FB-DFWM geometry of Fig. 1, all fields are nearly copropagating, $\theta \cong 0$, and $|\Delta k_{12}| = |\Delta k_{32}| \cong 0$. Therefore all the gratings formed in the FB-DFWM phase matching geometry have large grating spacings, $D_{12} = D_{32} \rightarrow \infty$, and

$$L_{12}^g(\omega) = L_{32}^g(\omega) \; ; \; L_{12}^e(\omega) = L_{32}^e(\omega). \tag{12}$$

Substituting Eq. (12) into Eqs. (5a) and (5b) shows that geometric factors that correspond to the interchange of the two pump fields (1 and 3) are equally weighted. The total geometric factor has the simple form of Eq. (8) for all transition types and polarization configurations. Therefore Tables 3.2 and 3.3 contain all of the relevant polarization information for FB-DFWM. As shown in Table 3.3, the polarization ratios are equal for any entry with orthogonally polarized pump fields ($\varepsilon_1 \cdot \varepsilon_3^* = 0$). This result distinguishes the FB-DFWM configuration from the other configurations as we shall see below. This distinction is in addition to the fact that FB-DFWM is not a sub-Doppler spectroscopic technique.

C. Phase Matching Geometries 2 and 3: Backward Box and Phase Conjugate DFWM (BB- and PC-DFWM)

For the BB-DFWM and PC-DFWM geometries of Fig. 1, fields 1 and 2 are nearly copropagating, $|\Delta k_{12}| \cong 0$, and fields 3 and 2 are nearly counterpropagating, $|\Delta k_{32}| \cong 2k = 4\pi / \lambda$. Therefore two types of gratings are formed in these phase matching geometries: one has a large grating spacing, $D_{12} \rightarrow \infty$; and the other has a small spacing, $D_{32} \rightarrow \lambda / 2$. Allowing for more wash out of the small-spaced grating compared to the large-spaced grating when the molecules are moving, we may write the following inequalities:

$$L_{12}^g(\omega) \geq L_{32}^g(\omega) \; ; \; L_{12}^e(\omega) \geq L_{32}^e(\omega). \tag{13}$$

Unlike for FB-DFWM, the total geometric factors for BB- and PC-DFWM that correspond to the interchange of the two pump fields (1 and 3) are generally not weighted equally. Hence the overall DFWM polarization response, i.e., the total geometric factor $G_F^T(\varepsilon_4, \varepsilon_1, \varepsilon_3, \varepsilon_2; J_g, J_e; \omega)$ of Eq. (4), will be sensitive to the collisional environment because the weighting factors $W_{13}(\omega)$ and $W_{31}(\omega)$ are dependent on the relative relaxation

rates of the g and e levels. This dependence complicates the interpretation of DFWM spectra for these phase matching geometries, and the weighted average expressed in Eq. (4) generally must be performed.

In some cases, however, the polarization dependence for BB- and PC-DFWM can be disentangled from collisional effects. These cases arise when

$$G_F(\varepsilon_4, \varepsilon_1, \varepsilon_3, \varepsilon_2; J_g, J_e) = G_F(\varepsilon_4, \varepsilon_3, \varepsilon_1, \varepsilon_2; J_g, J_e) \qquad (14a)$$

or when

$$\Gamma_g = \Gamma_e \Rightarrow L^g_{12}(\omega) = L^e_{12}(\omega) \; ; \; L^g_{32}(\omega) = L^e_{32}(\omega) . \qquad (14b)$$

For these cases Eq. (4) reduces to Eq. (8), and again, the DFWM polarization response only depends on the polarization states of the incident fields and the total angular momentum of the levels involved. Equation (14a) is satisfied for all Q-branch ($\Delta J = 0$) transitions and for P-branch ($\Delta J = -1$) and R-branch ($\Delta J = +1$) transitions when the two pump fields are of the same polarization ($\varepsilon_1 \cdot \varepsilon_3^* = 1$). Therefore, the simple results of Tables 3.2 and 3.3 can be used to evaluate BB- and PC-DFWM signal intensities for Q-branch transitions and for P- and R-branch transitions when $\varepsilon_1 \cdot \varepsilon_3^* = 1$ in addition to FB-DFWM signal intensities. For P- and R-branch transitions with orthogonally polarized pump fields ($\varepsilon_1 \cdot \varepsilon_3^* = 0$), however, Eq. (14b) must be satisfied for the results of Tables 3.2 and 3.3 to apply, i.e., the upper and lower levels must relax at the same rate. If neither Eq. (14a) nor (14b) is satisfied, the DFWM polarization response depends on the dynamics of the collisional environment under study. This drawback is offset because collisional relaxation information can be obtained from polarization-ratio measurements without having to resolve spectral line shapes.[17,46]

Grating wash out leading to the inequality in Eq. (13) often occurs for Doppler-broadened systems in which the homogeneous full-width $2\Gamma_{eg}$ of the spectroscopic transition between levels e and g is smaller than the Doppler width $\Delta\omega_D$ ($2\Gamma_{eg} < \Delta\omega_D$). Experiments conducted under low-pressure, high-temperature conditions, such as atmospheric-pressure (and lower) flames and plasmas, are examples of Doppler-broadened systems. Again invoking the grating picture of DFWM for this case yields $L^g_{12} > L^g_{32}$ and $L^e_{12} > L^e_{32}$; in other words, the small spaced-grating is washed out more than the large-spaced grating. Substituting these inequalities into Eq. (4) shows that P- and R-branch transitions with orthogonally polarized pump fields are sensitive to differences in the relaxation rates of the g and e levels. To emphasize this point consider the case when $\Gamma_g < \Gamma_e$. Given two orthogonal polarization states ε' and ε'', we have

55

$$G_F^T\left(\varepsilon',\varepsilon',\varepsilon'',\varepsilon'';J_g,J_e;\omega\right) > G_F^T\left(\varepsilon',\varepsilon'',\varepsilon',\varepsilon'';J_g,J_e;\omega\right) \qquad (15a)$$

for P-branch ($\Delta J = -1$) transitions, and

$$G_F^T\left(\varepsilon',\varepsilon',\varepsilon'',\varepsilon'';J_g,J_e;\omega\right) < G_F^T\left(\varepsilon',\varepsilon'',\varepsilon',\varepsilon'';J_g,J_e;\omega\right) \qquad (15b)$$

for R-branch ($\Delta J = +1$) transitions. If $\Gamma_g > \Gamma_e$, the inequalities of Eqs. (15a) and (15b) are reversed. These inequalities hold for frequency-integrated DFWM signal intensities as well. Analytic expressions for the line shape functions in the Doppler-broadened limit are found in references 10 and 43 and can be used to quantify the inequalities of Eqs. (15a) and (15b).

Recall that for P- and R-branch transitions with $\Gamma_g = \Gamma_e$, the total geometric factor is invariant to the exchange of the polarizations of the pump fields. This result is important because even though most flame and plasma experiments are Doppler-broadened, diagnostic applications typically involve the investigation of molecular species in which rotational energy transfer collisions are the dominant type of collision. Furthermore the energy-level spacings of the g and e levels of these species are usually similar, and as a result, they have similar rotational energy transfer rates. For these experiments, $\Gamma_g \cong \Gamma_e$, and to a first approximation, the simple results of Tables 3.2 and 3.3 describe the DFWM polarization response. This response is discussed in detail in Chapter 4 for the case of the CH radical in an atmospheric-pressure flame.

We conclude this discussion by considering systems in the homogeneously broadened limit, i.e., $2\Gamma_{eg} \gg \Delta\omega_D$. Experiments performed in supercritical water[47] that are characterized by high pressure (tens of atmospheres) and low temperature (~ 400 K) closely approximate this limit. In this limit $L_{12}^g \cong L_{32}^g$ and $L_{12}^e \cong L_{32}^e$ because the absorbers are effectively relaxed before they have a chance to move, and thus neither the large- nor small-spaced gratings are washed out. Therefore for homogeneously broadened systems Eq. (4) reduces to Eq. (8), and the results presented in Tables 3.2 and 3.3 apply. For a more precise evaluation of Eq. (4), Wandzura[48] obtained analytic expressions for the line shape functions in this limit that can be used to calculate the DFWM polarization dependence.

D. Other Signal Contributions

The discussion above assumes that no other process contributes to the DFWM signal. For some experimental conditions, however, other types of laser-induced grating phenomena[44] can coherently scatter light along the DFWM signal direction. The most

likely candidate is a thermal grating that results from the localized absorption of the laser energy and subsequent heating of the medium. This absorption leads to a spatial-density modulation in gases that can produce signals on the order of or greater than the DFWM response under some conditions.[46,49,50] Another intensity grating effect observed at high laser intensities is an electrostrictive grating[51] that results from an electric-field-induced modulation in the gas density. These types of effects, however, can result only from the interference of two fields that have the same polarization (intensity gratings); fields with orthogonal polarizations do not produce such effects (polarization gratings) because there is no spatial modulation of the field intensity (only its polarization is spatially modulated).[52,53] If the molecule is optically active (chiral), however, then circular-dichroism induced thermal gratings can be formed with orthogonally polarized fields.[54]

If other types of gratings are present, polarization dependences different from those discussed above are observed. In particular, polarization configurations that involve large-spaced intensity gratings have anomalous signal intensities if additional intensity grating contributions are present. A good way to test for this effect is to measure the polarization ratio of a Q-branch transition with orthogonally polarized pump fields in the BB- or PC-DFWM phase matching geometry. If the polarization ratio is not unity, another process is likely to be contributing.[17] Rahn and Brown[46] used similar polarization techniques to determine that thermal gratings make significant contributions to OH spectra taken in atmospheric-pressure flames. If other gratings are determined to be contributing, the YXXY polarization configuration best discriminates against their contribution for all experimental conditions, but the YYXX and RRLL configurations are also good choices for Doppler-broadened systems with grating wash out because only small-spaced intensity gratings are present.

E. Influence of Hyperfine Structure

A full treatment considering the influence of hyperfine structure is possible,[31,35] but the additional complexity required to include such effects is not warranted[2,55] for the conditions described in this chapter, i.e., the spectroscopy of molecular systems in collisionally dominated environments. This conclusion can be justified by invoking the vector model of angular momenta. In the absence of collisions, the rotational angular momentum J couples to the nuclear angular momentum I to form the total angular momentum F so that the prepared direction of J in the laboratory-frame is lost to some degree (depolarized). This directional blurring obviously influences the geometric factors

related to the distribution of **J** in the laboratory frame. If the magnitude of **J** is substantially larger than the magnitude of **I** (typically **I** takes values up to about 5/2), **J** and **F** will be close to parallel, and the hyperfine depolarization will be small. This condition is usually satisfied for DFWM spectra of molecular species in which the magnitude of **J** for the levels of interest is much larger than the magnitude of **I**. However for low values of **J** (magnitudes of **J** close to or smaller than those of **I**), the hyperfine depolarization can be significant.

If **J** is effectively decoupled from **I** by collisions, the hyperfine depolarization is small even for low **J** values. We used time-independent diagrammatic perturbation theory to derive the results of this chapter, which implies that the results are valid for low-intensity, steady-state conditions in which population transfer is assumed to be small. Inherent in this approximation is the fact that the population relaxation and collisional dephasing times must be much shorter than the temporal duration of the laser pulse. These collisional times are typically much shorter than the precessional period of **J** about **F** (usually tens of nanoseconds or longer), which implies that hyperfine depolarization will not be significant for collisionally dominated systems. A quick experimental check is to determine if the hyperfine structure is spectrally resolved in either the BB- or PC-DFWM (sub-Doppler) phase matching geometries. If it is not resolved, hyperfine interactions will not significantly affect the results presented here. This conclusion follows because unresolved hyperfine structure suggests that the hyperfine splitting is small compared with the collisional broadening of the hyperfine components, which in turn implies that the precessional period of **J** about **F** is slow compared with the time it takes to collisionally decouple **J** from **I**.

III. INTERPRETATION OF THE DFWM SIGNAL INTENSITY IN TERMS OF MULTIPOLE MOMENTS

A. Derivation and General Expressions

In DFWM two molecular levels with total angular momentum quantum numbers J_g and J_e, respectively, are coupled by the input fields. Describing the resulting coherence between these levels in terms of the total angular momentum distribution is convenient. The most complete description of the angular momentum distribution is in terms of state multipoles that represent the populations of the levels and the coherences existing between them.[56,57] The state multipoles are spherical tensors of rank K and component Q

$(-K \le Q \le K)$. The $Q = 0$ components describe the projection of $\mathbf{J}$ onto the space-fixed Z-axis, and the $Q \ne 0$ components describe the projection of $\mathbf{J}$ onto the space-fixed XY-plane. Here the monopole term (K=0) is proportional to the population. All odd rank multipoles (dipole, octopole, etc.) describe the orientation of the angular momentum, and all even rank multipoles (quadrupole, hexadecapole, etc.) are related to the alignment of the angular momentum. Below we show that the highest allowed value of K for unsaturated DFWM is 2. Therefore, we take the K=0, 1, and 2 terms to describe the (scalar) population, (dipolar) orientation, and (quadupolar) alignment, respectively.

We outline a method for calculating the third-order nonlinear polarization for fully resonant DFWM of molecular gases in collisionally dominated environments. The expressions are derived using diagrammatic perturbation theory[40,41,58,59] and are evaluated using a spherical tensor formalism[3,60,61] The techniques used are standard; consequently, only the key elements of the derivation are presented.

The molecular levels are coupled by three input electric fields. The intensity of each electric field $E_j(r,t)$ is given by

$$I_j = \varepsilon_o c \left\langle \left| E_j(r,t) \right|^2 \right\rangle = \frac{\varepsilon_o c}{2} \left| \mathcal{E}_j \right|^2 \tag{16}$$

where the angular brackets denote a cycle average and j is the field label, ε_o is the permittivity of free space, c is the speed of light, and $\mathcal{E}_j$ is the scalar amplitude of the electric field. The result of the interaction of the three electric fields with the molecular sample is the generation of the third-order electric polarization $P^{(3)}(r,t)$. We note that many conventions are used for expressing $P^{(3)}(r,t)$. Therefore for clarity, we follow the convention of Butcher and Cotter[62] throughout and write $P^{(3)}(r,t)$ in SI units as

$$P^{(3)}(r,t) = \frac{1}{2} P^{(3)}_{DFWM} e^{-i(\omega_4 t - k_4 \cdot r)} + c.c. \ ; \ P^{(3)}_{DFWM} = \wp^{(3)}_{DFWM} \varepsilon_4 \tag{17}$$

where $P^{(3)}_{DFWM}$ is the vector amplitude, and $\wp^{(3)}_{DFWM}$ is the scalar amplitude, and ε_4 is the normalized $(\varepsilon_4 \cdot \varepsilon_4^* = 1)$ polarization vector. $P^{(3)}_{DFWM}$ is defined in terms of the DFWM third-order nonlinear susceptibility $\chi^{(3)}_{DFWM}(-\omega_4, \omega_1, \omega_3, -\omega_2)$ as

$$P^{(3)}_{DFWM} = \varepsilon_o \frac{3}{4} \chi^{(3)}_{DFWM}(-\omega_4, \omega_1, \omega_3, -\omega_2) \vdots E_1 E_2^* E_3. \tag{18}$$

where the symbol $\vdots$ refers to tensor contraction. The DFWM signal intensity is proportional to the cycle average of the absolute square of the third-order nonlinear polarization. In analogy with Eq. (16), the DFWM signal intensity is proportional to the absolute value squared of the scalar amplitude $\wp^{(3)}_{DFWM}$, i.e.,

$$I_{DFWM} \propto \left\langle \left| P^{(3)}(r,t) \right|^2 \right\rangle = \left| \wp_{DFWM}^{(3)} \right|^2. \tag{19}$$

Therefore our concern is to calculate $\wp_{DFWM}^{(3)}$ where

$$\wp_{DFWM}^{(3)} = P_{DFWM}^{(3)} \cdot \varepsilon_4^* = \varepsilon_o \frac{3}{4} \chi_{DFWM}^{(3)}(-\omega_4, \omega_1, \omega_3, -\omega_2) \, \mathcal{E}_1 \mathcal{E}_2^* \mathcal{E}_3 \tag{20}$$

and $\chi_{DFWM}^{(3)}(-\omega_4, \omega_1, \omega_3, -\omega_2)$ is the scalar form of the third-order susceptibility. See reference 62, page 27.

The significant contributions to the DFWM third-order nonlinear susceptibility are represented using double-sided Feynman diagrams in Fig. 3. Note that sixteen diagrams are necessary to account for all of the time orderings that correspond to the energy-level diagram of Fig. 2. These diagrams represent the following expression[33] for $\chi_{DFWM}^{(3)}(-\omega_4, \omega_1, \omega_3, -\omega_2)$ in the perturbative (weak-field) limit:

$$\chi_{DFWM}^{(3)}(-\omega_4, \omega_1, \omega_3, -\omega_2) = \frac{1}{6\varepsilon_o \hbar^3} \left[C(-\omega_4, \omega_1, \omega_3, -\omega_2) + C(-\omega_4, \omega_3, \omega_1, -\omega_2) \right], \tag{21}$$

where

$$C(-\omega_4; \omega_i, \omega_j, -\omega_2)$$

$$= N \Bigg\{ \sum_{all\ M} \left\langle g \left| \varepsilon_4^* \cdot \boldsymbol{\mu} \right| e' \right\rangle \left\langle e' \left| \varepsilon_j \cdot \boldsymbol{\mu} \right| g' \right\rangle \left\langle g' \left| \varepsilon_2^* \cdot \boldsymbol{\mu} \right| e \right\rangle \left\langle e \left| \varepsilon_i \cdot \boldsymbol{\mu} \right| g \right\rangle (A - B_1)$$

$$+ \sum_{all\ M} \left\langle e' \left| \varepsilon_j \cdot \boldsymbol{\mu} \right| g' \right\rangle \left\langle g' \left| \varepsilon_2^* \cdot \boldsymbol{\mu} \right| e \right\rangle \left\langle e \left| \varepsilon_i \cdot \boldsymbol{\mu} \right| g \right\rangle \left\langle g \left| \varepsilon_4^* \cdot \boldsymbol{\mu} \right| e' \right\rangle (B_2 - B_3) \Bigg\}, \tag{22}$$

and

$$A = (\rho_{gg}^{(0)} - \rho_{ee}^{(0)}) \left\{ \left[\omega_o - \omega + k_i \cdot \mathbf{v} - i\Gamma_{eg} \right] \left[(k_i - k_2) \cdot \mathbf{v} - i\Gamma_{g'g} \right] \left[\omega_o - \omega + k_4 \cdot \mathbf{v} - i\Gamma_{e'g} \right] \right\}^{-1}, \tag{23a}$$

$$B_1 = (\rho_{g'g'}^{(0)} - \rho_{ee}^{(0)}) \left\{ \left[\omega_o - \omega + k_2 \cdot \mathbf{v} + i\Gamma_{eg'} \right] \left[(k_i - k_2) \cdot \mathbf{v} - i\Gamma_{g'g} \right] \left[\omega_o - \omega + k_4 \cdot \mathbf{v} - i\Gamma_{e'g} \right] \right\}^{-1}, \tag{23b}$$

$$B_2 = (\rho_{g'g'}^{(0)} - \rho_{e'e'}^{(0)}) \left\{ \left[\omega_o - \omega + k_j \cdot \mathbf{v} - i\Gamma_{e'g'} \right] \left[(k_j - k_2) \cdot \mathbf{v} - i\Gamma_{ee} \right] \left[\omega_o - \omega + k_4 \cdot \mathbf{v} - i\Gamma_{e'g} \right] \right\}^{-1}, \tag{23c}$$

and

60

$$B_3 = \left(\rho_{g'g}^{(0)} - \rho_{ee}^{(0)}\right)\left\{ \left[\omega_o - \omega + k_2 \cdot v + i\Gamma_{eg'}\right]\left[(k_j - k_2)\cdot v - i\Gamma_{e'e}\right]\left[\omega_o - \omega + k_4 \cdot v - i\Gamma_{e'g}\right] \right\}^{-1}. \quad (23d)$$

In Eq. (22), N is the total number of absorbers, the ket $|n\rangle$ represents the total molecular wave function for the quantum level characterized by total angular momentum $\mathbf{J_n}$, μ is the electric dipole moment operator, and A, B_1, B_2, and B_3 represent energy-resonant denominators. In Eqs. (23a)-(23d), $\rho_{nn}^{(0)}$ is the initial density matrix element for the magnetic sublevel M_n of the level n and refers to the initial probability of the system being in that sublevel, $\hbar\omega_o$ is the energy difference between the levels e and g, k_j is the propagation vector of the field label j, $\mathbf{v}$ is the velocity vector of the absorbing molecule, and Γ_{nm} represents the total dephasing rate of the coherence between the magnetic sublevels M_n and M_m.

We seek to evaluate Eqs. (21)-(23) using a spherical tensor formalism and to express the DFWM third-order nonlinear polarization in terms of its multipole components. This method provides a well-developed and efficient way of using the inherent symmetry of the system and enables dynamic and geometric factors to be separated from each other. The evaluation is similar to that of coherent LIF by Greene and Zare (GZ)[2] with the exception that four photons are involved. This greater complexity, however, does not significantly increase the difficulty of solving the problem, which illustrates the power of the spherical tensor method.

The first step in the evaluation is to recognize that the summation over projections onto the several degenerate sublevels of the level n constitutes a single projection operator indicated by

$$P = \sum_{M_n} |n\rangle\langle n| = 1, \quad (24)$$

which is scalar (tensor of rank 0). Substituting Eq. (24) into the first term of Eq. (22) gives

$$\sum_{M_g} \langle g | \hat{O} | g \rangle, \quad (25)$$

where

$$\hat{O} = \left(\varepsilon_4^* \cdot \mu_4\right)\left(\varepsilon_j \cdot \mu_j\right)\left(\varepsilon_2^* \cdot \mu_2\right)\left(\varepsilon_i \cdot \mu_i\right), \quad (26)$$

and the energy-resonant denominators have been omitted for simplicity. The transition dipole moment operators μ have been subscripted for bookkeeping. The tensor product in Eq. (26) has four dipole (rank 1) terms that can be organized in various ways to produce a

61

tensor of rank 4. In DFWM, however, the process initiates and terminates in the same level, denoted here as $|\alpha_n J_n M_n\rangle$, where M_n is the projection of the total angular momentum $\mathbf{J_n}$ (quantum number J_n) on the space-fixed Z-axis, and α_n represents all other quantum numbers, i.e., electronic and vibrational. The only operator $\hat{O}$ that can connect the ket $|\alpha_n J_n M_n\rangle$ to the bra $\langle \alpha_n J_n M_n|$ is a scalar, c, i.e.,

$$\langle \alpha_n J_n M_n |\hat{O}|\alpha_n J_n M_n\rangle = \langle \alpha_n J_n M_n |c|\alpha_n J_n M_n\rangle = c \tag{27}$$

because any higher rank tensor will cause the matrix element to vanish. A tensor of rank zero can be formed by contracting tensors of higher and equal rank. For example two tensors of rank 1 (vectors) make a tensor of rank 0 by the vector dot product. Similarly, two vectors of rank two (quadrupoles) can also be contracted. Recall that Eq. (26) has four dipole (rank 1) terms that can be organized in various ways, for instance as a tensor product of three dipoles to form tensors up to rank 3 and a single dipole of rank 1. However this tensor product cannot be contracted to form a scalar. Therefore we organize Eq. (26) in terms of tensor products of two dipoles to form tensors up to rank 2 which can be contracted to give a scalar. The resulting expressions are readily interpreted using the grating picture of DFWM. We note here, however, that higher-order tensors will contribute to the DFWM signal as the laser intensity approaches saturation. In a perturbative treatment, an increase in the laser intensity is accounted for by including higher order terms in the perturbative expansion, i.e., χ^5, $\chi^7, \chi^9, \ldots \chi^n$. These additional terms contain matrix element products with 6, 8, 10, ... $n+1$ factors and can form tensors up to rank $(n+1)/2$.

The spherical tensor convention adopted here is that of Zare.[3] Below $\otimes$ refers to the tensor product and $\times$ refers to scalar multiplication. We begin by expressing the vector dot product involved in the electric dipole interaction in spherical tensor notation:

$$(\boldsymbol{\varepsilon} \cdot \boldsymbol{\mu}) = -\sqrt{3}\left[\varepsilon^{(1)} \otimes \mu^{(1)}\right]_0^{(0)} = \sum_\varrho (-1)^\varrho \varepsilon_\varrho^{(1)} \mu_{-\varrho}^{(1)}, \tag{28}$$

where the general expression for the scalar product is

$$\left[T^{(K)} \otimes V^{(K)}\right]_0^{(0)} = \sum_\varrho (-1)^{K-\varrho}(2K+1)^{-\frac{1}{2}} T_\varrho^{(K)} V_{-\varrho}^{(K)}. \tag{29}$$

In Eqs. (28) and (29) each vector is written in terms of its spherical tensor components. See the Appendix. The product of two dipole terms is

$$\left(\varepsilon_i^* \cdot \boldsymbol{\mu}_i\right)\left(\varepsilon_j \cdot \boldsymbol{\mu}_j\right) = 3 \left[\left[\varepsilon_i^{*(1)} \otimes \mu_i^{(1)}\right]^{(0)} \otimes \left[\varepsilon_j^{(1)} \otimes \mu_j^{(1)}\right]^{(0)}\right]_0^{(0)}$$

$$= 3 \langle(11)K(11)K0|(11)0(11)00\rangle \sum_K \left[\left[\varepsilon_i^{*(1)} \otimes \varepsilon_j^{(1)}\right]^{(K)} \otimes \left[\mu_i^{(1)} \otimes \mu_j^{(1)}\right]^{(K)}\right]_0^{(0)}, \quad (30)$$

where the operators have been regrouped using the recoupling transformation of four angular momenta. The summation over K in Eq. (30) is from $K=0$ to $K=2$ because the tensor product of two dipoles can form a scalar (the dot product), a vector (the cross product), or a tensor of rank 2. The factor in angular brackets is a recoupling coefficient and involves a 9-j symbol, three of whose arguments are zero. This coefficient has been evaluated (GZ Eq. (37)) and has the general form

$$\langle(KK')K''(KK')K''0|(KK)0(K'K')00\rangle = (2K+1)^{-\frac{1}{2}}(2K'+1)^{-\frac{1}{2}}(2K''+1)^{\frac{1}{2}}. \quad (31)$$

The operator $\hat{O}$ defined in Eq. (26) can be represented using Eqs. (30) and (31) as

$$\hat{O} = \sum_{K,K'}(2K+1)^{\frac{1}{2}}(2K'+1)^{\frac{1}{2}}$$

$$\times \left[\left[\left[\varepsilon_4^{*(1)} \otimes \varepsilon_j^{(1)}\right]^{(K)} \otimes \left[\mu_4^{(1)} \otimes \mu_j^{(1)}\right]^{(K)}\right]^{(0)} \otimes \left[\left[\varepsilon_2^{*(1)} \otimes \varepsilon_i^{(1)}\right]^{(K')} \otimes \left[\mu_2^{(1)} \otimes \mu_i^{(1)}\right]^{(K')}\right]^{(0)}\right]_0^{(0)}, \quad (32)$$

and with one more recoupling transformation all of the polarization factors can be grouped together. Performing this transformation gives

$$\hat{O} = \sum_{K,K',K''}(2K+1)^{\frac{1}{2}}(2K'+1)^{\frac{1}{2}}\langle(KK')K''(KK')K''0|(KK)0(K'K')00\rangle$$

$$\times \left[\left[\left[\varepsilon_4^{*(1)} \otimes \varepsilon_j^{(1)}\right]^{(K)} \otimes \left[\varepsilon_2^{*(1)} \otimes \varepsilon_i^{(1)}\right]^{(K')}\right]^{(K'')} \otimes \left[\left[\mu_4^{(1)} \otimes \mu_j^{(1)}\right]^{(K)} \otimes \left[\mu_2^{(1)} \otimes \mu_i^{(1)}\right]^{(K')}\right]^{(K'')}\right]_0^{(0)} \quad (33)$$

which can be simplified using Eq. (31) and expanded in terms of its tensor components by Eq. (29) to yield

$$\hat{O} = \sum_{K,K',K'',Q''}(-1)^{K''-Q''}\left[\left[\varepsilon_4^{*(1)} \otimes \varepsilon_j^{(1)}\right]^{(K)} \otimes \left[\varepsilon_2^{*(1)} \otimes \varepsilon_i^{(1)}\right]^{(K')}\right]_{Q''}^{(K'')}$$

$$\times \left[\left[\mu_4^{(1)} \otimes \mu_j^{(1)}\right]^{(K)} \otimes \left[\mu_2^{(1)} \otimes \mu_i^{(1)}\right]^{(K')}\right]_{-Q''}^{(K'')}. \quad (34)$$

63

Equation (34) is the same as Eq. (39) of GZ for LIF with the important distinction that four different electric fields are involved. Recalling that only a scalar operator, i.e., a tensor of rank $K''=0$, can connect the ket $|\alpha_n J_n M_n\rangle$ to the bra $\langle\alpha_n J_n M_n|$, we have $K=K'$ because only two tensors of equal rank can be contracted to form a scalar. Therefore the summation over K, K', and K'' of Eq. (34) is replaced with a single summation over K. Substituting into Eq. (25) gives a key result, namely,

$$\sum_{M_g}\left\langle \alpha_g J_g M_g \left| \hat{O} \right| \alpha_g J_g M_g \right\rangle = \sum_{K}\left\{ \left[\left[\varepsilon_4^{*(1)}\otimes\varepsilon_j^{(1)}\right]^{(K)}\otimes\left[\varepsilon_2^{*(1)}\otimes\varepsilon_i^{(1)}\right]^{(K)}\right]_0^{(0)}\right.$$

$$\left.\times\sum_{M_g}\left\langle\alpha_g J_g M_g\left|\left[\left[\mu_4^{(1)}\otimes\mu_j^{(1)}\right]^{(K)}\otimes\left[\mu_2^{(1)}\otimes\mu_i^{(1)}\right]^{(K)}\right]_0^{(0)}\right|\alpha_g J_g M_g\right\rangle\right\}, \quad (35)$$

where K can have values of 0, 1 and 2 (the range of K and K'), and the shorthand notation for the molecular wave functions $|n\rangle$ has been replaced with $|\alpha_n J_n M_n\rangle$. Equation (35) displays the disentanglement of the geometric aspects (polarization tensors) of the problem from the dynamics (transition moment tensors) of the electric dipole interaction.

The first factor of Eq. (35) represents the scalar contraction of two polarization tensors to form a scalar and is essentially in its most fundamental form. The explicit evaluation of this factor is straightforward and is shown in the Appendix. The second factor of Eq. (35), on the other hand, can be reduced to a more fundamental form. Applying the Wigner-Eckart theorem (Zare Eq. (5.14)) yields after some simplification

$$\sum_{M_g}\left\langle\alpha_g J_g M_g\left|\left[\left[\mu_4^{(1)}\otimes\mu_j^{(1)}\right]^{(K)}\otimes\left[\mu_2^{(1)}\otimes\mu_i^{(1)}\right]^{(K)}\right]_0^{(0)}\right|\alpha_g J_g M_g\right\rangle$$

$$=\left(2J_g+1\right)^{1/2}\left\langle\alpha_g J_g\left\|\left[\left[\mu_4^{(1)}\otimes\mu_j^{(1)}\right]^{(K)}\otimes\left[\mu_2^{(1)}\otimes\mu_i^{(1)}\right]^{(K)}\right]^{(0)}\right\|\alpha_g J_g\right\rangle. \quad (36)$$

The last factor of Eq. (36) is the reduced matrix element of a compound tensor operator and can be evaluated using the following relation (Zare Eq. (5.74))

$$\left\langle \alpha J \left\| X^{(K)} \right\| \alpha' J' \right\rangle$$

$$=\left\langle \alpha J \left\| \left[T^{(K_1)}\otimes T^{(K_2)}\right]^{(K)} \right\| \alpha' J' \right\rangle$$

$$= (-1)^{K+J+J'} (2K+1)^{\frac{1}{2}} \sum_{\alpha''J''} \begin{Bmatrix} K_1 & K_2 & K \\ J' & J' & J'' \end{Bmatrix} \langle \alpha J \| T^{(K_1)} \| \alpha''J'' \rangle \langle \alpha''J'' \| T^{(K_1)} \| \alpha'J' \rangle . \quad (37)$$

where the term in curly brackets is a 6-j symbol. Applying Eq. (37) to (36) gives the following result after some simplification

$$\sum_{M_g} \langle \alpha_g J_g M_g | \left[\left[\mu_4^{(1)} \otimes \mu_j^{(1)} \right]^{(K)} \otimes \left[\mu_2^{(1)} \otimes \mu_i^{(1)} \right]^{(K)} \right]_0^{(0)} | \alpha_g J_g M_g \rangle$$

$$= (-1)^{K+J_g} (2K+1)^{\frac{1}{2}} \sum_{\alpha J} \sum_{\alpha'J'} \sum_{\alpha''J''} (-1)^{3J} \begin{Bmatrix} J & J & K \\ 1 & 1 & J' \end{Bmatrix} \begin{Bmatrix} J_g & J_g & K \\ 1 & 1 & J'' \end{Bmatrix}$$

$$\times \langle \alpha_g J_g \| \mu_4^{(1)} \| \alpha'J' \rangle \langle \alpha'J' \| \mu_j^{(1)} \| \alpha J \rangle \langle \alpha J \| \mu_2^{(1)} \| \alpha''J'' \rangle \langle \alpha''J'' \| \mu_i^{(1)} \| \alpha_g J_g \rangle . \quad (38)$$

For fully resonant DFWM we have assumed that the excitation bandwidth is sufficiently narrow compared to the density of states (including Doppler broadening) of the absorbing species so that the interaction is exclusively between the degenerate magnetic sublevels of the two levels involved in the one-photon resonant transition. Therefore the electric dipole operators in Eq. (38) can only connect $\mathbf{J_g} \leftrightarrow \mathbf{J_e}$, i.e., $J'' \to J_e$, $J \to J_g$, and $J' \to J_e$, and Eq. (38) simplifies to

$$\sum_{M_g} \langle \alpha_g J_g M_g | \left[\left[\mu_4^{(1)} \otimes \mu_j^{(1)} \right]^{(K)} \otimes \left[\mu_2^{(1)} \otimes \mu_i^{(1)} \right]^{(K)} \right]_0^{(0)} | \alpha_g J_g M_g \rangle$$

$$= (-1)^K (2K+1)^{\frac{1}{2}} \begin{Bmatrix} J_g & J_g & K \\ 1 & 1 & J_e \end{Bmatrix}^2 \left| \langle \alpha_e J_e \| \mu^{(1)} \| \alpha_g J_g \rangle \right|^4 \quad (39)$$

where the labels on the electric dipole moment operator have been dropped. The square of the reduced matrix element $\langle \alpha_e J_e \| \mu^{(1)} \| \alpha_g J_g \rangle$ is the molecular line strength $S(\alpha_g J_g; \alpha_e J_e)$ of the $g \leftrightarrow e$ transition, i.e.,

$$S(\alpha_g J_g; \alpha_e J_e) = \left| \langle \alpha_e J_e \| \mu^{(1)} \| \alpha_g J_g \rangle \right|^2 = \left| \langle \alpha_g J_g \| \mu^{(1)} \| \alpha_e J_e \rangle \right|^2 . \quad (40)$$

Equation (40) is often expressed (Zare pp. 283-290 and 312-315) as

$$S(\alpha_g J_g; \alpha_e J_e) = S_{J_g J_e}^{\alpha} S_{J_g J_e}^{R} \quad (41)$$

where $S_{J_g J_e}^{\alpha}$ is the strength of the $\alpha_g \leftrightarrow \alpha_e$ vibronic band (in many cases simply the product of the Franck-Condon factor(s) and the square of the electronic transition moment), and $S_{J_g J_e}^{R}$ is the rotational line strength (Hönl-London factor).

65

Equations (29), (35), and (39) are used to express the key result

$$\sum_{M_g} \left\langle \alpha_g J_g M_g \left| \hat{O} \right| \alpha_g J_g M_g \right\rangle$$

$$= \left| \left\langle \alpha_e J_e \left\| \mu^{(1)} \right\| \alpha_g J_g \right\rangle \right|^4 \sum_K \left\{ \begin{matrix} J_g & J_g & K \\ 1 & 1 & J_e \end{matrix} \right\}^2 \sum_{Q=-K}^{K} (-1)^Q \left[\varepsilon_4^{*(1)} \otimes \varepsilon_j^{(1)} \right]_Q^{(K)} \left[\varepsilon_2^{*(1)} \otimes \varepsilon_i^{(1)} \right]_{-Q}^{(K)}. \quad (42)$$

The first factor of Eq. (42) represents the dependence of the DFWM signal intensity on the dynamics of the electric dipole interaction, i.e., the greater the line strength of the molecular transition, the larger the DFWM signal intensity. The second factor of Eq. (42) represents the dependence of the DFWM signal intensity on the level degeneracies and the polarization vectors of the electric fields.

The final step in the derivation of the macroscopic polarization is to average over the initial molecular distribution. For an isotropic gas all of the magnetic sublevels of a given level are equally populated ($\rho_{nn} = \rho_{n'n'}$), and no phase relation exists between levels. Therefore the average consists of integrating over the velocity distribution of the absorbing molecules, which is defined as follows

$$N = \int N(\mathbf{v}) d^3 v = N \int f(\mathbf{v}) d^3 v . \quad (43)$$

In most experiments $f(\mathbf{v})$ is the normalized Maxwell-Boltzmann velocity distribution. Using Eqs. (20)-(23) and the identity

$$\left[T^{(1)} \otimes V^{(1)} \right]_Q^{(K)} = (-1)^K \left[V^{(1)} \otimes T^{(1)} \right]_Q^{(K)}, \quad (44)$$

the scalar amplitude of the macroscopic polarization becomes

$$\wp_{DFWM}^{(3)} = \frac{N}{8\hbar^3} \left(\rho_{gg}^{(0)} - \rho_{ee}^{(0)} \right) \left| \left\langle \alpha_e J_e \left\| \mu^{(1)} \right\| \alpha_g J_g \right\rangle \right|^4 \mathcal{E}_1 \mathcal{E}_2^* \mathcal{E}_3$$

$$\times \left\{ \sum_K L_{12}^g(\omega, K) \left\{ \begin{matrix} J_g & J_g & K \\ 1 & 1 & J_e \end{matrix} \right\}^2 \sum_{Q=-K}^{K} (-1)^Q \left[\varepsilon_4^{*(1)} \otimes \varepsilon_3^{(1)} \right]_Q^{(K)} \left[\varepsilon_2^{*(1)} \otimes \varepsilon_1^{(1)} \right]_{-Q}^{(K)} \right.$$

$$\left. + \sum_K L_{12}^e(\omega, K) \left\{ \begin{matrix} J_e & J_e & K \\ 1 & 1 & J_g \end{matrix} \right\}^2 \sum_{Q=-K}^{K} (-1)^Q \left[\varepsilon_4^{*(1)} \otimes \varepsilon_3^{(1)} \right]_Q^{(K)} \left[\varepsilon_2^{*(1)} \otimes \varepsilon_1^{(1)} \right]_{-Q}^{(K)} \right.$$

$$+ \sum_K L^g_{32}(\omega,K) \begin{Bmatrix} J_g & J_g & K \\ 1 & 1 & J_e \end{Bmatrix}^2 \sum_{Q=-K}^{K} (-1)^Q \left[\varepsilon_4^{*(1)} \otimes \varepsilon_1^{(1)} \right]_Q^{(K)} \left[\varepsilon_2^{*(1)} \otimes \varepsilon_3^{(1)} \right]_{-Q}^{(K)}$$

$$+ \sum_K L^e_{32}(\omega,K) \begin{Bmatrix} J_e & J_e & K \\ 1 & 1 & J_g \end{Bmatrix}^2 \sum_{Q=-K}^{K} (-1)^Q \left[\varepsilon_4^{*(1)} \otimes \varepsilon_1^{(1)} \right]_Q^{(K)} \left[\varepsilon_2^{*(1)} \otimes \varepsilon_3^{(1)} \right]_{-Q}^{(K)} \Bigg\}, \quad (45)$$

where the line shape factors have the form

$$L^n_{j2}(\omega,K) = \int \frac{f(\mathbf{v})d^3\mathbf{v}}{[(\mathbf{k}_j - \mathbf{k}_2)\cdot\mathbf{v} - i\Gamma_n(K)]} \left\{ \frac{1}{[\omega_o - \omega + \mathbf{k}_j\cdot\mathbf{v} - i\Gamma_{eg}]} - \frac{1}{[\omega_o - \omega + \mathbf{k}_2\cdot\mathbf{v} + i\Gamma_{eg}]} \right\} \frac{1}{[\omega_o - \omega + \mathbf{k}_4\cdot\mathbf{v} - i\Gamma_{eg}]}. \quad (46)$$

In Eq. (45), the $K=0$, 1 and 2 terms describe the (scalar) population, (dipolar) orientation, and (quadupolar) alignment, respectively, and in Eq. (46) the phenomenological relaxation rates $\Gamma_n(K)$ of the spherical tensor representation have replaced the $\Gamma_{n'n}$ rates. The $\Gamma_n(K)$ are defined as follows: $\Gamma_n(0)$ is the relaxation rate of the global population of the nth level, and $\Gamma_n(K=1)$ and $\Gamma_n(K=2)$ are the relaxation rates of the molecular orientation and alignment of the nth level, respectively. Furthermore we considered only collisional relaxation of the molecular system (no spontaneous emission), and we made the reasonable assumption that for a dipolar transition $\Gamma_{e'g'} = \Gamma_{e'g} = \Gamma_{eg'} = \Gamma_{eg}$, i.e., that only one optical relaxation rate need be considered.[63] As written, the specific collisional relaxation rates are dependent on temperature but independent of velocity.

Equation (45) together with Eq. (46) represents the general solution to the DFWM third-order polarization for molecular systems (no hyperfine structure) excited by electric dipole radiation in the weak-field limit and can be evaluated explicitly for the phase matching geometry and polarization configuration of interest. Physically, the third-order DFWM polarization of Eq. (45) is interpreted as resulting from the contributions of four terms: the first term represents the contribution of the diffraction of wave 3 from a ground-state grating formed by fields 1 and 2, the second term represents the contribution of the diffraction of wave 3 from an excited-state grating formed by fields 1 and 2, the third term represents the contribution of the diffraction of wave 1 from a ground-state grating formed by fields 3 and 2, and the fourth term represents the contribution of the diffraction of wave 1 from an excited-state grating formed by fields 3 and 2. In addition the multipole components can be interpreted as ground- and excited-state population, orientation, alignment gratings for $K=0$, 1, and 2, respectively. This treatment demonstrates that in the most general case the DFWM signal may be regarded as arising

from the contributions of twelve different gratings! The gratings can be distinguished by spacing (Δk_{12} or Δk_{32}), by the level in which the grating is formed (ground or excited), and by the multipole nature of the grating (population, orientation, or alignment).

To complete our derivation, Eq. (45) is substituted into Eq. (19) to yield the expression[64] for the DFWM signal intensity:

$$
I_{DFWM} \propto \left[N_g - \frac{(2J_g+1)}{(2J_e+1)} N_e \right]^2 \left[B_{ge}(J_g, J_e) \right]^4 I_1 I_2 I_3
$$

$$
\times \Bigg| \sum_K L^g_{12}(\omega, K) G(J_g, J_e; K) F(\varepsilon_4, \varepsilon_1, \varepsilon_3, \varepsilon_2; K)
$$

$$
+ \sum_K L^e_{12}(\omega, K) G(J_e, J_g; K) F(\varepsilon_4, \varepsilon_1, \varepsilon_3, \varepsilon_2; K)
$$

$$
+ \sum_K L^g_{32}(\omega, K) G(J_g, J_e; K) F(\varepsilon_4, \varepsilon_3, \varepsilon_1, \varepsilon_2; K)
$$

$$
+ \sum_K L^e_{32}(\omega, K) G(J_e, J_g; K) F(\varepsilon_4, \varepsilon_3, \varepsilon_1, \varepsilon_2; K) \Bigg|^2, \qquad (47)
$$

where the following substitutions have been made:

$$
N_g - \frac{(2J_g+1)}{(2J_e+1)} N_e = N\left(2J_g + 1\right)\left(\rho^{(0)}_{gg} - \rho^{(0)}_{ee}\right), \qquad (48)
$$

$$
\left[B_{ge}(J_g, J_e) \right]^2 = \left[\frac{\pi}{3\varepsilon_0 \hbar^2} \right]^2 \frac{\left| \langle \alpha_e J_e \| \mu^{(1)} \| \alpha_g J_g \rangle \right|^4}{(2J_g+1)^2}, \qquad (49)
$$

$$
G(J, J'; K) = (2J_g + 1) \left\{ \begin{matrix} J & J & K \\ 1 & 1 & J' \end{matrix} \right\}^2, \qquad (50)
$$

and

$$
F(\varepsilon_4, \varepsilon_i, \varepsilon_j, \varepsilon_2; K) = \sum_{Q=-K}^{K} (-1)^Q \left[\varepsilon_4^{*(1)} \otimes \varepsilon_j^{(1)} \right]_Q^{(K)} \left[\varepsilon_2^{*(1)} \otimes \varepsilon_i^{(1)} \right]_{-Q}^{(K)}. \qquad (51)
$$

In Eq. (50) the $G(J, J'; K)$ factors are simply 6-j symbols and depend only on K, J_g, and J_e. These values are listed in Table 3.4 as a function of transition type. Conversely, the

68

Table 3.4. Analytic expressions for $G(J,J';K) = (2J_g+1)\begin{Bmatrix} J & J & K \\ 1 & 1 & J' \end{Bmatrix}^2$ as a function of transition type and K value.

$J'-J$	$G(J,J';0)$	$G(J,J';1)$	$G(J,J';2)$
-1	$\frac{1}{3}\left[\frac{(2J_g+1)}{(2J+1)}\right]$	$\frac{1}{6}\left[\frac{(J+1)}{J}\right]\left[\frac{(2J_g+1)}{(2J+1)}\right]$	$\frac{1}{30}\left[\frac{(2J+3)(J+1)}{J(2J-1)}\right]\left[\frac{(2J_g+1)}{(2J+1)}\right]$
0	$\frac{1}{3}\left[\frac{(2J_g+1)}{(2J+1)}\right]$	$\frac{1}{6}\left[\frac{1}{J(J+1)}\right]\left[\frac{(2J_g+1)}{(2J+1)}\right]$	$\frac{1}{30}\left[\frac{(2J+3)(2J-1)}{J(J+1)}\right]\left[\frac{(2J_g+1)}{(2J+1)}\right]$
+1	$\frac{1}{3}\left[\frac{(2J_g+1)}{(2J+1)}\right]$	$\frac{1}{6}\left[\frac{J}{(J+1)}\right]\left[\frac{(2J_g+1)}{(2J+1)}\right]$	$\frac{1}{30}\left[\frac{J(2J-1)}{(2J+3)(J+1)}\right]\left[\frac{(2J_g+1)}{(2J+1)}\right]$

Table 3.5. Analytic expressions for $F(\varepsilon_4,\varepsilon_i,\varepsilon_j,\varepsilon_2;K) = \displaystyle\sum_{Q=-K}^{K}(-1)^Q \left[\varepsilon_4^{*(1)}\otimes\varepsilon_j^{(1)}\right]_Q^{(K)}\left[\varepsilon_2^{*(1)}\otimes\varepsilon_i^{(1)}\right]_{-Q}^{(K)}$ as a function of polarization configuration and K value.

$\varepsilon_4\varepsilon_i\varepsilon_j\varepsilon_2$	$F(\varepsilon_4,\varepsilon_i,\varepsilon_j,\varepsilon_2;0)$	$F(\varepsilon_4,\varepsilon_i,\varepsilon_j,\varepsilon_2;1)$	$F(\varepsilon_4,\varepsilon_i,\varepsilon_j,\varepsilon_2;2)$
RRRR	$\frac{1}{3}$	$\frac{1}{2}$	$\frac{1}{6}$
RLRL	$\frac{1}{3}$	$-\frac{1}{2}$	$\frac{1}{6}$
RRLL	0	0	1
YYYY	$\frac{1}{3}$	0	$\frac{2}{3}$
YXYX	$\frac{1}{3}$	0	$-\frac{1}{3}$
YYXX	0	$\frac{1}{2}$	$\frac{1}{2}$
YXXY	0	$-\frac{1}{2}$	$\frac{1}{2}$

70

$F(\varepsilon_4,\varepsilon_i,\varepsilon_j,\varepsilon_2;K)$ factors of Eq. (51) depend on the field polarizations but not on J_g and J_e. The polarization tensor products of Eq. (51) are evaluated in the Appendix, and the results for specific polarization cases treated in Sec. II are given in Table 3.5.

B. Equal Relaxation of the Multipole Moments

In Sec. II we assumed that the relaxation is isotropic and that all of the state multipoles relax at the same rate. For many experiments, population relaxation rates such as quenching are much larger than collisional rates that only perturb the magnetic sublevel distribution. Therefore, a single relaxation rate might be expected to characterize the nth level. Some experimental evidence supports this "single relaxation" assumption.[17,65]

Under the "single relaxation" assumption the line shape factors of Eq. (46) become K independent and take the form of Eq. (7) of Sec. IIA, i.e., $L_{j2}^n(\omega,K) \to L_{j2}^n(\omega)$. Removing the line shape factors from the summations of Eq. (47) gives the familiar expression of Eq. (2) with the total geometric factor $G_F^T(\varepsilon_4,\varepsilon_1,\varepsilon_3,\varepsilon_2;J_g,J_e;\omega)$ defined in terms of an expansion in K as

$$
G_F^T(\varepsilon_4,\varepsilon_1,\varepsilon_3,\varepsilon_2;J_g,J_e;\omega) = \frac{1}{\pounds(\omega)}\left\{ L_{12}^g(\omega)\sum_{K=0}G(J_g,J_e;K)F(\varepsilon_4,\varepsilon_1,\varepsilon_3,\varepsilon_2;K) \right.
$$

$$
+ L_{12}^e(\omega)\sum_{K}G(J_e,J_g;K)F(\varepsilon_4,\varepsilon_1,\varepsilon_3,\varepsilon_2;K)
$$

$$
+ L_{32}^g(\omega)\sum_{K}G(J_g,J_e;K)F(\varepsilon_4,\varepsilon_3,\varepsilon_1,\varepsilon_2;K)
$$

$$
\left. + L_{32}^e(\omega)\sum_{K}G(J_e,J_g;K)F(\varepsilon_4,\varepsilon_3,\varepsilon_1,\varepsilon_2;K) \right\}
$$

$$
= \sum_{K}G_F^{T(K)}(\varepsilon_4,\varepsilon_1,\varepsilon_3,\varepsilon_2;J_g,J_e;\omega), \tag{52}
$$

where the dependence of the line shape factors on collisions and phase matching is the same as in Sec. II. Equation (52) reduces to Eq. (4) of Sec. IIA because

$$\sum_K \begin{Bmatrix} J & J & K \\ 1 & 1 & J' \end{Bmatrix}^2 \sum_{Q=-K}^{K} (-1)^Q \left[\varepsilon_4^{*(1)} \otimes \varepsilon_j^{(1)} \right]_Q^{(K)} \left[\varepsilon_2^{*(1)} \otimes \varepsilon_i^{(1)} \right]_{-Q}^{(K)}$$

$$= \sum_K \begin{Bmatrix} J' & J' & K \\ 1 & 1 & J \end{Bmatrix}^2 \sum_{Q=-K}^{K} (-1)^Q \left[\varepsilon_4^{*(1)} \otimes \varepsilon_i^{(1)} \right]_Q^{(K)} \left[\varepsilon_2^{*(1)} \otimes \varepsilon_j^{(1)} \right]_{-Q}^{(K)}. \quad (53)$$

This identity is proven in Appendix A of reference 30. Equation (53) results from the fact the first four-photon matrix element product in Eq. (22) differs from the second product only in the ordering of the matrix elements. Because each matrix element is simply a complex number, it is immediately obvious that

$$\sum_{all\,M} \left\langle g \left| \varepsilon_4^* \cdot \mu \right| e' \right\rangle \left\langle e' \left| \varepsilon_j \cdot \mu \right| g' \right\rangle \left\langle g' \left| \varepsilon_2^* \cdot \mu \right| e \right\rangle \left\langle e \left| \varepsilon_i \cdot \mu \right| g \right\rangle$$

$$= \sum_{all\,M} \left\langle e' \left| \varepsilon_j \cdot \mu \right| g' \right\rangle \left\langle g' \left| \varepsilon_2^* \cdot \mu \right| e \right\rangle \left\langle e \left| \varepsilon_i \cdot \mu \right| g \right\rangle \left\langle g \left| \varepsilon_4^* \cdot \mu \right| e' \right\rangle. \quad (54)$$

Note however that the ordering of the angular momentum coupling is different for the two four-photon matrix element products of Eq. (54). From Eqs. (4), (52), and (53), the geometric factors are defined as

$$G_F\left(\varepsilon_4, \varepsilon_i, \varepsilon_j, \varepsilon_2; J_g, J_e\right) = \sum_K G(J_g, J_e; K)\, F(\varepsilon_4, \varepsilon_i, \varepsilon_j, \varepsilon_2; K)$$

$$= \sum_K G(J_e, J_g; K)\, F(\varepsilon_4, \varepsilon_j, \varepsilon_i, \varepsilon_2; K). \quad (55)$$

Equation (55) was used to generate the results found in Tables I-III.

The geometric factor $G_F^{T(K)}(\varepsilon_4, \varepsilon_1, \varepsilon_3, \varepsilon_2; J_g, J_e; \omega)$ of Eq. (52) is interpreted as being proportional to the total contribution of the 2^K multipole moment of the total angular momentum distribution to the DFWM signal amplitude along ε_4. We have plotted the $G_F^{T(K)}(\varepsilon_4, \varepsilon_1, \varepsilon_3, \varepsilon_2; J_g, J_e; \omega)$ for experimental conditions where $L_{12}^n(\omega) = L_{32}^n(\omega)$ and the upper and lower levels relax at the same rate, i.e., for the cases where the total geometric factor is decoupled from the collisional effects and phase matching geometry of the experiment. These results are shown in Figs. 5-8. Note that inherent in Eq. (52) is the assumption that the relaxation is isotropic and all of the state multipoles relax at the same
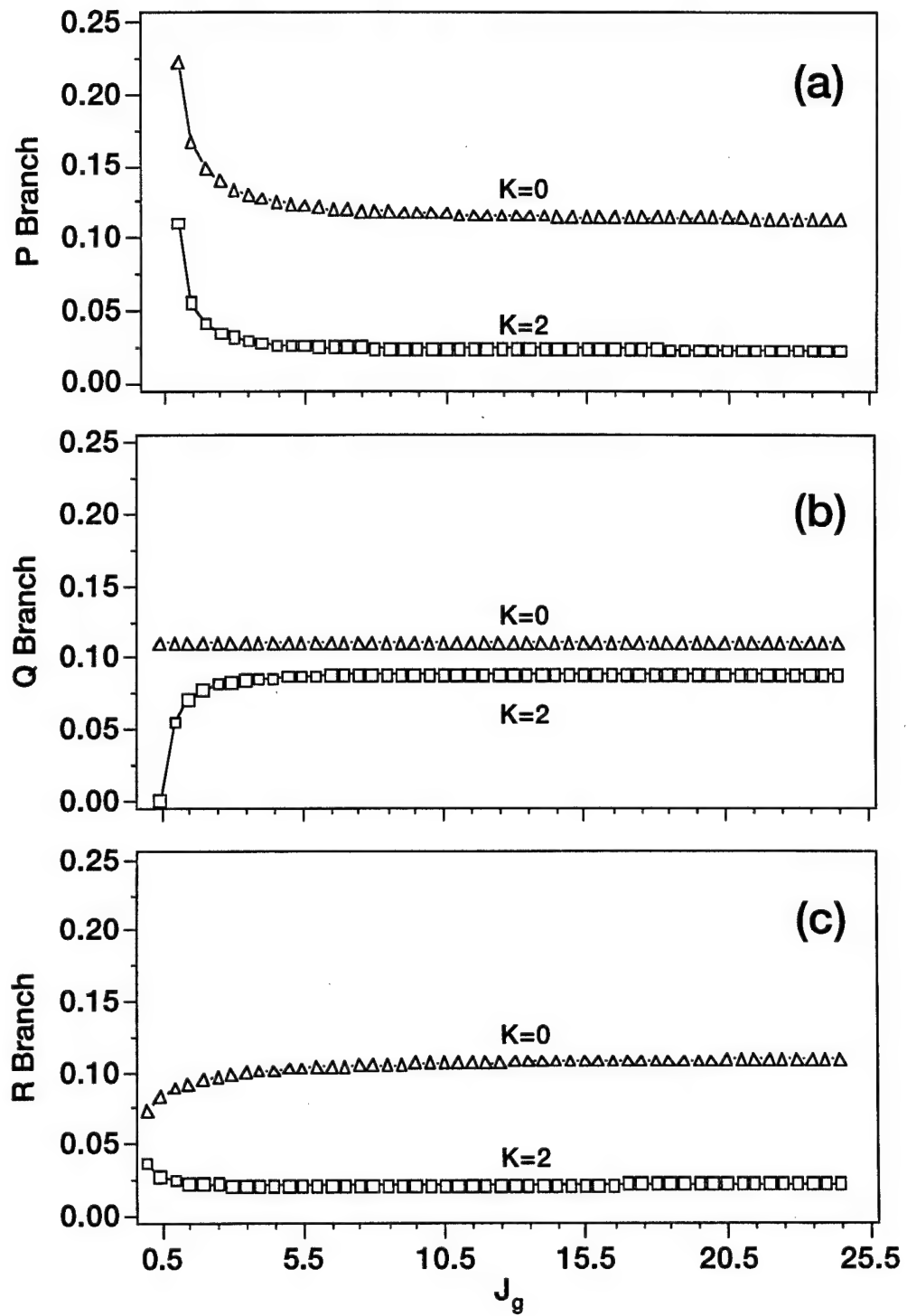
FIG. 3.5. Evaluated $G_F^{T(K)}(Y,Y,Y,Y;J_g,J_e;\omega)$ factors as a function of J_g for (a) P-branch, (b) Q-branch, and (c) R-branch transitions. Permuting $X \leftrightarrow Y$ does not change the plots. In the figure $-\triangle-$ and $-\square-$ correspond to $K = 0$ and 2, respectively.
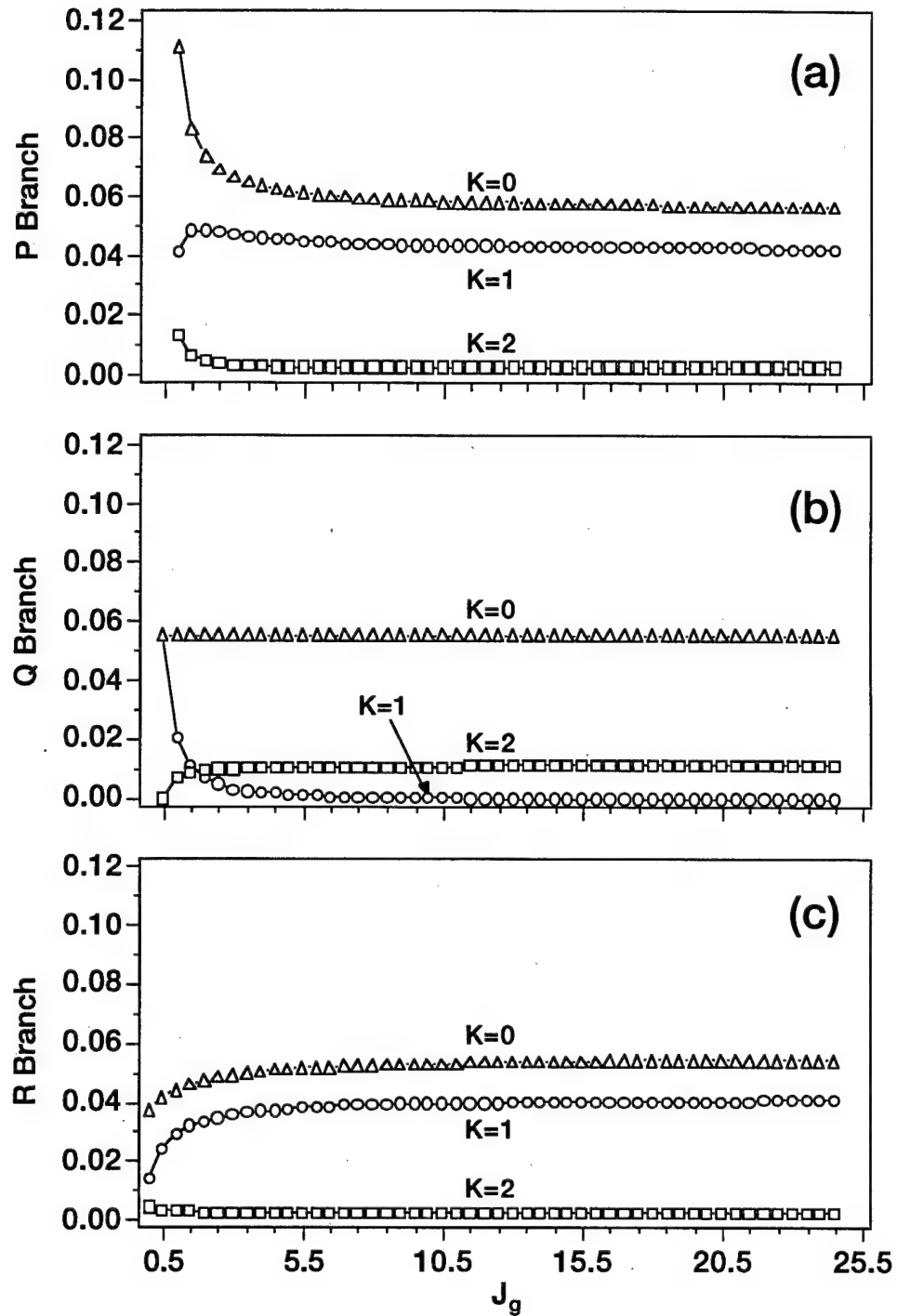
FIG. 3.6. Evaluated $G_F^{T(K)}(Y,X,Y,X;J_g,J_e;\omega) = G_F^{T(K)}(Y,Y,X,X;J_g,J_e;\omega)$
$= \frac{1}{2} G_F^{T(K)}(R,R,R,R;J_g,J_e;\omega)$ factors as a function of J_g for (a) P-branch, (b) Q-branch,
and (c) R-branch transitions. Permuting $X \leftrightarrow Y$ or $R \leftrightarrow L$ does not change the plots. In
the figure $-\Delta-$, $-O-$, and $-\square-$ correspond to $K = 0$, 1, and 2, respectively.

rate. The conditions that Figs. 5-8 describe are very specific; however, the discussion presented below can be extended to most experiments.

Figures 5 and 6 show the $G_F^{T(K)}(\varepsilon_4,\varepsilon_1,\varepsilon_3,\varepsilon_2;J_g,J_e;\omega)$ values as a function of J_g when the fields have identical polarizations, either linear (X or Y) or circular (R or L). According to the grating picture, interference of the grating-forming fields produces a spatial modulation of laser intensity with spacing given by Eq. (11). These intensity gratings are usually referred to as population gratings, but as can be seen in Figs. 5 and 6, the DFWM signal amplitude has significant contributions from higher-order moments. For instance, the population and alignment contributions to the DFWM signal amplitude for a Q-branch transition excited with linear polarized light (see Fig. 5b) are nearly equal! This and other effects can be understood by employing known concepts from linear spectroscopy to develop a qualitative picture of DFWM.

The first step is to recognize that, although the intensity is spatially modulated, the field polarization in these regions is preserved. Thus we can think of the initial isotropic distribution of absorbers interacting with polarized light in spatially distinct regions. For linearly polarized light, we would expect to create a spatial modulation of the population and alignment of the absorbers, i.e., population and alignment gratings. As shown in Fig. 5, only population and alignment gratings contribute. Likewise for circularly polarized light, we would expect to create a spatial modulation of the population, orientation, and alignment of the absorbers, i.e., population, orientation, and alignment gratings. Figure 6 shows that this expectation is indeed met.

Another interesting case involves linear polarized light in which both pump fields have the same polarization but are orthogonally polarized with respect to the probe field (see Fig. 7). The interference produced in this case is spatially uniform in intensity but spatially modulated in polarization. This polarization grating is typically referred to as a coherence grating because spatial population modulation does not exist. Under these circumstances only orientation and alignment contributions are expected, as confirmed in Fig. 7.

In Fig. 7 orientation gratings are found to dominate for $\Delta J = \pm 1$ transitions and alignment gratings dominate for $\Delta J = 0$ transitions. Furthermore, inspection of Figs. 6-8 shows that this conclusion is generally true. This behavior can be understood, again, if we consider the interaction of an isotropic distribution of molecules interacting with polarized light. After the absorption of linearly polarized light the system will be aligned, and after the absorption of circularly polarized light the system will be oriented and aligned. Q-

75
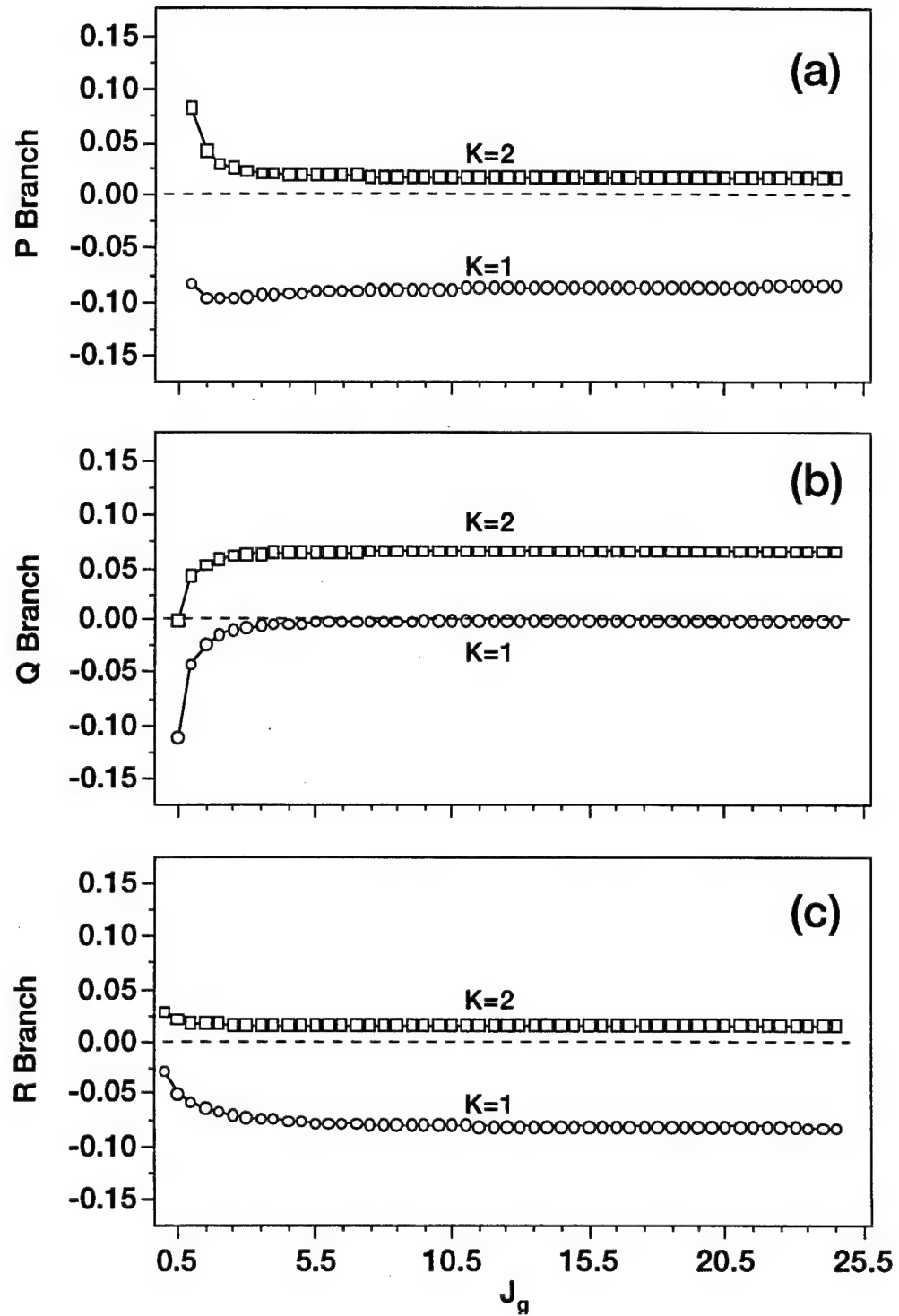
FIG. 3.7. Evaluated $G_F^{T(K)}(Y,X,X,Y;J_g,J_e;\omega)$ factors as a function of J_g for (a) P-branch, (b) Q-branch, and (c) R-branch transitions. Permuting $X \leftrightarrow Y$ does not change the plots. In the figure $-\text{o}-$ and $-\square-$ correspond to $K = 1$ and 2, respectively.
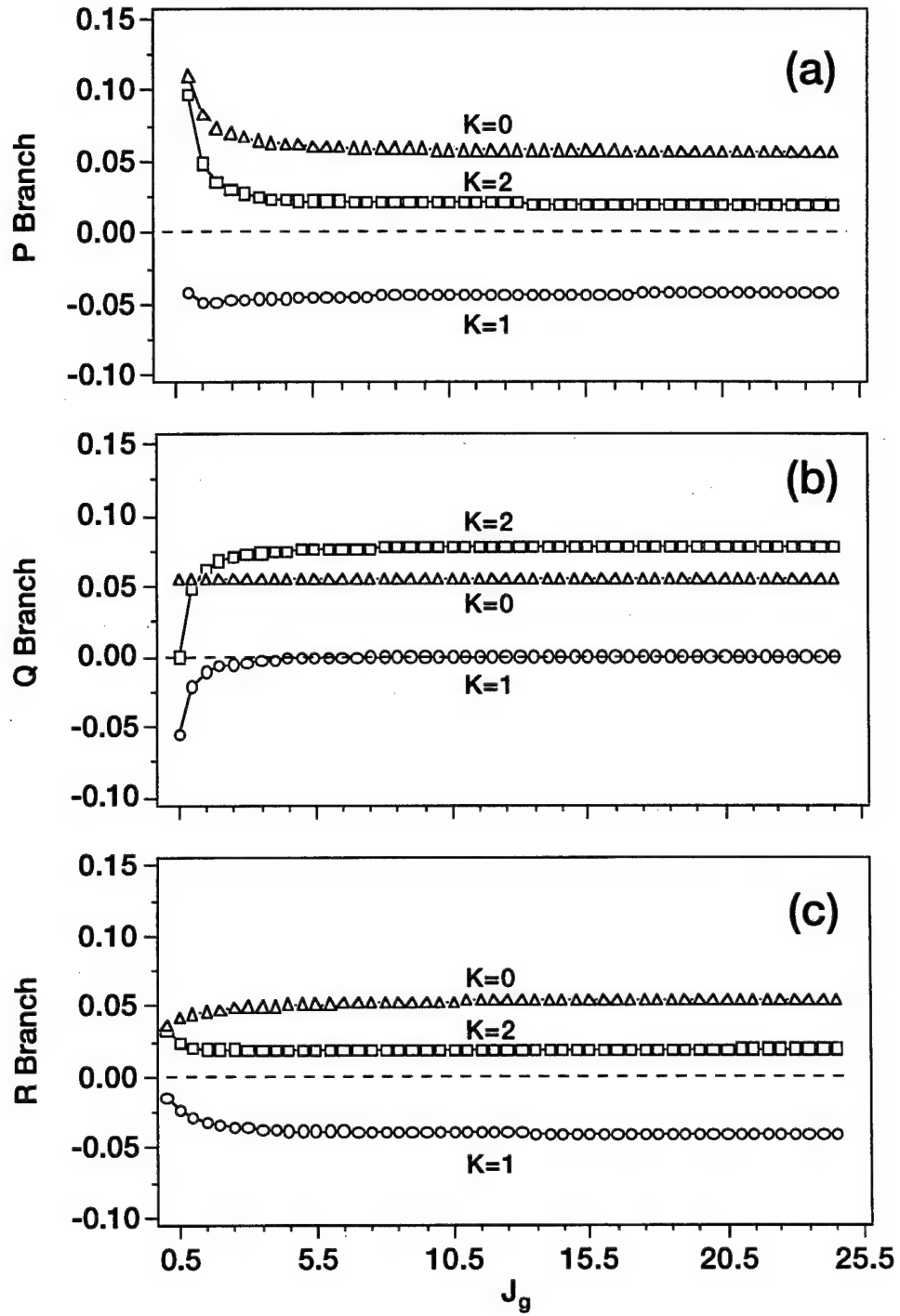
FIG. 3.8. Evaluated $G_F^{T(K)}(R,L,R,L;J_g,J_e;\omega) = G_F^{T(K)}(R,R,L,L;J_g,J_e;\omega)$ factors as a function of J_g for (a) P-branch, (b) Q-branch, and (c) R-branch transitions. Permuting $R \leftrightarrow L$ does not change the plots. In the figure $-\triangle-$, $-\text{o}-$, and $-\square-$ correspond to $K = 0$, 1, and 2, respectively.

branch transitions are more easily aligned than oriented, and the opposite is true for P- and R-branch transitions.

Finally, the most significant aspect of Figs. 5-8 is that the relative multipole moment contributions are very dependent on the value of J for low J values, but rapidly approach a high-J limit, i.e., for $J \geq 4$ the total geometric factor and its relative contributions are essentially independent of J. This behavior means that the J dependence of the DFWM signal intensity for a given branch (P, Q, or R) taken in a single polarization configuration will primarily reflect the J dependence of the one-photon absorption coefficient B_{ge} as well as any J-dependent relaxation effects. Molecules are often in the high-J limit, especially at flame and plasma temperatures at which J values ranging from 5 to 50 are typically populated.

C. Unequal Relaxation of the Multipole Moments

We have assumed thus far that the multipole moments relax at equal rates, which is a good approximation in flame experiments where efficient energy transfer collision partners, such as water, are present. We have recently observed[65] experimental conditions for which these rates are not the same, particularly for low values of J, in collisional environments in which light species such as helium are the dominant collision partners. Such species have slow inelastic collisional rates (quenching) compared with elastic collisional rates (depolarizing). The presence of unequal relaxation can be determined by polarization-ratio measurements.[17,65]

In the event that the multipole moments of the angular momentum distribution do not relax equally, the expressions for the DFWM signal intensity presented in Sec. II do not apply. If the relaxation is isotropic, however, the multipole moments relax independently, and the expressions presented in Sec. IIIA are valid. The effects of unequal relaxation has been discussed by Ducloy and Bloch[30] and is the topic of a future publication.[65] Finally if the relaxation is anisotropic, for example, the gas is in a static electric or magnetic field, then the situation is considerably more complicated.[34] Note, however, that the interpretation of DFWM signal intensities at this level of detail is not necessary for most applications.

IV. COMPARISON WITH PREVIOUS WORK

In what follows we attempt to place our work in the context of previous perturbative theoretical treatments of DFWM. Lam and Abrams (LA)[29] were among the first to describe the polarization effects for a degenerate two-level system. They used a density matrix approach to express the DFWM response as a summation of matrix element products that represented different coherences corresponding to contributions from normal population, cross-population, and Zeeman coherence mechanisms. Although this model provides an intuitive picture for the origin of the DFWM polarization effects, its application depends on the coordinate system chosen. This coordinate-frame dependence also makes the inclusion of collisional relaxation difficult, and LA acknowledged that an accurate description of the DFWM collisional effects in systems with degenerate sublevels necessitates the introduction of the irreducible (spherical tensor) representation of the density matrix.[56,57]

Such an approach was presented by Ducloy and Bloch (DB),[30] who discussed the DFWM response in terms of its irreducible tensor components. In their tensorial density matrix treatment, DB considered the degeneracy of the resonant levels, unequal relaxation of the magnetic sublevels, spontaneous emission (optical pumping), thermal motion, and the effect of pump-probe angular separation (noncollinear geometries). In later papers Berman, Steel, Khitrova, and Liu (BSKL)[31] and Alekseev[35] derived similar expressions that also included the effects of hyperfine structure. Together the work of DB, BSKL, and Alekseev illustrates the fundamental aspects of DFWM in the perturbative regime and represents general solutions of the problem. Unfortunately these studies have not been available to most experimentalists because the final results, expressed in density matrix notation, are quite complicated. Recently Kupiszewska and Whitaker (KW)[38] addressed this problem by specializing the treatment of BSKL to stationary diatomic molecules described by Hund's case (a) coupling with no hyperfine structure. The simplified expressions presented by KW provide some insight into the polarization effects in DFWM for molecular systems; however, the specialization of the treatment necessarily limits the applicability of the results.

An alternative approach to interpret DFWM signal intensities is to use diagrammatic perturbation theory (double-sided Feynman diagrams) to evaluate the DFWM polarization and collisional effects.[40,41,58] The diagrammatic method is equivalent to the density matrix formalism but has the advantage that the third-order nonlinear polarization can be evaluated directly without the need to calculate lower-order

processes. Using diagrammatic methods, Attal-Trétout, Monot, and Müller-Dethlefs (TMD)[33] and Aben, Ubachs, van der Zwan, and Hogervorst (AUZH)[36] have derived expressions for resonant CARS spectroscopy. This work focused on obtaining four-wave mixing line strength factors for diatomic molecules (omitting nuclear spin) to be used directly in the analysis of experimental signal intensities. Both TMD and AUZH note that the CARS expressions could be extended to describe DFWM, i.e., fully resonant CARS. We noted in Sec. II that the line strength factors themselves are dependent on the relaxation caused by the environment and not just angular momentum considerations. Consequently, this suggestion is correct only with qualification.

The general CARS expressions involve four distinct frequencies ω_1, ω_2, ω_3, and ω_4, and four independent states $|a\rangle$, $|b\rangle$, $|c\rangle$, $|d\rangle$ (labeled a, n, b, n' in TMD and a, b, c, d in AUZH). In the fully resonant case, $\omega_1 = \omega_2 = \omega_3 = \omega_4 = \omega$, and the four independent states converge to four distinct magnetic sublevels, i.e., $|a\rangle \to |g\rangle$, $|b\rangle \to |e\rangle$, $|c\rangle \to |g'\rangle$, and $|d\rangle = |e'\rangle$. This mapping leads to the inclusion of eight diagrams (eight more if $N_e \neq 0$) and four distinct resonant four-photon matrix element products, namely,

$$\sum_{all\, M} \langle g\, |\, \boldsymbol{\varepsilon}_4^* \cdot \boldsymbol{\mu} |e'\, \rangle \langle e'\, |\, \boldsymbol{\varepsilon}_3 \cdot \boldsymbol{\mu} |g'\, \rangle \langle g'\, |\, \boldsymbol{\varepsilon}_2^* \cdot \boldsymbol{\mu} |e\, \rangle \langle e\, |\, \boldsymbol{\varepsilon}_1 \cdot \boldsymbol{\mu} |g\, \rangle, \tag{56a}$$

$$\sum_{all\, M} \langle e'\, |\, \boldsymbol{\varepsilon}_3 \cdot \boldsymbol{\mu} |g'\, \rangle \langle g'\, |\, \boldsymbol{\varepsilon}_2^* \cdot \boldsymbol{\mu} |e\, \rangle \langle e\, |\, \boldsymbol{\varepsilon}_1 \cdot \boldsymbol{\mu} |g\, \rangle \langle g\, |\, \boldsymbol{\varepsilon}_4^* \cdot \boldsymbol{\mu} |e'\, \rangle, \tag{56b}$$

$$\sum_{all\, M} \langle g\, |\, \boldsymbol{\varepsilon}_4^* \cdot \boldsymbol{\mu} |e'\, \rangle \langle e'\, |\, \boldsymbol{\varepsilon}_1 \cdot \boldsymbol{\mu} |g'\, \rangle \langle g'\, |\, \boldsymbol{\varepsilon}_2^* \cdot \boldsymbol{\mu} |e\, \rangle \langle e\, |\, \boldsymbol{\varepsilon}_3 \cdot \boldsymbol{\mu} |g\, \rangle, \tag{56c}$$

and

$$\sum_{all\, M} \langle e'\, |\, \boldsymbol{\varepsilon}_1 \cdot \boldsymbol{\mu} |g'\, \rangle \langle g'\, |\, \boldsymbol{\varepsilon}_2^* \cdot \boldsymbol{\mu} |e\, \rangle \langle e\, |\, \boldsymbol{\varepsilon}_3 \cdot \boldsymbol{\mu} |g\, \rangle \langle g\, |\, \boldsymbol{\varepsilon}_4^* \cdot \boldsymbol{\mu} |e'\, \rangle. \tag{56d}$$

Equations (56a) and (56b) have the same value when summed over all M, but the ordering of the angular momentum coupling is different, and thus they represent different contributions from the zeroth, first, and second rank multipole moments. The same is true for Eqs. (56c) and (56d). The proper accounting of the multipole moment contributions, to our knowledge, has not been done using diagrammatic perturbation theory but has been done using density matrix approaches.[30,31,38] In addition Eqs. (56a) and (56c) appear quite similar, but have distinctly different values even when summed over all M, and the

same is true for Eqs. (56b) and (56d). Therefore care must be taken in extending CARS expressions to DFWM.

Bervas, Le Boiteux, Labrunie, and Attal-Trétout (BBLT)[37] and Freidman-Hill, Rahn, and Farrow (HRF)[39] recently reduced the CARS expressions to apply to DFWM. The expressions of BBLT contradict our results for BB- and PC-DFWM but agree fortuitously with our results for FB-DFWM. We offer the following explanation for these results. In Fig. 4 of BBLT, diagrams (a)-(d) describe the primary contributions to BB- and, PC-DFWM in the Doppler-broadened limit, and diagrams (a)-(h) describe the primarily contributions to FB-DFWM. Because BBLT do not distinguish between g and g' or e and e', all of the diagrams appear to be represented by the same matrix element product, namely Eq. (8) of BBLT. Diagrams (a) and (c) of BBLT Fig. 4 correspond to our Eq. (56a), diagrams (b) and (d) of BBLT Fig. 4 correspond to our Eq. (56c), diagrams (e) and (g) of BBLT Fig. 4 correspond to our Eq. (56b), and diagrams (f) and (h) of BBLT Fig. 4 correspond to our Eq. (56d). In terms of the notation developed in this chapter, the result of BBLT predicts the following proportionality for the BB- and PC-DFWM signal intensity:

$$I_{BB,PC} \propto \left| G_F(\varepsilon_4, \varepsilon_1, \varepsilon_3, \varepsilon_2; J_g, J_e)(L_{12}^g(\omega) + L_{12}^e(\omega)) \right|^2, \tag{57a}$$

which is independent of the difference in the relaxation rates of the g and e levels for all polarization configurations, whereas our treatment predicts that

$$I_{BB,PC} \propto \left| G_F(\varepsilon_4, \varepsilon_1, \varepsilon_3, \varepsilon_2; J_g, J_e)L_{12}^g(\omega) + G_F(\varepsilon_4, \varepsilon_3, \varepsilon_1, \varepsilon_2; J_g, J_e)L_{12}^e(\omega) \right|^2, \tag{57b}$$

which is dependent on the relative relaxation rates of the g and e levels whenever the two geometric factors differ (see Sec. II). Furthermore, our result, Eq. (57b), agrees with Eq. (45) of DB derived using a density matrix approach and experimental DFWM polarization ratios obtained in our laboratory for the CH radical.[17] The expressions for FB-DFWM presented by BBLT agree with our results because $L_{12}^g(\omega) = L_{32}^g(\omega)$ and $L_{12}^e(\omega) = L_{32}^e(\omega)$. In our notation, BBLT predict the following proportionality for the FB-DFWM signal intensity:

$$I_{FB} \propto \left| G_F(\varepsilon_4, \varepsilon_1, \varepsilon_3, \varepsilon_2; J_g, J_e)(L_{12}^g(\omega) + L_{12}^e(\omega)) + G_F(\varepsilon_4, \varepsilon_3, \varepsilon_1, \varepsilon_2; J_g, J_e))(L_{32}^g(\omega) + L_{32}^e(\omega)) \right|^2, \tag{58a}$$

which is equivalent to our result

$$I_{FB} \propto \left| G_F(\varepsilon_4, \varepsilon_1, \varepsilon_3, \varepsilon_2; J_g, J_e)(L_{12}^g(\omega) + L_{32}^e(\omega)) + G_F(\varepsilon_4, \varepsilon_3, \varepsilon_1, \varepsilon_2; J_g, J_e))(L_{12}^e(\omega) + L_{32}^g(\omega)) \right|^2, \tag{58b}$$

when $L_{12}^g(\omega) = L_{32}^g(\omega)$ and $L_{12}^e(\omega) = L_{32}^e(\omega)$. HRF considered three-level or "crossover" resonances that occur when two transitions that share a common level become resonant because of a simultaneous Doppler shift. HRF show that "crossover" resonances can influence DFWM signal intensities even if they are not spectroscopically resolved from their parent transitions. Such considerations could be important in spectrally congested regions with overlapping branches.

In summary, the work to date can be classified in two categories: first, density matrix approaches that emphasize the complex relation between polarization, collisional relaxation, and phase matching at the expense of simplicity; and second, diagrammatic approaches that focus on expressing the polarization effects (without specifying multipole contributions) analyticly while treating relaxation effects superficially. The emphasis of this chapter has been on the key aspects of interpreting molecular DFWM spectra in collisionally dominated environments because these types of experiments are those for which DFWM has found the largest application. In these experiments, hyperfine structure, spontaneous emission, and in most circumstances unequal relaxation of the multipole moments of the angular momentum distribution can be neglected so that relatively simple expressions are obtained without unnecessarily trivializing the treatment. Thus we have attempted to combine the best aspects of the two approaches by presenting analytic expressions with the relevant collision, velocity, and polarization considerations for the most-utilized experimental configurations. These expressions can be used directly in the evaluation of DFWM spectra for these specific cases. Finally the polarization tensor products evaluated in the Appendix can be used to extend the general expressions of Sec. IIIA to other experimental geometries of interest.

The above results were derived in the weak-field (no saturation) limit. An appealing aspect of DFWM is that in the saturation regime, the DFWM signal intensity becomes relatively insensitive to the specific value of the relaxation rates.[11,28] In this regime, the problem of extracting relative population distributions essentially reduces to knowing the absorption coefficients. This aspect is discussed in detail in Chapter 4.

V. CONCLUSIONS

In the present chapter we derived expressions via time-independent diagrammatic perturbation theory that account for the DFWM polarization, collisional, and velocity effects in the weak-field limit (no saturation). In our treatment, we assumed that the DFWM process couples levels of sharp (definite) angular momentum **J**. Three input fields

of arbitrary polarization interact with an isotropic sample to produce a fourth field. The general result (Sec. III) was specialized to apply to circularly and linearly polarized fields that interact in nearly collinear phase matching geometries in collisional environments where the multipole moments of the total angular momentum distribution relax independently (isotropic relaxation) and at the same rate. These specialized expressions (Sec. II) generally apply to DFWM experiments performed in collisionally dominated environments.

In Sec. II we showed that the DFWM signal intensity for collisionally dominated systems is proportional to the square of the concentration difference of the levels involved in the one-photon resonant transition, the fourth power of the one-photon transition strength, the square of a total line shape function, and the square of the total geometric factor. The total geometric factor was shown to depend not only on the polarization of the input fields but also on the specifics of the experiment, i.e., collisional relaxation, velocity, and phase matching. This interdependence complicated the interpretation of the DFWM polarization response but also enabled qualitative information about the collisional relaxation caused by the environment to be obtained from polarization measurements.

Finally in Sec. III, we showed that in the most general case the DFWM signal may be regarded as arising from the contributions of twelve different gratings. These gratings are distinguished by spacing (Δk_{12} or Δk_{32}), by the level in which the grating is formed (ground or excited), and by the multipole nature of the grating (population, orientation, or alignment). Therefore simple population vs. coherence grating pictures of DFWM are not adequate descriptions. For instance, DFWM experiments in which all fields are the same polarization (either linear or circular) have contributions (in addition to population) from higher-order moments of the total angular momentum distribution, namely, alignment for linear, and orientation and alignment for circular. We also showed that the relative multipole moment contributions depend strongly on J for low J values but rapidly approach a high-J limit. In this limit the J dependence of the DFWM signal intensity for a given branch (P, Q, or R) taken with a single polarization configuration primarily reflects the J dependence of the one-photon absorption coefficient B_{ge} as well as any J-dependent relaxation effects.

We have discussed the key aspects of DFWM in reference to molecular species in collisionally dominated environments. We presented explicit expressions for the DFWM signal intensity that can be used with molecular absorption and relaxation data to obtain

83

the relative population distributions. Absorption data in the form of cross sections, line strengths, emission coefficients, etc., are available for most molecules of interest. However obtaining an accurate and complete set of relaxation rates for a given molecule in a specific environment is a formidable task.

References

(1)   D. A. Case, G. M. McClelland and D. R. Herschbach, *Mol. Phys.* **35**, 541 (1978).

(2)   C. H. Greene and R. N. Zare, *J. Chem. Phys.* **78**, 6741 (1983).

(3)   R. N. Zare, *Angular Momentum* (John Wiley & Sons, New York, 1988).

(4)   D. R. Crosley, *Opt. Eng.* **20**, 511 (1981).

(5)   A. C. Eckbreth, *Laser Diagnostics for Combustion Temperature and Species* (Abacus, Cambridge, MA, 1988).

(6)   K. J. Rensberger, J. B. Jeffries, R. A. Copeland, K. Kohse-Höinghaus, M. L. Wise and D. R. Crosley, *Appl. Opt.* **28**, 3556 (1989).

(7)   R. P. Lucht and N. M. Laurendeau, *Appl. Opt.* **18**, 856 (1979). R. P. Lucht, D. W. Sweeney and N. M. Laurendeau, *Appl. Opt.* **19**, 3295 (1980).

(8)   R. Altkorn and R. N. Zare, *Ann. Rev. Phys. Chem.* **35**, 265 (1984).

(9)   N. Billy, B. Girard, G. Gouedard and J. Vigué, *Mol. Phys.* **61**, 65 (1987).

(10)   R. L. Abrams, J. F. Lam, R. C. Lind, D. G. Steel and P. F. Liao, in *Optical Phase Conjugation*, edited by R. A. Fisher (Academic Press, New York, 1983), Chapter 8.

(11)   R. L. Farrow and D. J. Rakestraw, *Science* **257**, 1894 (1992).

(12)   R. L. Abrams and R. C. Lind, *Opt. Lett.* **2**, 94 (1978); erratum **3**, 205 (1978).

(13)   R. L. Farrow, D. J. Rakestraw and T. Dreier, *J. Opt. Soc. Am. B* **9**, 1770 (1992). T. Dreier and D. J. Rakestraw, *Appl. Phys. B* **50**, 479 (1990). T. Dreier and D. J. Rakestraw, *Opt. Lett.* **15**, 72 (1990).

(14)   M. Winter and P. P. Radi, *Opt. Lett.* **17**, 320 (1992).

(15)   B. Yip, P. M. Danehy and R. K. Hanson, *Opt. Lett.* **17**, 751 (1992).

(16)   S. Williams, D. S. Green, S. Sethuraman and R. N. Zare, *J. Amer. Chem. Soc.* **114**, 9122 (1992). T. G. Owano, C. H. Kruger, D. S. Green, S. Williams and R. N. Zare, *Diamond and Related Materials* **2**, 661 (1993). D. S. Green, T. G. Owano, S. Williams, D. G. Goodwin, R. N. Zare and C. H. Kruger, *Science* **259**, 1726 (1993).

(17)   Chapter 4.

(18)   D. R. Meacher, A. Charlton, P. Ewart, J. Cooper and G. Alber, *Phys. Rev. A* **42**, 3018 (1990). J. Cooper, A. Charlton, D. R. Meacher, P. Ewart and G. Alber, *Phys. Rev. A* **40**, 5705 (1989). G. Alber, J. Cooper and P. Ewart, *Phys. Rev. A* **31**, 2344 (1985).

(19)   D. Bloch and M. Ducloy, *J. Opt. Soc. Am.* **73**, 635 (1983); erratum **73**, 1844 (1983).

(20)   G. G. Adonts and D. G. Akopyan, *J. Phys. B: At. Mol. Phys.* **18**, 3407 (1985).

(21)   M. Ducloy, F. A. M. de Oliveira and D. Bloch, *Phys. Rev. A* **32**, 1614 (1985).

(22)   S. Le Boiteux, P. Simoneau, D. Bloch, F. A. M. de Oliveira and M. Ducloy, *IEEE J. Quantum Electron.* **QE-22**, 1229 (1986).

(23)   G. P. Agrawal, *Opt. Lett.* **8**, 359 (1983).

(24)   G. Grynberg, M. Pinard and P. Verkerk, *Opt. Commun.* **50**, 261 (1984).

(25)   M. Pinard, B. Kleinmann and G. Grynberg, *Opt. Commun.* **51**, 281 (1984).

(26)   G. Grynberg, M. Pinard and P. Verkerk, *J. Phys. (Paris)* **47**, 617 (1986).

(27)   P. Verkerk, M. Pinard and G. Grynberg, *Phys. Rev. A.* **35**, (1987).

(28)   R. P. Lucht, R. L. Farrow and D. J. Rakestraw, *J. Opt. Soc. Am. B* **10**, 1508 (1993).

(29)   J. F. Lam and R. L. Abrams, *Phys. Rev. A* **26**, 1539 (1982).

(30)   M. Ducloy and D. Bloch, *Phys. Rev. A* **30**, 3107 (1984).

(31)   P. R. Berman, D. G. Steel, G. Khitrova and J. Liu, *Phys. Rev. A* **38**, 252 (1988).

(32)   F. Aguillion, *IEEE J. Quantum Electron.* **25**, 1947 (1989).

(33)   B. Attal-Trétout, P. Monot and K. Müller-Dethlefs, *Mol. Phys.* **73**, 1257 (1991). B. Attal-Trétout and K. Müller-Dethlefs, *Ber. Bunsenges. Phys. Chem.* **89**, 318 (1985).

(34)   A. A. Panteleev, *Sov. Phys. JETP* **72**, 939 (1991).

(35)   A. I. Alekseev, *Sov. Phys. JETP* **74**, 227 (1992).

(36)   I. Aben, W. Ubachs, G. van der Zwan and W. Hogervorst, *Chem. Phys.* **169**, 113 (1993).

(37)   H. Bervas, S. Le Boiteux, L. Labrunie and B. Attal-Trétout, *Mol. Phys.* **79**, 911 (1993).

(38)   D. Kupiszewska and B. J. Whitaker, *JCS Faraday Trans.* **89**, 2951 (1993).

(39)   E. Freidman-Hill, L. A. Rahn and R. L. Farrow, accepted *J. Chem. Phys.*

(40)   S. A. J. Druet and J.-P. E. Taran, *Prog. Quantum Electron.* **7**, 1 (1981).

(41)   Y. Prior, *IEEE J. Quantum Electron.* **QE-20**, 37 (1984).

(42)   R. C. Hilborn, *Am. J. Phys.* **50**, 982 (1982).

(43)   M. Ducloy and D. Bloch, *J. Phys. (Paris)* **42**, 711 (1981).

(44)   H. J. Eichler, P. Günter and D. W. Pohl, *Laser-Induced Dynamic Gratings* (Springer-Verlag, Berlin, 1986).

(45)   In laser-induced grating phenomena molecular diffusion will fill the grating nulls and will deplete the peaks, i.e., wash out. In general the entire molecular velocity distribution along the grating k-vector contributes. This effect is discussed in T. S. Rose, W. L. Wilson, G. Wäckerle and M. D. Fayer, *J. Chem. Phys.* **86**, 5370 (1987). In DFWM, however, the counterpropagating pump fields insure that only the sub-Doppler projection of the molecular velocity distribution on the grating k-vector contributes.

Because both the grating spacing and the velocity projection increase as $1/\sin(\theta/2)$, the large- and small-spaced gratings wash out to the same degree in the infinite Doppler limit. If the Doppler width is finite, however, the projection along the large-spaced grating's k-vector is finite, and it will be washed out to a lesser degree.

(46)   L. A. Rahn and M. S. Brown, submitted to *Opt. Lett.*

(47)   J. W. Tester, H. R. Holgate, F. J. Armellini, P. A. Webley, W. R. Killilea, G. T. Hong and H. E. Barner, in *Emerging Technologies in Hazardous Waste Management III*, edited by D. W. Tedder and F. G. Pohland (American Chemical Society, Washington D. C., 1993), pp. 518.

(48)   S. M. Wandzura, *Opt. Lett.* **4**, 208 (1979).

(49)   R. L. Farrow, P. H. Paul, E. J. Friedman-Hill and P. M. Danahy, acceted *Opt. Lett.*.

(50)   S. Williams, L. Rahn, P. H. Paul, and J. Forsman, *Thermal Gratings in Flames,* in preparation.

(51)   D. E. Govoni, J. A. Booze, A. Sinha and F. F. Crim, *Chem. Phys. Lett.*, in press.

(52)   J. T. Fourkas, R. Trebino and M. D. Fayer, *J. Chem. Phys.* **97**, 69 (1992).

(53)   J. T. Fourkas, R. Trebino and M. D. Fayer, *J. Chem. Phys.* **97**, 78 (1992).

(54)   J. Nunes, W. G. Tong, L. A. Rahn and D. W. Chandler, in preparation.

(55)   U. Fano and J. H. Macek, *Rev. Mod. Phys.* **45**, 553 (1973).

(56)   A. Omont, *Prog. Quantum Electron.* **5**, 69 (1977).

(57)   K. Blum, *Density Matrix Theory and Applications* (Plenum Press, New York, 1981).

(58)   T. K. Yee and T. K. Gustafson, *Phys. Rev. A* **18**, 1597 (1978).

(59)   R. Trebino, *Phys. Rev. A* **38**, 2921 (1988).

(60)   U. Fano and G. Racah, *Irreducible Tensorial Sets* (Academic Press Inc., New York, 1959).

(61)   B. R. Judd, *Angular Momentum Theory for Diatomic Molecules* (Academic Press, New York, 1975).

(62)   P. N. Butcher and D. Cotter, *The Elements of Nonlinear Optics* (Cambridge University Press, Cambridge, 1990). We use the numerical definitions and convention established by these authors; however, our analysis uses double-sided Feynman diagrams whereas these authors use single-sided diagrams which can lead to errors.

(63)   A good discussion of isotropic relaxation and broadening of optical transitons is given in reference 56, pp. 108-113.

(64)   Because $\mathcal{E}_4 = (ik_4 L/2\varepsilon_o)\wp_4^{(3)}$ there is an additional L^2 dependence where L is the interaction length of the fields in the medium. See reference 30, Eq. (23) and reference 62, pp. 217-218.

(65)   S. Williams, R. N. Zare and L. A. Rahn, *Observation of Orientation and Alignment Dephasing in Resonant Four-Wave Mixing,* in preparation.

(66) E. Hecht, *Optics* (Addison-Wesley Publishing, Inc., Reading, MA, 1987), pp. 270-273.

CHAPTER 4

Effects of Field Polarization in the Reduction of DFWM Spectra to Relative Populations in the Presence of Weak and Strong Fields

There are no *absolutes* in combustion just a lot of *pretty sures*.

Personal Opinion

I. INTRODUCTION

Abrams and Lind (AL)[1] have presented a model of degenerate four-wave mixing (DFWM) which has shown good agreement with experiments.[2-4] The AL model considers a nondegenerate two-level homogeneously broadened system in the presence of two counterpropagating pump fields of arbitrary intensity and weak probe and signal fields. The probe and signal intensities are weak in the sense that they do not significantly affect the level populations. In this model all fields are monochromatic, are of the same polarization state, and are configured in the phase-conjugate geometry (PC-DFWM) discussed in Chapter 3.[5]

One of the most significant predictions of the AL model is that the DFWM signal becomes relatively insensitive to collisions when the intensity of the pump fields is increased so that the population difference of the two-level system oscillates with a rate (Rabi frequency) greater than the relaxation and dephasing rates. When the pump field intensity approaches this value (I_{sat}^o) the DFWM signal is said to be saturated. The collisional independence of saturated DFWM has been verified experimentally for many species including NO,[6,7] OH,[8-10] NH,[11] and CH.[12] Note however that the AL model should be viewed only as a qualitative description of these experiments because in most cases the lasers employed are not monochromatic, the molecules are moving, and the probe field intensity is a significant fraction of the pump field intensity. In addition, molecules possess polarization-dependent spectroscopic properties such as those discussed in Chapter 3 that are not described by the AL model.

Meacher, Charlton, Ewart, Cooper, and Alber (MCECA)[13-15] have developed a theory for DFWM with broad-bandwidth lasers that has shown qualitative agreement with experiments.[13] The MCECA model is similar to the AL model in that intense pump fields and a weak probe field interact with stationary nondegenerate two-level absorbers in a PC-DFWM phase matching geometry; however, the pump bandwidths are assumed to be much larger than the homogeneous line width (including power broadening) of the optical transition. In this model the probe bandwidth can be any size. The results show that increasing the pump bandwidth leads to an increased I_{sat}^o and a slightly different DFWM power dependence compared to the AL model.

Lucht, Farrow, and Rakestraw (LFR)[16] have addressed the effects of molecular motion and strong (saturating) probe field intensity. LFR numerically evaluated the time- and space-dependent density matrix equations directly for a nondegenerate two-level system with molecular motion in which any or all of the incident fields can be saturating.

90

LFR calculated DFWM intensities and line shapes for conditions of interest for flame and plasma diagnostics, and compared the results of their calculations to experimental results of NO in 100 Torr of helium excited by a narrow-bandwidth (0.004 cm^{-1}) laser. Some of the findings of LFR relevant to our work are as follows: first the presence of molecular motion slightly increases I_{sat}^o; second, when the probe field intensity is one quarter of the pump field intensity the DFWM saturation behavior is very similar to the case where the probe field is held constant at a value much less than I_{sat}^o; and third, the DFWM signal is nearly independent of collisions when the pump field intensity is approximately $2I_{sat}^o$.

LFR discussed their work in the context of previous saturation treatments[17-24] so further comparisons will not be made here. The work of AL, MCECA, and LFR greatly enhance the understanding of DFWM saturation; however, because these models assume a nondegenerate two-level system, the effect of polarization in saturated DFWM remains unresolved.

Our aim is to determine the effect of polarization in applying nondegenerate two-level models to experiments involving molecules; in particular we wish to determine how polarization affects extracting relative internal-state distributions from DFWM signals. Our approach is to measure DFWM signals as a function field polarization and intensity and to interpret these data in the framework of the AL and MCECA models using the ideas developed in Chapter 3. In Sec. II we discuss the pertinent experimental details. A brief discussion of the AL and MCECA models is given in Sec. III with an emphasis on the key elements required to interpret DFWM signals. In Sec. IV we present DFWM data of the CH radical in an atmospheric-pressure flame as a function of field polarization and intensity, interpret the results, and present methods for extracting relative population distributions from saturated DFWM signals. In Sec. V we present conclusions of our findings.

II. EXPERIMENTAL DETAILS

A. Experimental Apparatus

Figure 1 shows the experimental configuration in which three fields of the same frequency overlap in the reaction zone of an atmospheric-pressure oxyacetylene flame to generate a fourth field (the DFWM signal). The two coaxial and counterpropagating pump fields, denoted E_1 (forward pump) and E_3 (backward pump), are crossed at a small angle, $\theta = 2°$, by a probe field, E_2. This configuration is commonly referred to as the

FIG. 4.1. Experimental configuration for the measurement of DFWM signals. Spectra are recorded with unfocused beams (diameter ~ 0.5 mm) having energies of 16 μJ for the pump beams (1 and 3) and 4 μJ for the probe beam (2). The flame consists of a standard welding torch fitted with a 0.94 mm nozzle. The abbreviations used in the figure are defined as follows: M: mirror, P: polarizer, L: lens, PH: pinhole, PEM: photoelastic modulator, BS: beamsplitter, WP: half-wave plate, DFR: double Fresnel rhomb, EM: energy meter, PMT: photomultiplier tube.
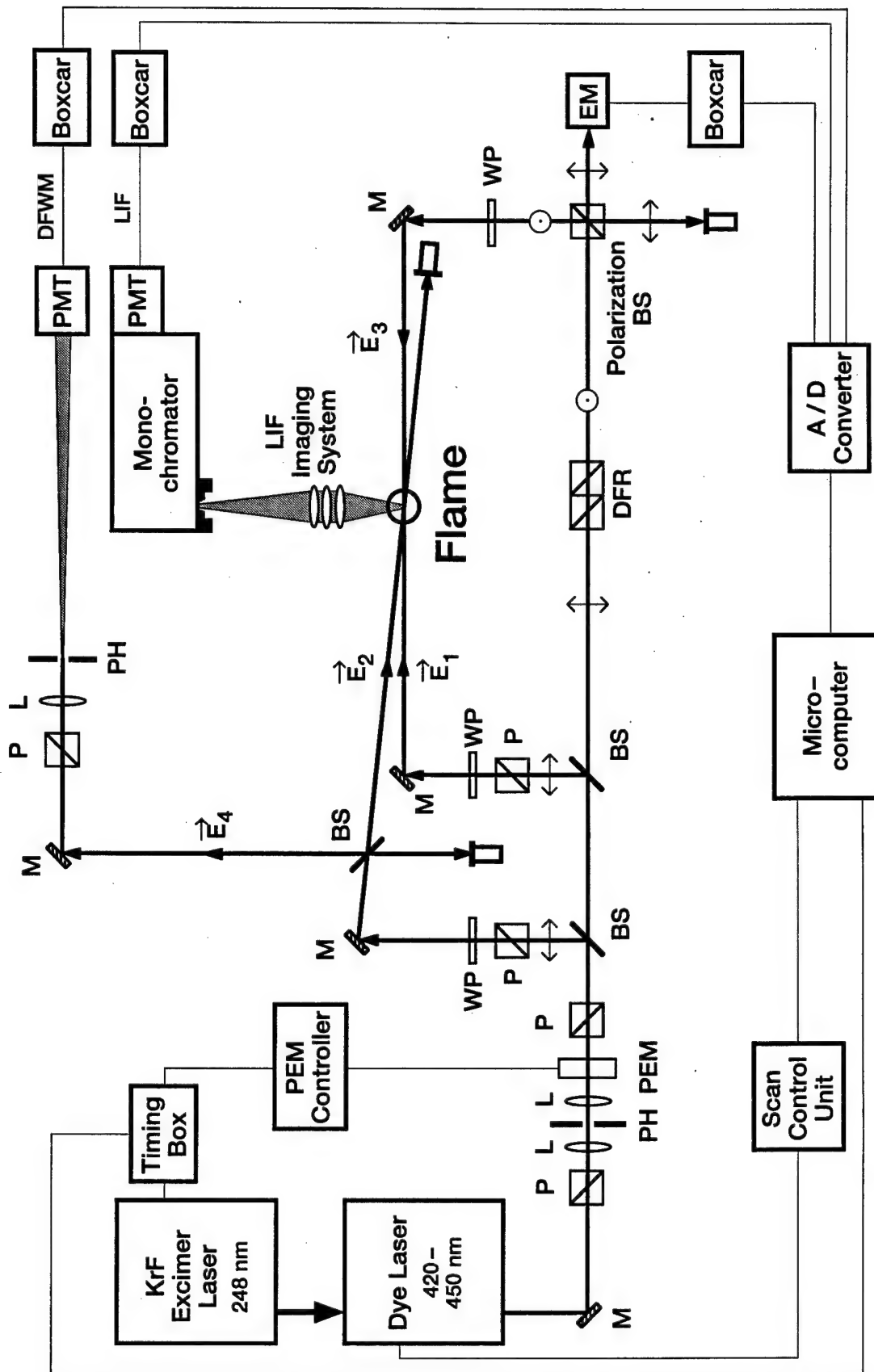
phase-conjugate geometry (PC-DFWM). The PC-DFWM signal field, E_4, is coherently generated and propagates 6 m to a photomultiplier (Hamamatsu R2393P) where it is detected.

Excitation is provided by a KrF excimer-pumped dye laser system (Lambda Physik EMG 102 MSC and FL 2002) operated over the wavelength range of 425-450 nm with a bandwidth of $\Delta\overline{\upsilon}_L$=0.18 ± 0.02 cm^{-1} (fwhm) and a pulse width of $\Delta\tau_L$=16.3 ± 1 ns (fwhm). The output beam of the dye laser is spatially filtered to produce a Gaussian beam profile. The fwhm diameter of the beams is measured using the procedure outlined in reference 25 and is typically d_{fwhm} ~ 0.5 mm. The beam diameter can be determined to ± 0.02 mm . The laser energy is computer (PC/XT) controlled using a photoelastic modulator (Hinds International PEM-CF4) between two crossed polarizers that allows the laser energy to be adjusted between 1 and 800 µJ with no beam deviation. The energy of the probe beam is one quarter of the forward pump beam, and the energy of the backward pump beam is adjusted to the value of the forward pump beam using a double Fresnel rhomb and a polarization beamsplitter which reflects S-polarized and transmits P-polarized light. We measure the beam energy by placing an energy meter (Molectron J4-09) after the polarization beamsplitter which allows the energy to be measured directly and accurately to a fraction of a microjoule.

The DFWM signal is amplified (Lecroy VV100BTB) before being processed by boxcar a averager (SRS SR250). The laser energy is processed directly by a boxcar averager (SRS SR250). Up to four channels are read at each wavelength, digitized, and averaged over 30 laser shots. The data is then stored on a computer (PC/XT) for further analysis. If not otherwise stated, the reported errors include statistical and experimental uncertainties and represent 1σ deviation.

B. Flame

The atmospheric-pressure oxyacetylene flame consists of a standard welding torch fitted with a 0.94 mm diameter nozzle operated in the open air. The flows of acetylene and oxygen are maintained with mass flow controllers (MKS) at 380 cc/min and 360 cc/min, respectively. This results in an oxygen to acetylene volumetric flow ratio, O_2/C_2H_2, of 0.947 and an equivalence ratio, Φ, of 2.64 (fuel rich). The temperature is 2774 ± 140 K at 0.4 mm above the burner nozzle and the CH concentration is estimated to be 30 ppm.[12] At these concentrations (~8 x 10^{11} molecules/cm^3 per quantum state) no CH absorption (< 1%) is observed.

94

C. CH Spectral Features and Collisional Rates

Figure 2 shows a DFWM spectrum of the CH radical taken at 0.4 mm above the burner nozzle. The integrated signal intensities of the well-resolved (0,0) band transitions of the $A^2\Delta$-$X^2\Pi$ system[26] are used in our analysis. The A-X system is highly diagonal,[27-29] and both the X and A states rapidly approach Hund's case (b) coupling as rotation increases. The radiative lifetimes of the v'=0 level of the $A^2\Delta$ state are nearly independent of rotational level.[30,31] In recent calculations, however, Luque and Crosley[29] show that there is about a 4% variation in the radiative lifetimes for N' quantum numbers ranging from N'=2 to N'=20. Therefore we use the calculations of Luque and Crosley and the rotational line strengths of Kovács[32,33] to calculate the Einstein absorption coefficients used in our analysis.[34] Experimental term energies[35] are used for J'' quantum number values up to 12.5. Term energies for higher J'' values are calculated using the spectroscopic constants of reference 35.

High-temperature collisional data for the $A^2\Delta(v'$=0) state of the CH radical are shown in Table 4.1.[36-41] In Table 4.1, R refers to rotational energy transfer and Q refers to quenching. Electronic and vibrational energy transfer are not included because these rates are negligible compared to R and Q.[37] When only cross sections are reported, those of CO and H_2 are used to calculate the rate coefficient. These two molecules are considered because Matsui, Yuuki, and Sahara[42] have determined by mass-spectrometric analysis that the reaction zone of oxyacetylene torch burners consists primarily of CO and H_2. The total collisional transfer rate coefficient T_{ij} (s^{-1}) from energy level i to energy level j of species p due to collisions with several species labeled q is given by

$$T_{ij} = \sum_q N_q \bar{v}_{pq} \sigma_{ij}^{pq} \tag{1}$$

where N_q is the number density (molecules/cm^3) of species q, σ_{ij}^{pq} is the cross-section (cm^2), and $\bar{v}_{pq}$ is the average relative speed (cm/s) of species p and q. The average relative speed is given by

$$\bar{v}_{pq} = \left(\frac{8k_B T}{\pi \mu_{pq}}\right)^{\frac{1}{2}} \tag{2}$$

where k_B is the Boltzmann constant, T is the temperature, and μ_{pq} is the reduced mass for species p and q. To our knowledge the highest temperature data available are at 2000 K. The temperatures of interest in our investigations are approximately 2774 K. Therefore the rates are scaled to this temperature by making a $1/T$ density correction and a $T^{1/2}$

95

FIG. 4.2. DFWM spectrum of selected Q- and R-branch transitions of the CH $A^2\Delta$-$X^2\Pi$ (0,0) and (1,1) bands recorded using the YYXX polarization configuration. In the figure only the (0,0) band transitions are labeled. The fine-structure components are indicated on the branch designations by subscript $1 = {}^2\Delta_{5/2}-{}^2\Pi_{3/2}$ and subscript $2 = {}^2\Delta_{3/2}-{}^2\Pi_{1/2}$. The upper state and lower state Λ doublets are labeled by e and f; when they are the same for both levels, ee is abbreviated by e and ff is abreviated by f.

DFWM Relative Intensity (a.u.)

Wavelength (nm)

Q_{1ef} Q_{1fe} Q_{2ef} Q_{2fe}

R_{1e} R_{1f}

R_{2e} R_{2f}
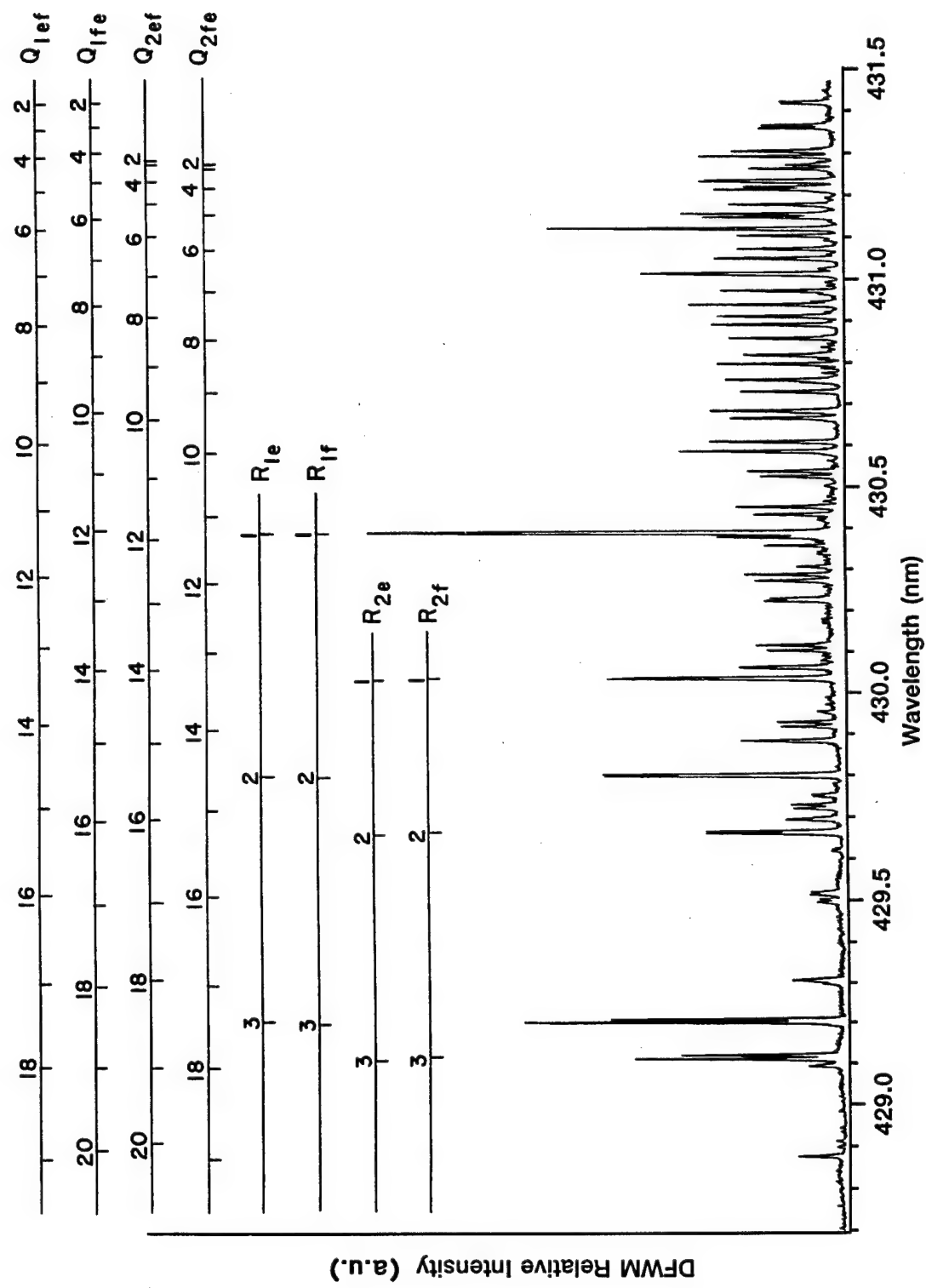
Table 4.1. CH energy transfer rates.

Ref.	CH Source	Temperature	N'	R/Q	Q^a
37	Flame	2040 K	6, 14	$2.4 \pm 0.1, 4.1 \pm 0.4$	---
36	Flame	2000 K	11	4^b	5.1 ± 0.4
38	Pyrolysis	1300 K	average	---	5.6 ± 0.4
39	Flame	1600 K	6	3.6 ± 0.5	3.6 ± 2.4
39	Flame	1600 K	3, 12	$2.7 \pm 0.5, 3.8 \pm 0.5$	---
40	Flame	1800 K	average	---	4.7 ± 0.3
41	Flame	1700 K	average	---	1.8 ± 0.4^c

[a]Estimated for CH at 2774 K in units of 10^8 s^{-1}. [b]Error not reported. [c]Estimated error.

velocity correction. Such a method is accurate if the cross-sections do not change significantly with velocity. Strictly speaking, the T_{ij} (s^{-1}) have units of a first-order chemical kinetic rate coefficient; however, they are more commonly referred to as rates in nonlinear optics. Therefore in what follows we will refer to the collisional transfer rate coefficients T_{ij} as rates.

D. Saturation Measurements

In Chapter 1 saturation measurements were performed by obtaining spectral scans at specific laser intensities. The line-center signal intensities (peak heights) were easily distinguished from the baseline noise. Because of the time required to take a spectral scan at each laser intensity the data accumulation time was quite long (~2 hours). We observe for our present experimental conditions that the major source of noise is scattered light. We are not able to observe a coherent nonresonant background signal in these experiments. Furthermore, the scattered light results primarily from beam 2 (probe) because it scatters light directly along the detection axis. A lesser contribution from beam 3 (backward pump) is also observed due to distortion and refraction of the beam after passing through the flame. Scattered light from beam 1 (forward pump) is found to be on the order of the electronic noise of the detection system, which is much less than the noise from the scattered light of beams 2 and 3.

In the present chapter we vary the laser energy with the laser frequency held at line center. Specifically, the KrF excimer laser trigger is phase locked with the 50 kHz oscillations of the photoelastic modulation crystal. Varying the laser trigger delay varies the retardation of the light exiting the crystal, and hence, the amount of light that passes through the second polarizer. The laser energy is varied under computer control, and the total light intensity reaching the detector and laser energy are recorded each laser shot. Then in a separate scan the forward pump beam is blocked, and a scattered light signal is obtained as a function of laser energy. Both traces are sorted as a function of laser energy (corrects for shot-to-shot fluctuations) and binned at intervals of 0.5 μJ. The upper and lower solid symbol traces in Fig. 3 are examples of the total signal and scattered light signal, respectively. The scattered light signal (linear in laser energy) is subtracted from the total signal to obtain the DFWM signal as a function of laser energy (open symbols in Fig. 3). This method allows an entire saturation curve to be obtained in approximately five minutes with each data point consisting of an average of 60-90 laser shots.

FIG. 4.3. Line-center saturation curve for the YYXX linear polarization configuration of the $Q_{1ef}(8)$ transition as a function of saturation intensity (bottom), and pump field spectral intensity (top). The upper and lower solid symbol traces in the figure are the total signal (-■-) and scattered light (-▲-) signal, respectively. The scattered light signal (linear in laser intensity) is subtracted from the total signal to obtain the DFWM signal as a function of laser intensity (-O-).
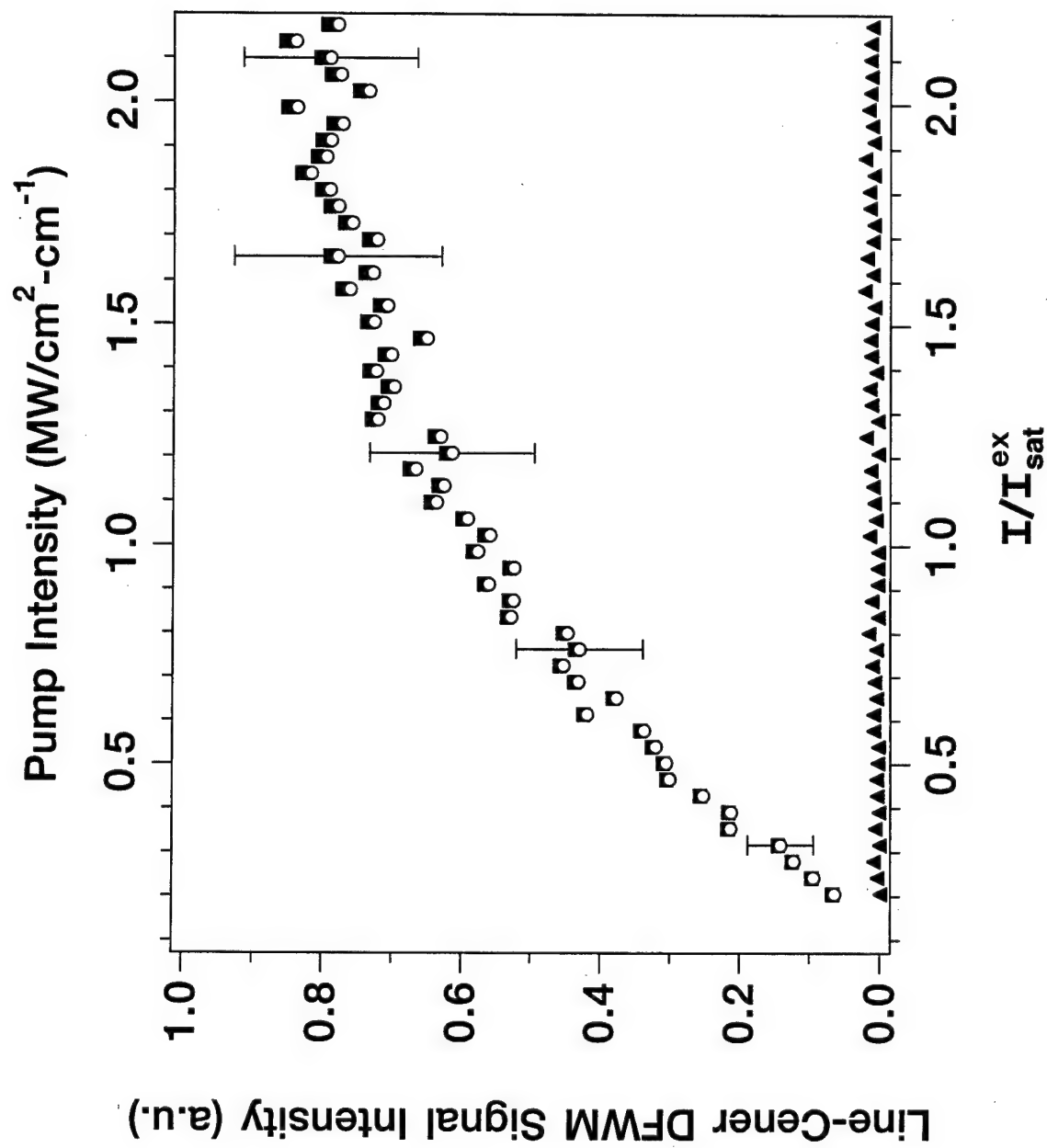
In calculating the laser spectral intensity from the measured beam energies, we use $\Delta\bar{\upsilon}_L$=0.18 $\pm$ 0.02 cm^{-1}, $\Delta\tau_L$=16.3 $\pm$ 1 ns, and $A = \pi(d_{TH}/2)^2$ where d_{TH} is the "top hat" diameter of a Gaussian beam[43] (d_{TH} equals 1.2 d_{fwhm} and typically d_{fwhm} = 0.5 mm). For example, typical beam energies employed in these experiments are 16 μJ for the forward and backward pump beams and 4 μJ for the probe beam. These values correspond to 1.93 MW/cm^2-cm^{-1} and 0.48 MW/cm^2-cm^{-1}, respectively. In what follows I^o_{sat} is the theoretical line-center saturation intensity, I^{ex}_{sat} is the experimental line-center saturation intensity, and $< I^{ex}_{sat} >$ is the average experimental line-center saturation intensity for different polarization configurations of single transition.

E. Polarization Measurements

The experiment is configured so that any linear polarization configuration is obtained by rotating the half-wave plates shown in Fig. 1. After polarization rotation each pump beam is directed by one additional mirror. Differences in S and P reflectance for all the mirrors is approximately 3%. The beamsplitter in the probe axis, which is used to collect the DFWM signal, reflects P-polarized light at 66.4 $\pm$ 6% times the efficiency for S-polarized light. The probe mirror, however, reflects P-polarized light at a higher efficiency than S-polarized light which results in less than 5% difference in the probe field intensity at the flame as its polarization is rotated. The polarization purity of all of the electric fields is greater than 98%.

Shot-to-shot polarization measurements are performed by placing the photoelastic modulator in place of one of the half-wave plates and removing the polarizer from the detection axis. The laser delay relative to the photoelastic modulator is adjusted on a shot-to-shot basis so that every other shot corresponds to either 0° or 180° retardation (half-wave plate). The DFWM signal and laser energy are averaged over 30 laser shots for each polarization configuration and for each spectral position. The shot-to-shot measurements enable polarization ratios to be obtained in real-time at a single laser intensity. These measurements are used to check the accuracy of polarization measurements taken a few minutes apart.

In what follows Y represents the linear polarization state that corresponds to S-polarized light, i.e., light polarized perpendicular to the plane of the laser table, and X represents P-polarized light. In addition we use the notation established in Chapter 3 where a polarization configuration is given as $\varepsilon_4\varepsilon_1\varepsilon_3\varepsilon_2$ where ε_j is the polarization vector

of the electric field labeled j. For example the YYXX polarization configuration corresponds to E_4 and E_1 being Y polarized and E_3 and E_2 being X polarized.

F. Rotational Temperature Measurements

In our rotational temperature analysis resolved Q_1 and Q_2 transitions of the $A^2\Delta(v'=0)$-$X^2\Pi(v''=0)$ system are used. For CH the Q branch covers a small spectral region and is sufficiently resolved to allow the analysis of individual DFWM transitions. Therefore rotational temperatures are obtained with minimal scan times. The XXXX and YXYX polarization configurations have been used in previous experiments, [3,6-12] but we chose the YYXX configuration because it offers many advantages. First the YYXX polarization configuration greatly discriminates against thermal grating contributions because only small-spaced intensity gratings are present.[5,44] We have not observed any direct evidence to suggest that thermal gratings are produced in this flame; however, this polarization configuration assures that their interference is negligible. Second, as stated in Sec. IIC, the primary source of noise in these experiments is scattered light from the probe beam (~90%) and the backward pump beam (~10%) with a negligible contribution (on the order of the electronic noise) from the forward pump beam. In the YYXX polarization configuration, the signal beam is crossed polarized to both of the "noisy" beams, and therefore the YYXX configuration offers true zero background detection when a linear polarizer is placed in the detection axis. Contrary to first impressions, the PC-DFWM signal intensity using the YYXX polarization configuration is equal to the YXYX configuration. Both these configurations give approximately 1/9 the signal intensity of the XXXX configuration (Table 3.3), but the thermal-grating and scattered-light discrimination make up for the loss of signal.

III. SATURATION MODELS

The AL model considers a nondegenerate two-level homogeneously broadened system in the presence of arbitrary pump field intensities and weak probe and signal intensities. In this model all fields are assumed to be monochromatic. In the limit of weak probe and signal intensities a full solution of the density matrix equation for the interaction of the pump fields with the two-level system is possible. The density matrix solution for two-level nondegenerate saturable absorbers in the presence of arbitrary field intensities is

well known in semi-classical laser theory. An excellent discussion of the topic is given in reference 45.

For electric fields defined as

$$E_j(z,t) = \frac{1}{2} E_j e^{-i(\omega_j t - k_j z)} + c.c. \quad ; \quad E_j = \mathcal{E}_j \varepsilon_j \quad ; \quad I_j = \frac{c\varepsilon_o}{2} |\mathcal{E}_j|^2, \tag{3}$$

where E_j is the vector amplitude, $\mathcal{E}_j$ is the scalar amplitude, ε_j is the normalized $(\varepsilon_j \cdot \varepsilon_j^* = 1)$ polarization unit vector, and I_j is the intensity of the electric field labeled j, the density matrix solution in the rotating-wave approximation for the steady-state population (number density) difference $\Delta N = N_g - N_e$ is

$$\Delta N = \frac{\Delta N_o}{1 + n|\Omega|^2/|\Omega_{sat}|^2} = \frac{\Delta N_o}{1 + n I/I_{sat}^o}, \tag{4a}$$

with

$$n = \frac{4 \cos^2(kz)}{1 + (\Delta/\Gamma_{eg})^2}. \tag{4b}$$

The Rabi frequency $|\Omega_j|$ associated with the field labeled j is defined with respect to the field intensity I_j as

$$|\Omega_j|^2 = \frac{|\mu_{ge}\mathcal{E}_j|^2}{\hbar^2} = \frac{2|\mu_{ge}|^2}{c\varepsilon_o\hbar^2} I_j, \tag{5}$$

and the saturation Rabi frequency $|\Omega_{sat}| = (\Gamma_o \Gamma_{eg})^{1/2}$ is defined with respect to the line-center saturation intensity I_{sat}^o as

$$|\Omega_{sat}|^2 = \frac{2|\mu_{ge}|^2}{c\varepsilon_o\hbar^2} I_{sat}^o. \tag{6}$$

In Eqs. (3)-(6) g refers to the lower level, e refers to the upper level, $\Delta N_o = N_g^o - N_e^o$ is the population difference of the two-level system in the absence of applied fields, $|\mu_{ge}|^2$ is the square of the transition dipole moment connecting levels g and e, $|\Omega|$ is the Rabi frequency associated with the pump fields ($|\Omega| = |\Omega_1| = |\Omega_3|$), I is the intensity of the pump fields ($I = I_1 = I_3$), k is the magnitude of the propagation vector of the fields, $\Delta = \omega - \omega_o$ is the spectral shift from the resonance frequency ω_o, and Γ_o and Γ_{eg} are the population relaxation and coherence dephasing rates, respectively. All of the terms are in SI units, and the constants ε_o, $\hbar$ and c have their usual meanings.

In Eq. (4) we see that the result of the interference of the two counterpropagating pump fields is a sinusoidally varying electric field intensity that spatially "burns holes" into

104

the population difference spaced one-half wavelength apart.[46] The two-level system is said to be saturated when the population difference, $\Delta N = N_g - N_e$, is zero over the entire interaction volume. Inspection of Eqs. (4) and (6) shows that saturation occurs when the optical pumping rate denoted by the Rabi frequency is much faster than the population relaxation and coherence dephasing rates.

Having obtained the system response in the presence of strong pump fields, perturbation theory is used to include the weak probe and signal fields. The final result is an analytic model of the DFWM signal. AL solved the slowly varying envelope approximation (SVEA) equations for the probe and signal fields. In the limit of no absorption, the SVEA equations are

$$\frac{d\mathcal{E}_2}{dz} = 0, \quad \frac{d\mathcal{E}_4}{dz} = i\beta\mathcal{E}_2^*, \tag{7}$$

where β is the nonlinear coupling coefficient defined in reference 2, page 222, Eq. (16). For the case of equal intensity pumps, the expression for the DFWM signal[2,47,48] is given by

$$I_{DFWM} = |\beta|^2 L^2 I_2 = R_{AL} \, I_2 \,, \tag{8}$$

with

$$R_{AL} = 4\,\alpha_o^2 L^2 \left[\frac{I}{I_{sat}^o}\right]^2 \left[\frac{\Gamma_{eg}^2}{\Delta^2 + \Gamma_S^2}\right]^3, \tag{9}$$

$$\alpha_o = \frac{\omega_o \Delta N_o |\mu_{ge}|^2}{2c\varepsilon_o \hbar\Gamma_{eg}}, \tag{10}$$

and

$$\Gamma_S = \Gamma_{eg} \left(1 + 4I / I_{sat}^o\right)^{1/2}. \tag{11}$$

In Eqs (7)-(11) R_{AL} is the AL model reflectivity, α_o is the line-center attenuation coefficient, L is the effective interaction length of the excitation fields, $I = I_1 = I_3$ is the intensity of the pump fields, and I_2 is the intensity of the probe field. Equation (8) defines the cube of a power-broadened Lorentzian with an actual half-width given by $\Gamma_S\left(2^{3/2} - 1\right)^{1/2}$.

The formulation of the MCECA model is similar in concept to the AL model with the exception that the excitation fields are not monochromatic (coherent). The MCECA model considers a medium of two-level nondegenerate absorbers transversed by two broad-bandwidth (incoherent) copolarized pump fields of equal and arbitrary intensity and a weak probe field of any bandwidth. Furthermore MCECA assume that the fields are statistically independent (chaotic) and uncorrelated (delayed with respect to each other by a distance much greater than the coherence length).[49-51] The bandwidths of the pump fields have a Lorentzian spectral shape with a fwhm of $\Delta\omega_1 = \Delta\omega_3 = 2b$. Most importantly, this model assumes that the bandwidths exceed all other rates that determine the time evolution of the system, i.e., $b >> |\Omega|, \Gamma_o, \Gamma_{eg}$. In this case the bandwidth-dependent saturation Rabi frequency is given by $|\Omega_{sat}| = (b\Gamma_o)^{1/2}$, and the average density matrix population terms vary on a time scale of $1/\Gamma_o$ whereas the much shorter correlation time of the fields varies as $1/b$. Under these conditions, all products of field and population terms may be treated as uncorrelated. This aspect is the key element of the treatment.

In contrast to the AL model expression of Eq. (4) which involves coherent fields, the interference of the counterpropagating pump fields considered by MCECA does not produce a steady-state standing wave pattern because the fields are incoherent and uncorrelated. Replacing the $\cos^2(kz)$ term of Eq. (4b) with its average value of 1/2 and assuming that $b >> \Gamma_{eg}$, we obtain the expression for the for the steady-state population difference $\Delta N = N_g - N_e$ of the MCECA model, namely,

$$\Delta N = \frac{\Delta N_o}{1 + m|\Omega|^2 / |\Omega_{sat}|^2} = \frac{\Delta N_o}{1 + m I / I_{sat}^o}, \tag{12a}$$

with

$$m = \frac{2}{1 + (\Delta/b)^2}, \tag{12b}$$

where I_{sat}^o is defined by Eq. (7) with $|\Omega_{sat}|^2 = b\Gamma_o$. We see in Eq. (12) that stronger fields are required to saturate the two-level system when broad-bandwidth lasers are used because the Rabi frequency must now exceed $(b\Gamma_o)^{1/2}$ which is much larger than $(\Gamma_o\Gamma_{12})^{1/2}$.

Analytic expressions[14] for the DFWM signal of the MCECA model are obtained when the bandwidth of the probe field, $\Delta\omega_2 = 2p$, is also large in the sense that $|\Omega|^2 << pb$ and $p >> \Gamma_o, \Gamma_{eg}$. Specifically for $p=b$ and for small detunings compared to the laser bandwidth ($\Delta << b$), we have the simplified MCECA expression for the DFWM signal, namely,

$$I_{DFWM} = R_{MCECA}\, I_2, \tag{13}$$

where

$$R_{MCECA} = \frac{\Gamma_o}{b}\alpha_o^2 L^2 \left[\frac{I}{I_{sat}^o}\right]^2 \left[\frac{\Delta^2 + b^2}{\Delta^2 + \Gamma_{S1}^2}\right]^{1/2} \left[\frac{b^4}{\left(\Delta^2 + \Gamma_{S2}^2\right)\left(\Delta^2 + \Gamma_{S3}^2\right)}\right]^{3/2}, \tag{14}$$

$$\Gamma_{S1} = b\left(1 + r_{pc} I / I_{sat}^o\right)^{1/2}, \tag{15}$$

$$\Gamma_{S2} = b\left(1 + 2I / I_{sat}^o\right)^{1/2}, \tag{16}$$

and

$$\Gamma_{S3} = b\left(1 + (2 + r_{pc})I / I_{sat}^o\right)^{1/2}. \tag{17}$$

In Eqs. (13)-(17) r_{pc} is the ratio of the population relaxation rate to the coherence dephasing rate ($r_{pc} = \Gamma_o / \Gamma_{12}$), and the remaining terms have been defined previously. For $I \leq 3I_{sat}^o$, Eq. (13) approximates a power-broadened Lorentzian-cubed profile like the AL model but with a spectral width determined by the laser bandwidth. For higher laser intensities, the line shape power broadens more rapidly than a Lorentzian-cubed profile and develops a dip at line center. The intensity range over which Eq. (13) applies depends on the laser bandwidth and the population relaxation rate caused by the environment. Because $b >> |\Omega|$ and $|\Omega_{sat}|^2 = b\Gamma_o$, we find that the condition

$$I / I_{sat}^o = |\Omega|^2 / |\Omega_{sat}|^2 << b / \Gamma_o \tag{18}$$

needs to be satisfied for Eq. (13) to be valid.

The collisional relaxation and dephasing rates for our experimental conditions must be determined in order to apply the models discussed in this section. We base the discussion on the available relaxation data for the CH radical (Sec. IIC), but the discussion is also applicable to other flame and plasma species. For molecules in collisionally dominated environments, the rotational levels involved in the one-photon transition are effectively coupled by rotational energy transfer (R) collisions to other rotational levels. Furthermore, the excited rotational levels are coupled to the ground rotational levels by quenching (Q) and spontaneous emission (A_{eg}). For this case the relaxation of the molecular levels approximates a four-level system.[52] For such a system the population relaxation and coherence dephasing rates are defined[45] as

$$\Gamma_o = \frac{2\Gamma_g \Gamma_e}{(\Gamma_g + \Gamma_e)}, \tag{19}$$

and

$$\Gamma_{eg} = \frac{1}{2}(\Gamma_g + \Gamma_e) + \Gamma_{eg}^{pd}, \tag{20}$$

where Γ_g and Γ_e are the population relaxation rates of levels g and e, and Γ_{eg}^{pd} is the pure dephasing rate of the dipolar transition.

In our analysis we take R to be the same for the $A^2\Delta$ ($v'=0$) and $X^2\Pi$ ($v''=0$) levels because the rotational spacings are very similar and define the ground and excited population relaxation rates as $\Gamma_g = R$ and $\Gamma_e = R + Q + A_{eg}$, respectively. With these definitions we estimate an average population relaxation rate of $\Gamma_o = 2 \times 10^9$ s^{-1} using the values of Table 4.1. Assuming that the pure dephasing rate is small compared to R, we have $\Gamma_o \cong \Gamma_{eg}$ ($r_{pc} = 0.98$ for $R/Q = 3.5$). Furthermore because the characteristic collisional relaxation times are ~ 40 times shorter than the laser pulse, i.e., $\Delta\tau_L \gg 1/\Gamma_g \cong 1/\Gamma_e$, steady-state conditions are assumed, and we use the AL and MCECA expressions discussed in this section.[53] In addition we expect the MCECA model to apply for laser intensities up to approximately twice the saturation intensity because $b/\Gamma_o = 9$ in Eq. (18). In Eqs. (8) and (13) ΔN_o is replaced with the ground state population because $N_g^o \gg N_e^o$ for our flame conditions.[12]

IV. RESULTS AND DISCUSSION

A. Polarization Ratios as a Probe of Collisional Dynamics

In Chapter 3 we discussed how DFWM polarization measurements provide information about the collisional relaxation caused by the environment. Line-center saturation curves like those of Fig. 3 for the $R_{1f}(8)$ and $Q_{1ef}(8)$ transitions were obtained for different linear polarization configurations. The line-center saturation curves of the $R_{1f}(8)$ transition are shown in Fig. 4. The absolute signal intensities dramatically differ for the four polarization configurations. To emphasize the differences in signal intensities, polarization ratios as a function of laser intensity are made from the saturation curves. Figure 5 shows polarization ratios of the $R_{1f}(8)$ and $Q_{1ef}(8)$ transitions as a function of pump field intensity. The solid symbols in Fig. 5 are experimental data and dashed lines in Fig. 5 are the predicted polarization ratios using Table 3.3.

Figure 5a shows the XYYX/XXXX polarization ratio of the $R_{1f}(8)$ transition, and Fig. 5b shows the YYXX/YXYX polarization ratio of the $Q_{1ef}(8)$ transition. The predicted polarization ratios in Figs 5a and 5b are in good agreement with the data at

FIG. 4.4. Line-center saturation curves for different linear polarization configurations of the $R_{1f}(8)$ transition as a function of average saturation intensity $< I_{sat}^{ex} >= 1.77$ MW/cm^2-cm^{-1} (bottom), and pump field spectral intensity (top). In the figure -■-, -▲-, -●- and -◆- correspond to the XXXX, YXYX, YYXX and XYYX polarization configurations, respectively. The absolute signal intensities dramatically differ for the four polarization configurations, but the saturation intensities (Table II) obtained from the AL model (dashed curves) and MCECA model (solid curves) are nearly equal for all polarization configurations.
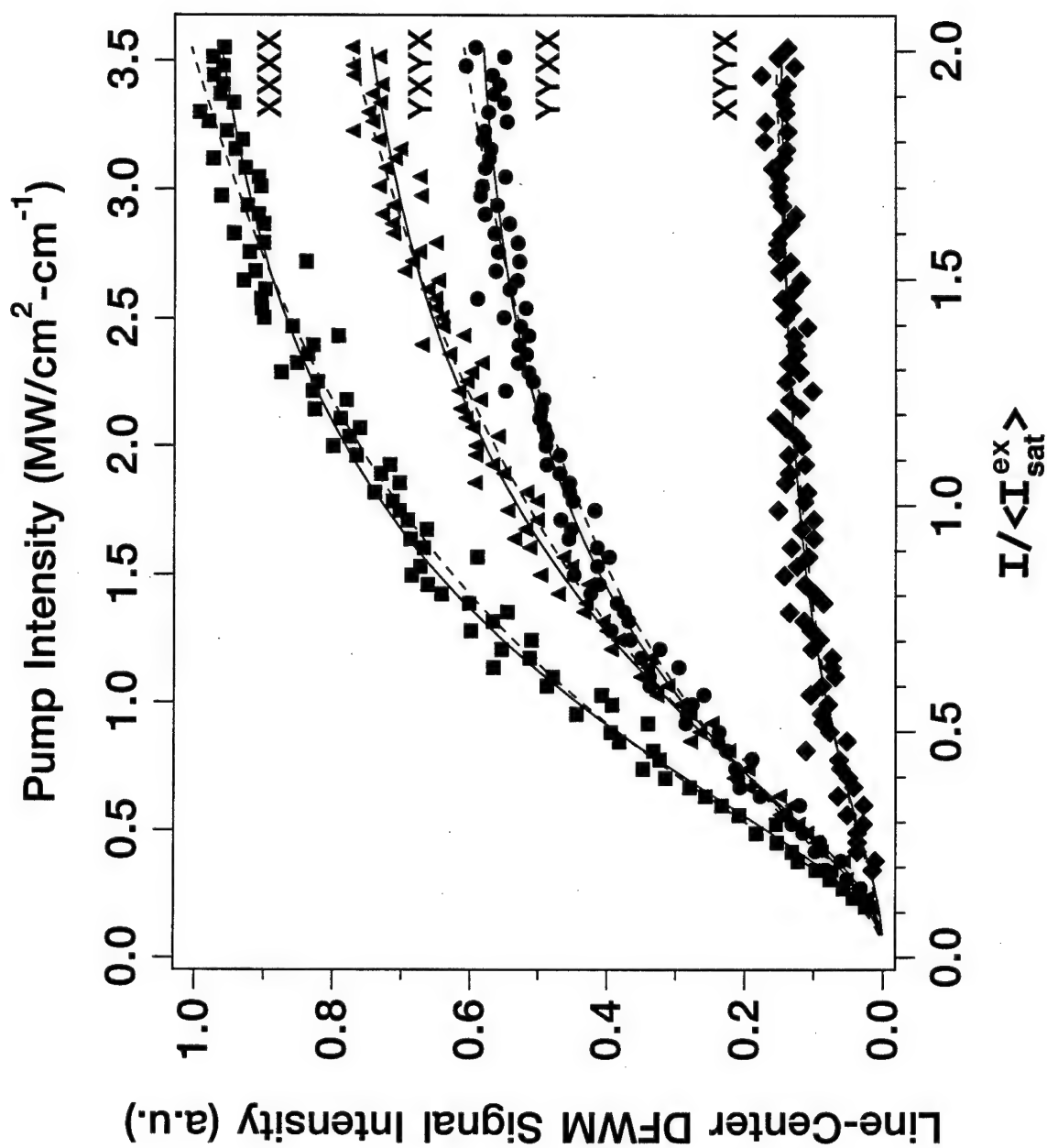
FIG. 4.5. The solid points are the experimental polarization ratios and the dashed lines are the predicted YYXX/YXYX polarization ratios using Table 3.3. (a) XYYX/XXXX polarization ratio for the $R_{1f}(8)$ transition as a function of average saturation intensity $<I_{sat}^{ex}>= 1.77$ MW/cm^2-cm^{-1}. The average value of the data between 0.1 and 0.4 $<I_{sat}^{ex}>$ is 0.20 ± 0.06 which is in good agreement with the calculated value of 0.24. (b) YYXX/YXYX polarization ratio for the $Q_{1ef}(8)$ transition as a function of average saturation intensity $<I_{sat}^{ex}>= 1.10$ MW/cm^2-cm^{-1}. The average value of the data between 0.1 and 0.4 $<I_{sat}^{ex}>$ is 0.92 ± 0.14 which is close to the expected value of 1.0. (c) YYXX/YXYX polarization ratio for the $R_{1f}(8)$ transition as a function of average saturation intensity $<I_{sat}^{ex}>= 1.77$ MW/cm^2-cm^{-1}. The average value of the data between 0.1 and 0.4 $<I_{sat}^{ex}>$ is 1.04 ± 0.09 which is close to the expected value of 1.0.

111
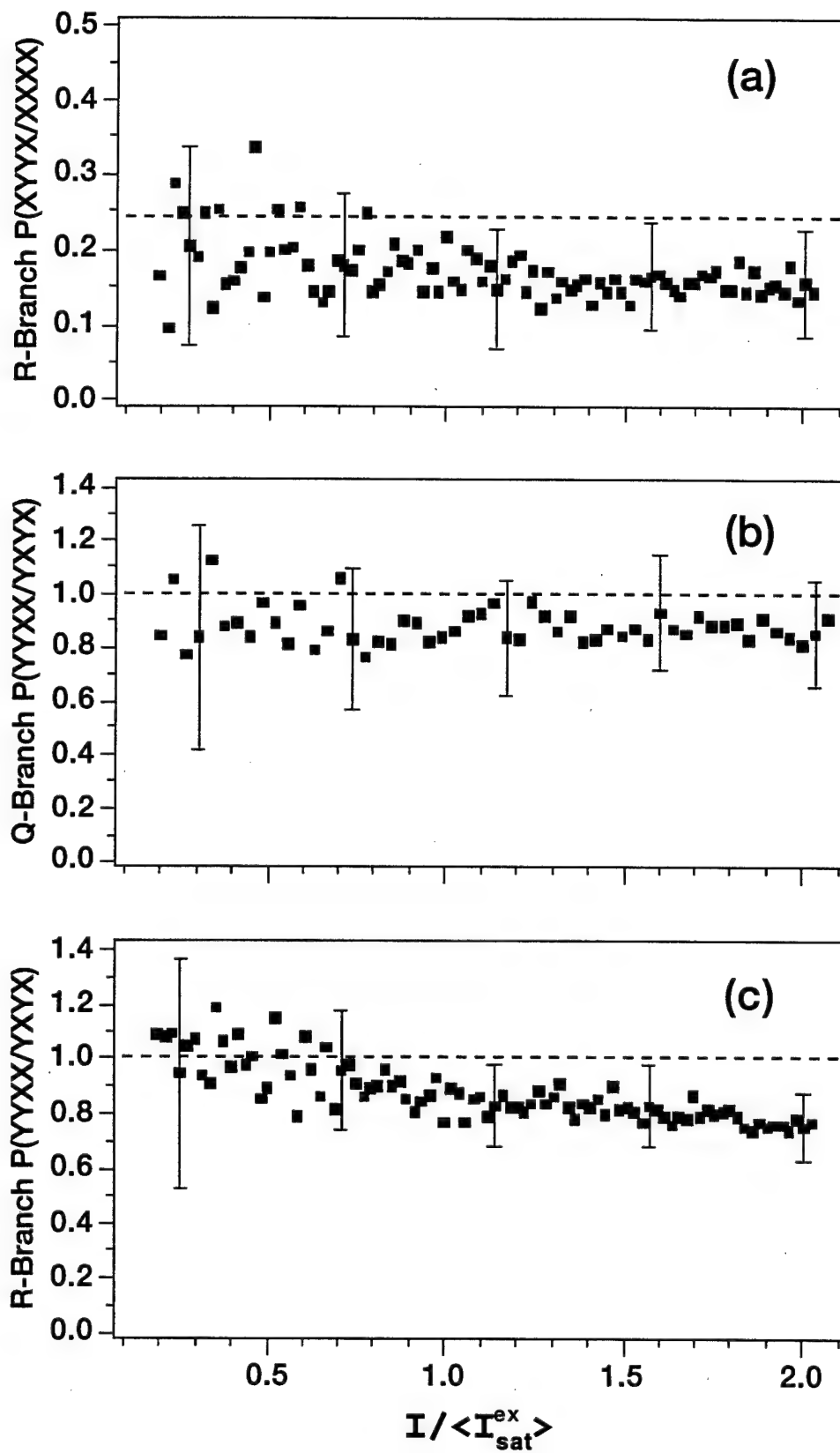
weak pump field intensity. Specifically, the average value of the data between 0.1 and 0.4 $< I_{sat}^{ex} >$ is 0.20 ± 0.06 in Fig 5a and 0.92 ± 0.14 in Fig. 5b. These values are close to the predicted polarization ratios of 0.24 and 1.0, respectively. Recall that the values of Table 3.3 were derived assuming that all of the multipole moments of the total angular momentum distribution, i.e., the population, the orientation, and the alignment, relax at the same rate and that no other process contributes the observed signal.

We have observed Q-branch polarization ratios different from the values of Table 3.3 for the OH radical in the burnt gas region of atmospheric-pressure hydrogen-oxygen flames.[54,55] We have attributed this effect to the presence of thermal gratings. With helium dilution, however, thermal gratings are no longer present, but anomalous polarization ratios are still observed for levels with low J quantum numbers. Nearly degenerate four-wave mixing (NDFWM) scans confirmed that in the helium-diluted flames the rates of relaxation of the multipole moments are not equal.[56] Therefore the good agreement between the data at low intensity in Figs. 5a and 5b with the calculated values implies that the mutipole moments are relaxing equally and that other laser-induced phenomena such as a thermal grating are not present.

In PC-DFWM of Doppler broadened systems, polarization ratios of P- and R-branch transitions are dependent on the relative values of the relaxation rates of ground and excited levels when the pump fields are cross polarized, i.e., when the YYXX and YXYX polarization configurations are used. We estimate a collisional full width, $2\Gamma_{eg}$, of 4×10^9 s^{-1} (0.02 cm^{-1}) and a Doppler width, $\Delta\omega_D$, of 46×10^9 s^{-1} (0.24 cm^{-1}) for CH at 2774 K. Our experiment corresponds to a Doppler-broadened system because $\Delta\omega_D > 2\Gamma_{eg}$. For such a system the YYXX/YXYX polarization ratio of the $R_{1f}(8)$ transition has a value of 1.4 when $\Gamma_e << \Gamma_g$, 0.70 when $\Gamma_e >> \Gamma_g$, and 1.0 when $\Gamma_e = \Gamma_g$.

Figure 5c illustrates the YYXX/YXYX polarization ratio for the $R_{1f}(8)$ transition, and the dashed line of Fig. 5c is the prediction of Table 3.3 which corresponds to $\Gamma_e = \Gamma_g$. The average value of the data between 0.1 and $0.4 < I_{sat}^{ex} >$ is 1.04 ± 0.09 which suggests that the relaxation rates of the ground and excited levels are approximately equal. This conclusion is consistent with the energy transfer data available for the CH radical. The rotational spacings of the v=0 vibrational levels of the X and A states of CH are nearly the same, and the rotational energy transfer rate of the v'=0 level of the A state is approximately 3.5 times faster than quenching. Furthermore if the quenching collisions do not trap population in higher vibrational states (rapid energy transfer to v''=0), we expect that $\Gamma_g \cong \Gamma_e$ according to the four-level model referred to in Sec. III.

An interesting aspect of Fig. 5 is that the experimental polarization ratios are within 30% of the perturbative calculations up to twice the saturation intensity. In the weak-field limit the DFWM signal is dependent on the spatial anisotropy of the total angular momentum distribution induced by the three input fields. Therefore this close agreement implies that the relative anisotropy of the total angular momentum represented by the total geometric factors persists to a large degree as the laser intensity increases. This effect is similar to that expected for saturated laser induced fluorescence measured with different polarization configurations (Fig. 5 of reference 57).

B. Saturation Behavior

The line-center saturation intensities resulting from nonlinear least squares fits of saturation data to the power dependencies of the AL model, Eq. (8) and the MCECA model, Eq. (13) for $\Delta = 0$ and $r_{pc} = 0.98$ are given in Table 4.2. In Table 4.2, the total error increases significantly as the ratio of the DFWM signal to the scattered light intensity decreases. The AL model and the MCECA model exhibit very similar saturation behavior for moderately high laser intensities $(I \sim I_{sat}^o)$. This statement is validated by the fact that the fitted saturation curves (Fig. 4) and saturation intensities (Table 4.2) of the two models are very similar. Therefore it is not surprising that the AL model has been able to qualitatively reproduce the saturation behavior for experiments employing broad-bandwidth (multi-mode) lasers.[12] The error associated with the MCECA saturation intensities, however, is approximately 30% smaller than the error associated with the AL saturation intensities. The reduced error results from the fact that the fits to MCECA model are more sensitive to the value of the saturation intensity (higher order power dependence) and are better correlated with the data.

For a single transition, the fitted MCECA saturation intensities of Table 4.2 are approximately equal regardless of the polarization configuration. For instance, the saturation intensities for the four polarization configurations of the $R_{1f}(8)$ transition are within 30% of the average value $\left\langle I_{sat}^{ex} \right\rangle$ of 1.77 MW/cm^2-cm^{-1}. This similarity is more easily seen in Fig. 6 which shows the DFWM reflectivity at line center for the four polarization configurations of the $R_{1f}(8)$ transition. The MCECA line-center reflectivity is at a maximum at $0.6\ I_{sat}^o$, and in Fig. 6, the reflectivity for each polarization configuration peaks at approximately the same pump field intensity. This effect is independent of the fact that the absolute magnitude of the reflectivities differ for the various polarization configurations.

114

FIG. 4.6: Line-center reflectivity curves for different linear polarization configurations of the $R_{1f}(8)$ transition as a function of average saturation intensity $< I_{sat}^{ex} >= 1.77$ MW/cm^2-cm^{-1} (bottom), and pump field spectral intensity (top). In the figure -■-, -▲-, -●- and -◆- correspond to the XXXX, YXYX, YYXX and XYYX polarization configurations, respectively. The solid curves are nonlinear least squares fits of the data to the MCECA model, Eq. (14). All of the reflectivity curves peak at approximately the same pump field intensity.
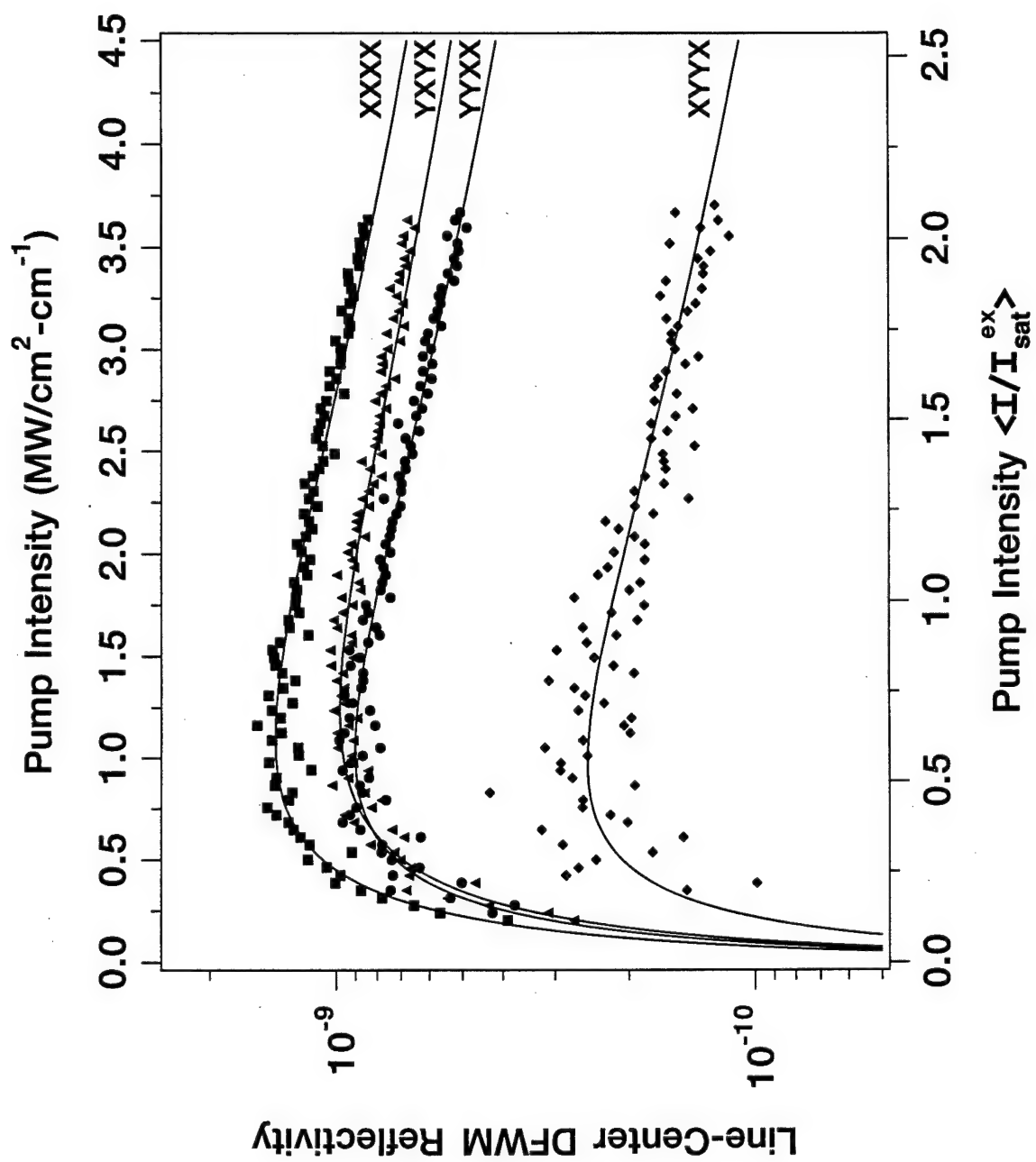
Table 4.2. Experimentally determined line-center saturation intensities.

Transition	$\varepsilon_4\varepsilon_1\varepsilon_3\varepsilon_2$	AL I_{sat}^{ex} (MW/cm^2-cm^{-1})	MCECA I_{sat}^{ex} (MW/cm^2-cm^{-1})
$Q_{1ef}(4)$	YYXX	1.88 ± 1.19	1.76 ± 0.74
$R_{1f}(4)$	YYXX	2.47 ± 0.83	2.21 ± 0.54
$Q_{1ef}(8)$	YXYX	1.06 ± 0.38	1.12 ± 0.25
$Q_{1ef}(8)$	YYXX	1.00 ± 0.51	1.08 ± 0.32
$R_{1f}(8)$	XXXX	1.88 ± 0.33	1.79 ± 0.21
$R_{1f}(8)$	YXYX	2.30 ± 0.43	2.07 ± 0.29
$R_{1f}(8)$	YYXX	1.68 ± 0.41	1.72 ± 0.25
$R_{1f}(8)$	XYYX	1.21 ± 1.34	1.51 ± 0.81

We suggest the following explanation for the weak sensitivity of the DFWM saturation intensity to polarization. In the framework of the MCECA discussed in Sec. III, the DFWM signal saturates when the population difference of Eq. (12) induced by the counterpropagating pump fields approaches zero over the entire interaction volume. At this point the probe field cannot perturb the population (make gratings) and the DFWM reflectivity approaches zero. The intensity at which the spatial population difference of the two-level system approaches zero is determined by I_{sat}^o. Because $I_{sat}^o \propto b\Gamma_o / |\mu_{ge}|^2$ for the MCECA model, this intensity is related to the collisional relaxation caused by the environment and the Einstein absorption coefficient ($|\mu_{ge}|^2 = (3\varepsilon_o \hbar^2 / \pi)B_{ge}$). For a nondegenerate two-level system this intensity is unambiguous.

The transition probabilities for a molecular (degenerate) transition, however, are dependent on the magnetic sublevels involved, the type of transition, and polarization state of the excitation field. In other words, for a given transition and field polarization, some magnetic sublevels interact strongly with the field and others do not. Those sublevels interacting strongly with the field saturate more rapidly than those that do not. Therefore to describe the saturation properties of a molecular system each magnetic sublevel must be treated independently, i.e., there is no single Rabi frequency for a degenerate system.[58] It is common in rate equation models of molecular processes, however, to use Einstein A and B coefficients[57] which represent an equally weighted average of the transition probabilities of all the magnetic sublevels.[34,58-60] Furthermore if the initial magnetic sublevel distribution is isotropic the average optical pumping rate, i.e., the rms Rabi frequency, is independent of the field polarization.[58]

Therefore to a first approximation the average intensity at which the population difference approaches zero will be related to the Einstein absorption coefficient. Furthermore we expect this intensity to be similar for the different polarization cases provided that the magnetic sublevels relax with equal rates, i.e., if the population, orientation, and alignment relax equally.[24] In Sec. IVA we showed this to be a reasonable assumption for CH in this flame. The saturation data presented in Table 4.2 validates this expectation because the saturation intensities for different polarization configurations involving the same transitions are similar; the values are within a factor of two of one another. In addition the ratio of the $Q_{1ef}(4)$ and $R_{1f}(4)$ saturation intensities is 0.80 ± 0.39, and the ratio of the $Q_{1ef}(8)$ and $R_{1f}(8)$ saturation intensities is 0.63 ± 0.21. These values are close to the inverse ratio of the B_{ge} coefficients for these transitions of 1.01 and 0.71, respectively. Note that the polarization dependence of the Q- and R-branch transitions differ sharply. In constructing these saturation ratios we used the

118

YYXX saturation intensities of the MCECA model, chose transitions that shared a common ground level, and assumed that effects arising from differences in the excited level degeneracies and collisional rates are small.

C. Numerical Comparisons

The calculated AL and MCECA saturation intensities for the $R_{1f}(8)$ transition using $\Gamma_o = \Gamma_{12} = 2$ x 10^9 s^{-1} and $|\mu_{ge}| = 0.405$ D are 0.0031 MW/cm^2 and 0.028 MW/cm^2, respectively. The bandwidth-corrected MCECA saturation intensity is approximately an order of magnitude larger than the AL saturation intensity; however, the MCECA saturation intensity is still an order of magnitude smaller than our average experimentally determined value of 0.32 ± 0.08 MW/cm^2. Order-of-magnitude agreement was also observed in the MCECA experiments.[13] There are several possible reasons for the discrepancy between the calculated and measured saturation intensities; although no single reason appears to be able to account for such a large difference.

The fact the MCECA model does not include effects arising from the spatial beam properties could account for some of the difference (possibly up to a factor of ten). The LFR calculations discussed in Sec. I, however, showed good agreement with their experimental results using a narrow-bandwidth laser even though the calculations neglected the spatial characteristics of the excitation beams. Therefore it is unlikely that the Gaussian nature of the excitation beams is solely responsible. The LFR calculations did show, however, that the saturation intensity increases as the ratio $2\Gamma_{eg}$ to $\Delta\omega_D$ decreases. Therefore the fact that the molecules are moving may account for some of the difference (less than a factor of 2). It is also possible that we have underestimated the values of the relaxation rates by employing the simple $T^{1/2}$ temperature extrapolation and by neglecting the effects of velocity changing collisions. Using larger relaxation rates would increase the calculated saturation intensity (possibly a factor of 2).

Another indication of saturation is power-broadening of spectral line shapes. Figure 7 shows the average DFWM line width (fwhm) of the $R_{1e}(8)$, $R_{1f}(8)$, $R_{2e}(8)$, and $R_{2f}(8)$ transitions as a function of I/I_{sat}. Each data point in Fig. 7 represents a separate spectral scan from which an average value was obtained. The solid line is the theoretical MCECA model prediction of Eq. (13) using the laser bandwidth of $\Delta\overline{\upsilon} = 0.18$ cm^{-1} and no adjustable parameters. The experimental data is plotted vs. I/I_{sat}^{ex} and the theoretical curve is plotted vs. I/I_{sat}^o where I_{sat}^{ex} and I_{sat}^o are the experimental and theoretical saturation intensities, respectively. The simplified form of the MCECA model expressed

119
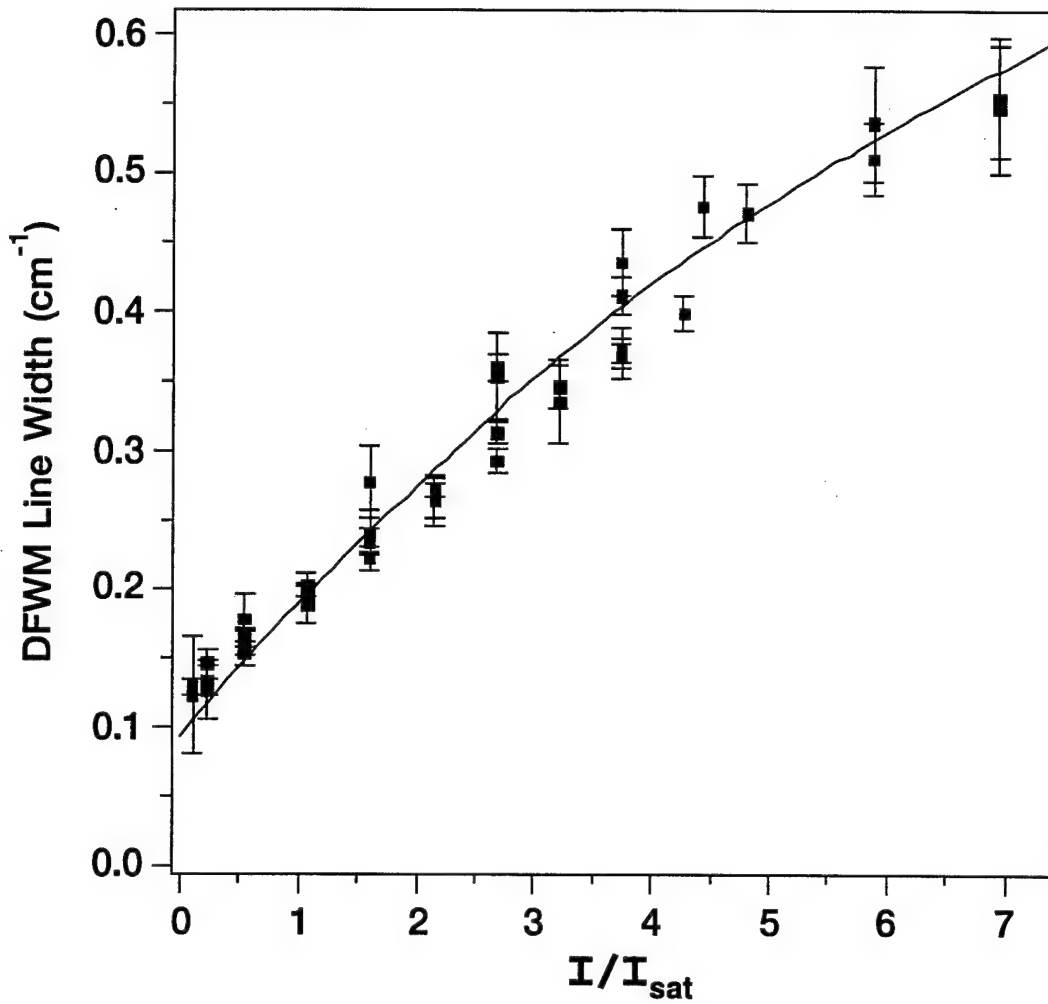
FIG. 4.7. Average DFWM line width (fwhm) of the $R_{1e}(8)$, $R_{1f}(8)$, $R_{2e}(8)$, and $R_{2f}(8)$
transitions as a function of I/I_{sat}. Each data point represents a separate spectral scan
from which an average value was obtained. The solid line is the theoretical MCECA
model prediction of Eq. (13) using the laser bandwidth of $\Delta\overline{\upsilon} = 0.18$ cm^{-1} and no
adjustable parameters. The experimental data is plotted vs. I/I_{sat}^{ex} and the theoretical
curve is plotted vs. I/I_{sat}^{o} where I_{sat}^{ex} and I_{sat}^{o} are the experimental and theoretical
saturation intensities, respectively.

in Eq. (13) is strictly valid for small detunings ($\Delta < b$); however, the agreement of the model with the data is quite good even for laser intensities outside the range of applicability defined in Eq. (18). In addition Eq. (13) approximates a power-broadened Lorentzian-cubed line shape for laser intensities less than $3\ I_{sat}$, and this line shape reproduces the experimental data.[12] Therefore an estimate of the degree of saturation of any transition can be determined from the power-broadened line width and Eq. (13).

A comparison can also be made between the calculated and measured DFWM reflectivities. Steel and Lamb[2,61] have empirically modified the AL reflectivity expression for homogeneously broadened systems to apply to Doppler-broadened systems, i.e., $\Delta\omega_D \gg 2\Gamma_{eg}$. The resulting expression also showed good agreement with their experimental data. Steel and Lamb express the Doppler-broadened reflectivity, R_D, as

$$R_D \cong \frac{\pi}{16}\ \frac{(\Gamma_{eg})^2}{(ku)^2}\ R_{AL}(\Delta = 0), \tag{21}$$

where u is the most probable speed of the Maxwell-Boltzmann velocity distribution and $R_{AL}(\Delta = 0)$ is the line-center DFWM reflectivity of Eq. (9) for homogeneously broadened media. We note that Eq. (21) is consistent with the ratio of perturbative expressions (Chapter 3, Eqs. (46)-(51)) evaluated in the Doppler-broadened limit ($\Delta\omega_D \gg 2\Gamma_{eg}$) and homogeneously broadened limit ($\Delta\omega_D \ll 2\Gamma_{eg}$).[62]

MCECA have also presented an approximate expression for the Doppler-broadened reflectivity (Eq. (22) of reference 14). Comparing that expression to Eq. (14), we find that the Doppler-broadened DFWM reflectivity using broad-bandwidth lasers, i.e., $\Delta\omega_D > 2b \gg 2\Gamma_{eg}$, scales relative to the homogeneously broadened reflectivity as

$$R_D \cong \frac{\sqrt{\pi}}{8}\ \frac{b\Gamma_{eg}}{(ku)^2}\ R_{MCECA}(\Delta = 0), \tag{22}$$

where $R_{MCECA}(\Delta = 0)$ is the line-center DFWM reflectivity of Eq. (14) for homogeneously broadened media.

The calculated Doppler-broadened reflectivity for the MCECA model at $I = I^o_{sat}$ and $\Delta = 0$ for the $R_{1f}(8)$ transition is 1.0×10^{-9} using Eqs. (14) and (22). This value is calculated for $T = 2774$ K, $\Gamma_o = \Gamma_{eg} = 2 \times 10^9$ s^{-1}, $\Delta N = 1.1 \times 10^{12}$ molecules/cm^3 (population of the $F_{1f}(8)$ level), $|\mu_{ge}| = 0.405$ D, and $L = 1$ mm (diameter of the flame). The calculated reflectivity is close to the reflectivities measured at the experimental saturation intensity ($I = I^{ex}_{sat}$) which ranged from 0.2 to 1.2×10^{-9}. See Fig. 6. The smallest and largest values in the range correspond to data taken using the XYYX and XXXX polarization configurations, respectively. Because of the numerous calibrations

required to evaluate the reflectivity, the measured values are only accurate within a factor of three. Based on the agreement between the calculated and measured reflectivities, Eq. (22) should provide an order-of-magnitude estimate for the feasibility of detecting molecular species in Doppler-broadened media with broad-bandwidth lasers.

D. Relative Branch Intensities

The spectral scan shown in Fig. 2 was taken using the YYXX polarization configuration at 1.7 times the experimental saturation intensity of the $Q_{1ef}(8)$ transition. Using Eq. (13) we find that the line widths of the transitions shown in Fig. 2 represent a range of approximately 0.9 to 2.3 I_{sat}^{ex}. By varying B_{ge} by $\pm$ 10% for various I / I_{sat}^o values and numerically integrating Eq. (13) we find that the MCECA model predicts a $B_{ge}^{2.14}$ to $B_{ge}^{1.71}$ dependence for the integrated DFWM signal over the range of 0.9 to 2.3 I_{sat}^o. This absorption coefficient dependence is consistent with the experimental results of Farrow, Rakestraw, and Dreier.[47] These authors employed a multi-mode laser similar to that used here and found that the integrated DFWM signal exhibits a reduced absorption coefficient dependence for saturating laser intensities.

We have plotted in Fig. 8 the ratio of the integrated intensities for Q_1 and R_1 transitions that share a common initial state. In plotting the relative branch intensities as a function of J_g we assume that the population relaxation and dephasing rates do not differ significantly even though the Q branch involves J_g and $J_e = J_g$ and the R branch involves J_g and $J_e = J_g + 1$. The dashed curve in Fig. 8 is the B_{ge}^2 saturated two-level (STL) model prediction for the Q-to-R-branch ratio. We have used a simple B_{ge}^2 dependence because the average degree of saturation of the data shown in Fig. 8 is 1.26 I_{sat}^{ex} which corresponds to $B_{ge}^{1.96}$ according to the integrated MCECA model. The dotted curve in Fig. 8 is the $B_{ge}^4 G_F^T(\varepsilon_4, \varepsilon_1, \varepsilon_3, \varepsilon_2; J_g, J_e)^2$ diagrammatic perturbation theory (DPT) prediction where $G_F^T(\varepsilon_4, \varepsilon_1, \varepsilon_3, \varepsilon_2; J_g, J_e)$ is the total geometric factor of Table 3.2. Recall that if $\Gamma_e = \Gamma_g$ these values apply to R-branch PC-DFWM signals. Inspection of Fig. 8 indicates that neither model is able to account for the fact that the Q-branch transitions are weaker than the R-branch transitions for high values of J_g even though the Q-Branch absorption coefficients are larger. See Fig. 9.

The work of Farrow, Rakestraw, and Dreier[47] demonstrated that there is a reduced absorption coefficient dependence ($\sim B_{ge}^2$) at saturating laser intensities, and our polarization ratio data (Fig. 5) showed that the relative anisotropy of the total angular momentum distribution represented by the total geometric factors persists in the presence

122
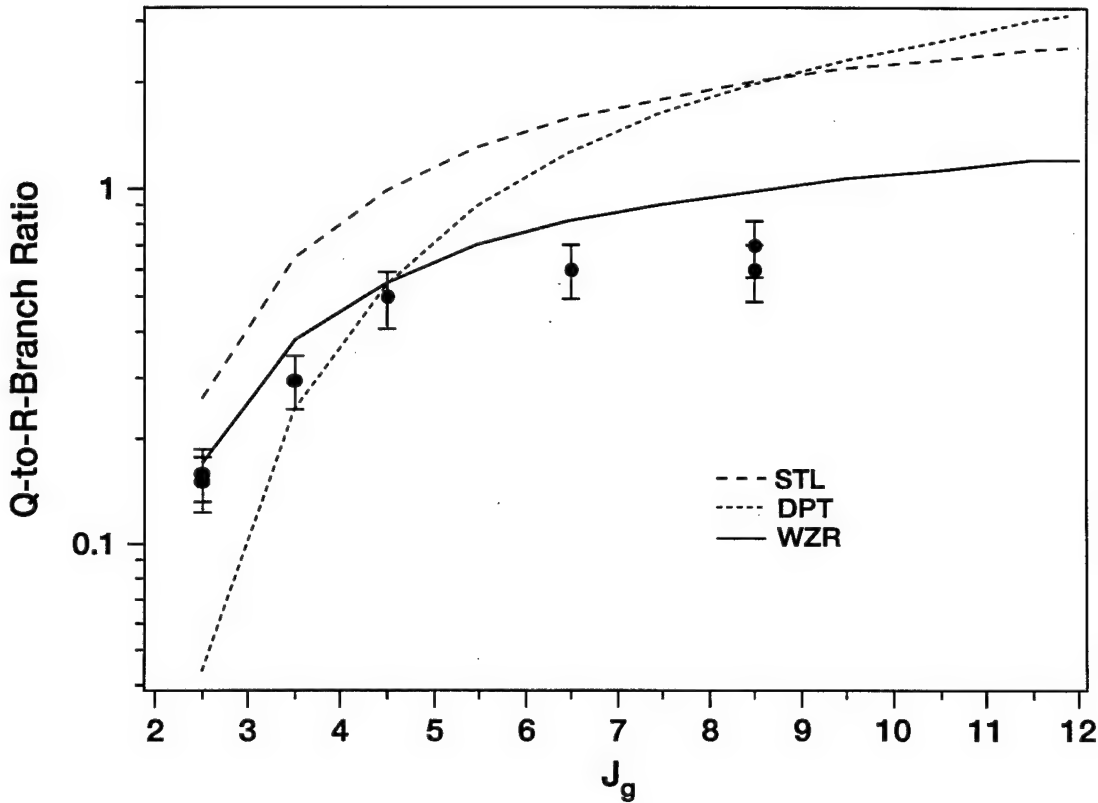
FIG. 4.8. Ratio of the integrated intensities for Q_1 and R_1 transitions that share a common initial state as a function of J_g. The dashed curve is the B_{ge}^2 saturated two-level model (STL) prediction for the Q-to-R-branch ratio, the dotted curve is the $B_{ge}^4 G_F^T(\varepsilon_4, \varepsilon_1, \varepsilon_3, \varepsilon_2; J_g, J_e)^2$ diagrammatic perturbation theory (DPT) prediction, and the solid curve is the $B_{ge}^2 G_F^T(\varepsilon_4, \varepsilon_1, \varepsilon_3, \varepsilon_2; J_g, J_e)^2$ empirical (WZR) prediction.
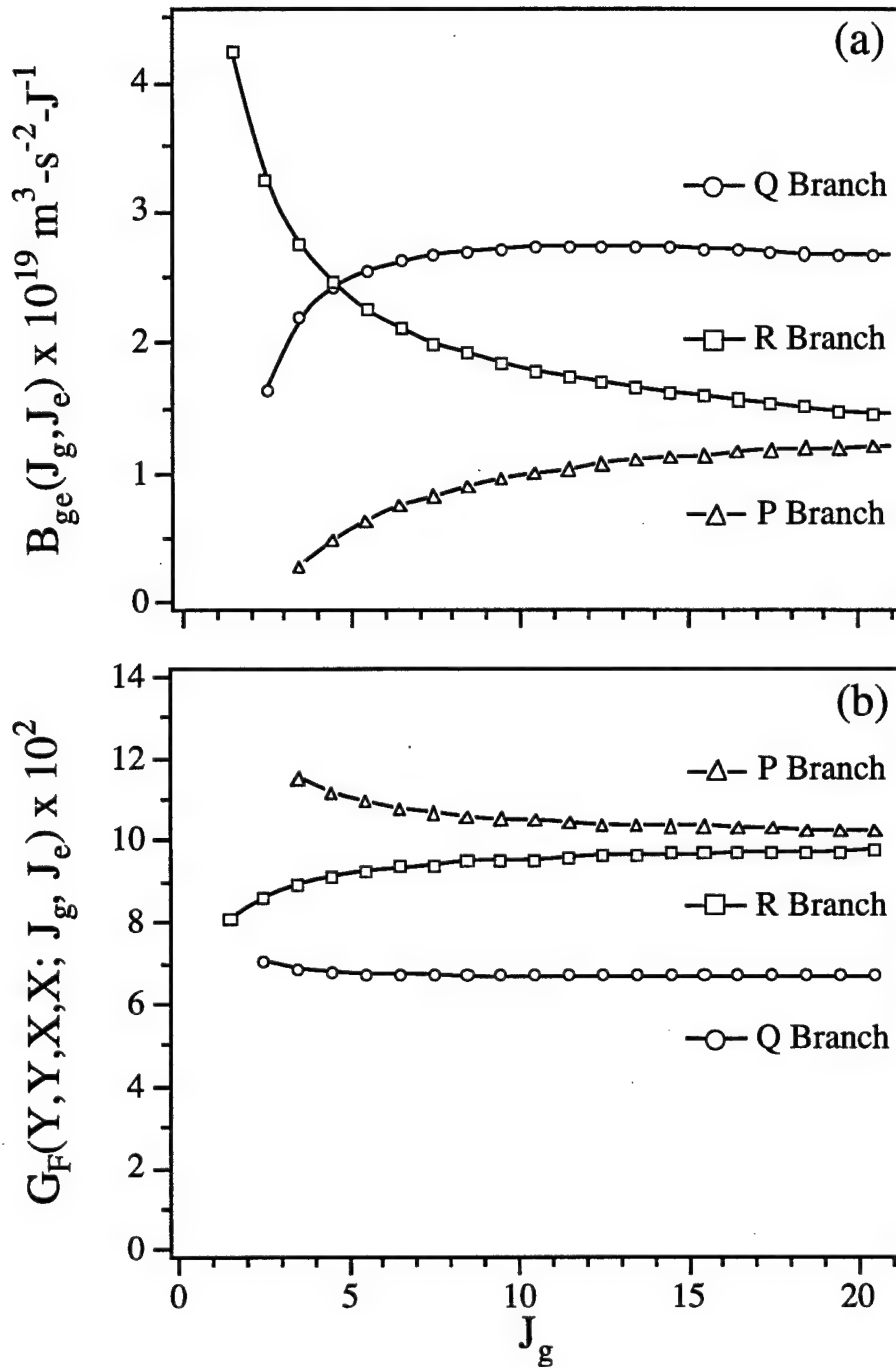
FIG. 4.9. (a) The Einstein absorption coefficients as a function of J_g for the R_1-, Q_1-. and P_1-branch transitions of CH labeled -□-, -O-, and -△-, respectively. The absorption coefficients for the R_2-, Q_2-. and P_2-branch transitions are nearly the same because both the X and A states rapidly approach Hund's case (b) coupling as rotation increases. (b) Total geometric factors of Table 3.2 for the YYXX polarization configuration as a function of J_g with the same conventions as (a).

124

of saturating fields. Therefore, we have also plotted $B_{ge}^2 G_F^T(\varepsilon_4, \varepsilon_1, \varepsilon_3, \varepsilon_2; J_g, J_e)^2$ in Fig. 8 which is the solid curve (WZR). In Fig. 8 it is apparent that both a reduced absorption coefficient dependence and a total geometric correction are necessary to account for the observed Q-to-R-branch ratios. Note at $J_g = 4.5$ the DPT and WZR curves are equal, and both curves are in excellent agreement with the observed ratio. The agreement at $J_g = 4.5$ results from the fact the absorption coefficients for the $Q_1(4)$ and $R_1(4)$ transitions are equal, so the ratio is determined exclusively by the geometric correction.   The agreement at other J_g values is not as good because the Q_1- and R_1-branch absorption coefficients are not equal, and therefore the transitions are not saturated to the same degree.

Once more the simple introduction of the geometric factors is able to explain the observed signal ratios with an accuracy in the range of 10-30%. We noted in Chapter 3 that at saturating laser intensities higher order moments of the angular momentum distribution contribute to the DFWM signal; however, these data suggest that the first three moments are sufficient nevertheless to predict relative signal strengths at laser intensities up to approximately twice the saturation intensity.

E. Relative Population Distributions

In general DFWM signals must be corrected for differences in collision rates, absorption coefficients, and geometric factors before relative population distributions can be determined. Previous saturated DFWM temperature determinations employing broad-bandwidth excitation, however, have shown good agreement with thermocouple[6] and coherent anti-Stokes Raman scattering [8,11] measurements without applying collisional and geometric corrections; the only J-dependent corrections made in these determinations were for relative absorption coefficients ($I_{DFWM} \propto B_{ge}^2$). In these experiments the laser intensity was in excess of the saturation intensity, and the analysis only involved DFWM signals from members of a single branch. We offer the following explanation for the apparent insensitivity of the DFWM signal to collisions and geometric corrections in these experiments and present the results of a rotational temperature analysis of the CH radical performed under similar conditions.

The reduced sensitivity to collisions is discussed first. The LFR calculations (Sec. I) for narrow-band DFWM of Doppler-broadened systems predict that the line-center DFWM signal is nearly independent of collisions at approximately 2 I_{sat}^o. This assertion is substantiated by their experimental data (Fig. 5 of reference 3 and Fig. 15 of reference 16) taken with a narrow-band excitation source. We can understand this result by considering

the how collisions affect the DFWM signal for Doppler-broadened systems. Using the total collisional dependence of the Doppler-broadened reflectivity of Eq. (21), we find that the line-center DFWM signal of the AL model has a zero-order collisional rate dependence at approximately $0.5 I_{sat}^o$. This value is in qualitative agreement with the LFR calculated value of $2 I_{sat}^o$. Without employing the additional collisional dependence of Eq. (21) for Doppler-broadened systems, the line-center DFWM signal of the AL model is independent of collisions only when $I >> I_{sat}^o$. This result is does not qualitatively agree with the LFR calculations.

By comparison we find using the total collisional dependence of the Doppler-broadened reflectivity of Eq. (22) that the line-center DFWM signal of the MCECA model has a zero-order collisional rate dependence at approximately $0.6 I_{sat}^o$. The applicability of Eq. (22) to our experiments is validated by the fact that the Doppler-broadened correction is necessary to account for the magnitude of our experimentally measured reflectivities. Hence it is reasonable to assume that broad-bandwidth DFWM signals of Doppler-broadened systems exhibit a reduced collisional dependence at laser intensities approximately equal to $2 I_{sat}^o$.

The independence of DFWM signals to geometric corrections results from that the fact that the total geometric factors are essentially constant for members of a single branch. As is shown in Fig. 9, the total geometric factors differ markedly for different branches, are J dependent for low J_g values, but are constant for each branch for values of J_g greater than three or four. We expect that once the geometric factors approach a high-J limit then the only remaining J-dependent corrections to saturated ($I \sim I_{sat}$) DFWM signal intensities for members of a single branch would arise from differences in absorption coefficients. We suggest that this behavior is the primary reason for the remarkable success of applying simple absorption coefficient corrections to determine relative population distributions from saturated DFWM signals.

We further emphasize this important point by presenting the results of a saturated DFWM rotational temperature analysis. In our rotational temperature determination we use Q-branch transitions recorded using the YYXX PC-DFWM experimental configuration with the laser intensity maintained at approximately 1.7 times the experimental saturation intensity of the $Q_{1ef}(8)$ transition. The average degree of saturation of all the Q-branch transitions used in the analysis is $1.6 I_{sat}^{ex}$ with a range of approximately 0.9 to 2.3 I_{sat}^{ex} as determined from the power-broadened line widths. This average degree of saturation corresponds to a $B_{ge}^{1.85}$ dependence for the integrated DFWM signal intensities according to the MCECA model. A Boltzmann plot of integrated Q-

126

branch transitions for $2.5 \leq J_g \leq 20.5$ is shown in Fig. 10. The lower line (STL) represents a least-squares linear regression analysis using data corrected for the $B_{ge}^{1.85}$ dependence, and the upper line (WZR) represents data corrected for the $B_{ge}^{1.85} G_F^T(\varepsilon_4, \varepsilon_1, \varepsilon_3, \varepsilon_2; J_g, J_e)^2$ dependence. In both linear regression analyses data corresponding to $3.5 \leq J_g \leq 20.5$ of resolved Q_1 and Q_2 transitions are used and no collisional corrections are applied.

We find that the geometric corrections only change the fitted temperature by 0.5%. This result is expected since the total geometric factors of the Q-branch are nearly constant over the range $3.5 \leq J_g \leq 20.5$. The data at the smallest term energies (J_g=2.5-4.5), however, deviate significantly from the data at larger term energies. Inspection of Fig. 9 shows that the Q-branch the absorption coefficients are J dependent for low values of J_g. We showed for the Q-to-R-branch ratios in Sec. IVD that the applied corrections, i.e., $B_{ge}^2 G_F^T(\varepsilon_4, \varepsilon_1, \varepsilon_3, \varepsilon_2; J_g, J_e)^2$, are only accurate to 10-30% when the relative absorption coefficients and geometric factors differ. Therefore using DFWM signal from members of a single branch and J values greater than three or four greatly reduces the error in determining the rotational temperature because both the absorption coefficients and total geometric factors are essentially J independent.

The degree of saturation of the data used in the analysis ranges from approximately $0.9 I_{sat}^{ex}$ at J_g=3.5 to 2.3 I_{sat}^{ex} at J_g=20.5. This range of saturation intensities corresponds to approximately a 60% decrease in the population relaxation rate, Γ_o, from J_g=3.5 to J_g=20.5 using $I_{sat}^{ex} \propto b \Gamma_o / B_{ge}$. A decrease in the relaxation rate with increasing J_g is expected for CH in this flame because $\Gamma_o \sim \Gamma_{eg} \sim \Gamma_g \sim \Gamma_e \sim R$ and R generally decreases as the spacing between adjacent rotational levels increases.[64] Hence if the DFWM signal were sensitive to collisions, a 60% variation in the collisional rate would significantly affect the temperature obtained from the Boltzmann analysis. For example the temperature would increase by approximately 160 K (>5%) if the DFWM signal were inversely proportional to the collisional rate.

The temperature obtained from the linear regression analysis of the data corrected for the $B_{ge}^{1.85} G_F^T(\varepsilon_4, \varepsilon_1, \varepsilon_3, \varepsilon_2; J_g, J_e)^2$ dependence is 2774 ± 58 K. This value is in consistent (within 5%) with our previously reported[12] CH vibrational temperatures of 2642 ± 99 K and 2882 ± 123 K obtained by LIF and DFWM, respectively. Because of the specific characteristics of the X and A states of CH, vibrational temperatures do not need to be corrected for relaxation, polarization, or saturation effects. This interesting aspect of high-pressure CH spectroscopy is discussed in detail in reference 12. Therefore the 5% agreement between the rotational temperature and vibrational temperatures

FIG. 4.10. Boltzmann plot of integrated Q-branch transitions for $2.5 \leq J_g \leq 20.5$ taken in the YYXX polarization configuration. The power-broadened line widths of the transitions used in the analysis indicate that the average degree of saturation of these data is 1.6 I_{sat}^{ex}. The lower line (STL) represents a least-squares linear regression analysis using data corrected for the $B_{ge}^{1.85}$ dependence, and the upper line (WZR) represents data corrected for the $B_{ge}^{1.85} G_F^T (\varepsilon_4, \varepsilon_1, \varepsilon_3, \varepsilon_2; J_g, J_e)^2$ dependence. In both linear regression analyses data corresponding to $3.5 \leq J_g \leq 20.5$ of resolved Q_1 and Q_2 transitions are used and no collisional corrections are applied.
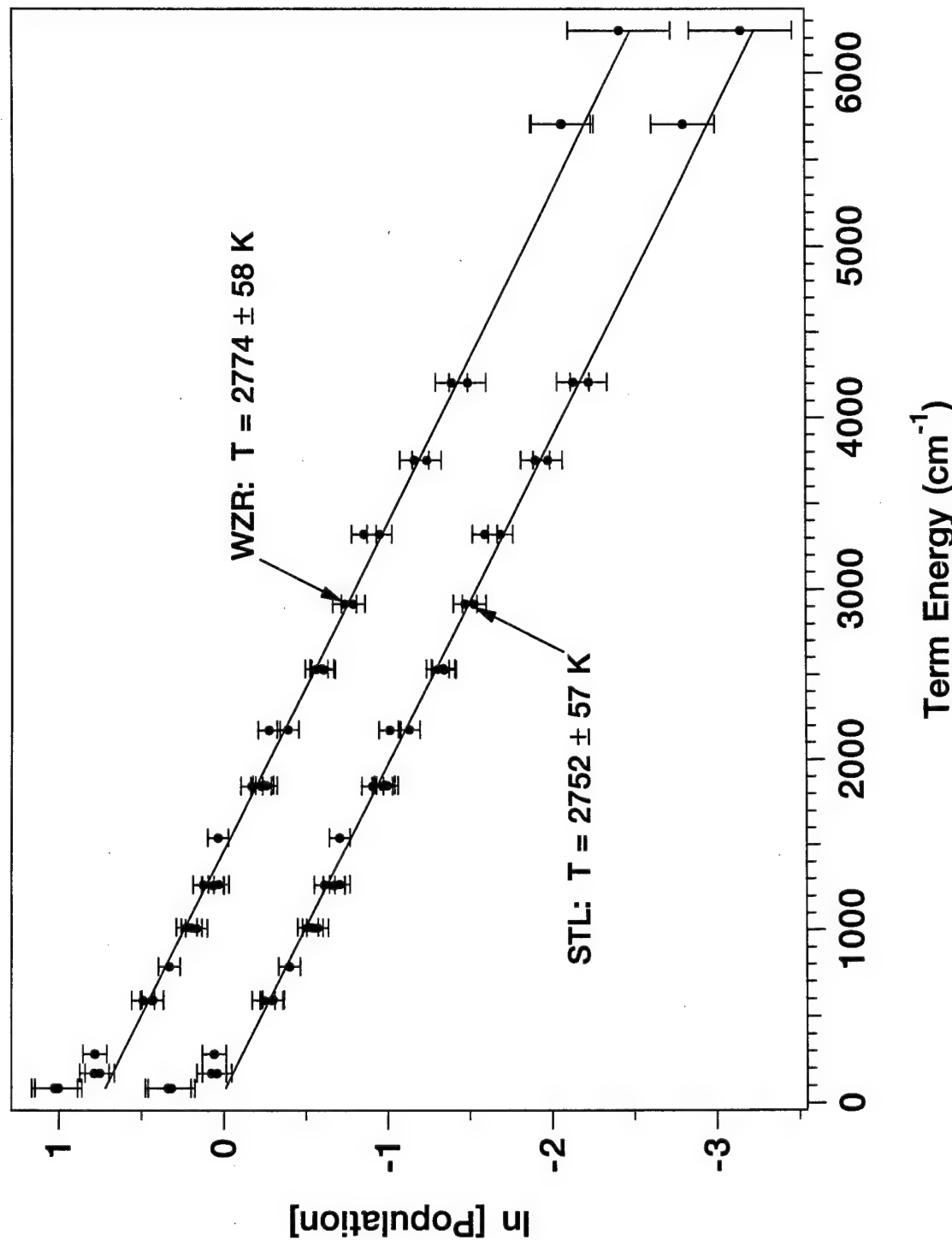
suggests that the DFWM signal does in fact exhibit a reduced (less than linear) collisional dependence when $I \sim I_{sat}^{ex}$.

Finally we comment on the rotational temperature error of 58 K (2%). This error is more indicative of the precision of these measurements rather than the accuracy because several significant assumptions were made in interpreting of the observed DFWM signals using the MCECA model. Based on these assumptions and the results presented in this chapter, a more realistic estimate of the accuracy of these measurements is 140 K (5%). This conclusion is also supported by the results of another ongoing project at Stanford which involves the investigation of trace radical species such as CH and C_2 in an atmospheric-pressure diamond synthesis reactor.[65-67] The reactor consists of an rf inductively-coupled argon plasma seeded with hydrogen and methane. These studies have focused on measuring CH and C_2 concentration profiles and CH vibrational and rotational temperatures using saturated DFWM. The results of these measurements are consistent with the results of numerical simulations of the deposition environment over temperature range of 2500-4000 K. Furthermore the agreement between the CH vibrational, rotational, and simulated temperatures has consistently been ~5%.[68-70]

V.   CONCLUSIONS

We have experimentally evaluated the effects of polarization in DFWM spectroscopy from the weak- to the strong-field limit. The effects of polarization were rationalized using the ideas developed in Chapter 3 for the weak-field limit. The key results are that the saturation intensity is relatively independent of polarization and that the DFWM spatial effects represented by the weak-field geometric factors of Chapter 3 are applicable at laser intensities up to twice the saturation intensity. Furthermore we showed that polarization ratios measured with weak fields can be used to infer important relaxation information.

The error in applying the weak-field geometric factors to saturated DFWM signals was found to be in the range of 10-30%. This degree of accuracy may be sufficient for determining energy transfer rates. In particular the sub-Doppler resolution offered by PC-DFWM would be advantageous for resolving energy transfer rate differences between different spin-orbit and Λ–doublet components that are difficult to resolve using LIF at these temperatures. In determining relative population distributions for temperature measurements, however, 10-30% accuracy is often not sufficient.

130

We showed in Sec. IV that if the absorption coefficients and the total geometric factors of a set of transitions are nearly the same, relative population distributions accurate to 5% can be extracted from saturated DFWM signals. Such behavior is expected for members of a single branch once the absorption coefficients and the total geometric factors reach a high J-limit. Therefore small values of J should be avoided in the analysis when accuracy is of primary importance. This result is an important finding because it substantiates a significant assumption in using two-level nondegenerate models to determine relative internal-state distributions of molecules. We also note that this finding is the same as that of Altkorn and Zare[57] for saturated LIF.

We supported this finding by presenting a rotational temperature analysis of the CH radical in an atmospheric-pressure flame. We employed a novel polarization configuration in this experiment which offered true zero-background detection and greatly discriminated against other intensity grating contributions to the DFWM signal. The laser intensity was maintained at approximately 1.7 times the experimental saturation intensity of the $Q_{1ef}(8)$ transition, and a PC-DFWM spectrum of the Q branch of the CH $A^2\Delta(v'=0)$-$X^2\Pi(v''=0)$ system was obtained in the YYXX polarization configuration. From a Boltzmann analysis a rotational temperature of 2774 ± 140 K was obtained. This rotational temperature is in good agreement with the average LIF and DFWM vibrational temperature of 2762 ± 160 K previously reported by our laboratory.

References

(1)   R. L. Abrams and R. C. Lind, *Opt. Lett.* **2**, 94 (1978), erratum **3**, 205 (1978).

(2)   R. L. Abrams, J. F. Lam, R. C. Lind, D. G. Steel and P. F. Liao, in *Optical Phase Conjugation*, edited by R. A. Fisher (Academic Press, New York, 1983), Chapter 8, and references therein.

(3)   R. L. Farrow and D. J. Rakestraw, *Science* **257**, 1894 (1992).

(4)   G. Hall and B. J. Whitaker, *JCS Faraday Trans.*, in press.

(5)   Chapter 3.

(6)   R. L. Farrow, D. J. Rakestraw and T. Dreier, *J. Opt. Soc. Am. B* **9**, 1770 (1992).

(7)   P. M. Danehy, E. J. Friedman-Hill, R. P. Lucht and R. L. Farrow, *Appl. Phys. B* **57**, 243 (1993).

(8)   T. Dreier and D. J. Rakestraw, *Opt. Lett.* **15**, 72 (1990).

(9)   M. Winter and P. P. Radi, *Opt. Lett.* **17**, 320 (1992).

(10)   B. Yip, P. M. Danehy and R. K. Hanson, *Opt. Lett.* **17**, 751 (1992).

(11)   T. Dreier and D. J. Rakestraw, *Appl. Phys. B* **50**, 479 (1990).

(12)   S. Williams, D. S. Green, S. Sethuraman and R. N. Zare, *J. Amer. Chem. Soc.* **114**, 9122 (1992).

(13)   D. R. Meacher, A. Charlton, P. Ewart, J. Cooper and G. Alber, *Phys. Rev. A* **42**, 3018 (1990).

(14)   J. Cooper, A. Charlton, D. R. Meacher, P. Ewart and G. Alber, *Phys. Rev. A* **40**, 5705 (1989).

(15)   G. Alber, J. Cooper and P. Ewart, *Phys. Rev. A* **31**, 2344 (1985).

(16)   R. P. Lucht, R. L. Farrow and D. J. Rakestraw, *J. Opt. Soc. Am. B* **10**, 1508 (1993).

(17)   D. Bloch and M. Ducloy, *J. Opt. Soc. Am.* **73**, 635 (1983); erratum **73**, 1844 (1983).

(18)   M. Ducloy, F. A. M. de Oliveira and D. Bloch, *Phys. Rev. A* **32**, 1614 (1985).

(19)   S. Le Boiteux, P. Simoneau, D. Bloch, F. A. M. de Oliveira and M. Ducloy, *IEEE J. Quantum Electron.* **QE-22**, 1229 (1986).

(20)   G. Grynberg, M. Pinard and P. Verkerk, *Opt. Commun.* **50**, 261 (1984).

(21)   M. Pinard, B. Kleinmann and G. Grynberg, *Opt. Commun.* **51**, 281 (1984).

(22)   G. Grynberg, M. Pinard and P. Verkerk, *J. Phys. (Paris)* **47**, 617 (1986).

(23)   P. Verkerk, M. Pinard and G. Grynberg, *Phys. Rev. A.* **35**, (1987).

(24)   G. P. Agrawal, *Opt. Lett.* **8**, 359 (1983).

(25)   J. M. Khosrofian and B. A. Garetz, *Appl. Opt.* **22**, 3406 (1983).

(26)   P. F. Bernath, C. R. Brazier, T. Olsen, R. Hailey, W. T. M. L. Fernando, C. Woods and J. L. Hardwick, *J. Molec. Spectrosc.* **147**, 16 (1991).

(27)   J. Hinze, G. C. Lie and B. Liu, *Astrophys. J.* **196**, 621 (1975).

(28)   N. L. Garland and D. R. Crosley, *J. Quant. Spectrosc. Radiat. Transfer* **33**, 591 (1985).

(29)   J. Luque and D. Crosley, to be submitted to *J. Quant. Spectrosc. Radiat. Transfer*.

(30)   J. Brzozowski, P. Bunker, N. Elander and P. Erman, *Astrophys. J.* **207**, 414 (1976).

(31)   M. Danielson, P. Erman, A. Hishikawa, M. Larsson, E. Rachlew-Kallne and G. Sundstrom, *J. Chem. Phys.* **98**, 9405 (1993).

(32)   I. Kovács, *Rotational Structure in the Spectra of Diatomic Molecules* (American Elsevier Publishing Company Inc., New York, 1969), Table 3.7, pp. 130.

(33)   The Kovács line strengths for CH are tabulated in C. I. M. Beenakker, P. J. F. Verbeek, G. R. Mohlmann and F. J. de Heer, *J. Quant. Spectrosc. Radiat. Transfer* **15**, 333 (1975).

(34)   R. C. Hilborn, *Am. J. Phys.* **50**, 982 (1982), Eqs. (9) and (10).

(35)   P. F. Bernath, *J. Chem. Phys.* **86**, 4838 (1987).

(36)   R. J. Cattolica, D. Stepowski, D. Puecheberty and M. Cottereau, *J. Quant. Spectrosc. Radiat. Transfer* **32**, 363 (1984).

(37)   N. L. Garland and D. R. Crosley, *Appl. Opt.* **24**, 4229 (1985).

(38)   N. L. Garland and D. R. Crosley, *Chem. Phys. Lett.* **134**, 189 (1987).

(39)   R. G. Joklik and J. W. Daily, *Combust. Flame* **69**, 211 (1987).

(40)   K. J. Rensberger, M. J. Dyer and R. A. Copelend, *Appl. Opt.* **27**, 3679 (1988).

(41)   D. E. Heard, J. B. Jeffries and D. R. Crosley, *Chem. Phys. Lett.* **178**, 533 (1991).

(42)   Y. Matsui, A. Yuuki, M. Sahara and Y. Hirose, *Jpn. J. of Appl. Phys.* **28**, 1718 (1989), Fig. 7

(43)   A. E. Siegman, *Lasers* (University Science Books, Mill Valley, CA, 1986), pp. 663-667.

(44)   T. S. Rose, W. L. Wilson, G. Wäckerle and M. D. Fayer, *J. Chem. Phys.* **86**, 5370 (1987).

(45)   M. Sargent III, M. O. Scully and W. E. Lamb, Jr., *Laser Physics* (Addison-Wesley Publishing Company, Inc., Redwood City, CA, 1974).

(46)   In the case of moving absorbers, these spatial holes wash out to some extent because the absorbers may move through several wavelengths of the field in their lifetimes. However, the absorbers with near zero velocity will interact most strongly with the

counterpropagating fields. As a result holes with a width related to Γ_{eg} are burned into the velocity distribution.

(47)   R. L. Farrow, D. J. Rakestraw and T. Dreier, *J. Opt. Soc. Am. B* **9**, 1770 (1992).

(48)   M. S. Brown, L. A. Rahn, and T. Dreier, *Opt. Lett.* **17**, 76 (1992).

(49)   R. Trebino, E. K. Gustafson and A. E. Siegman, *J. Opt. Soc. Am. B* **3**, 1295 (1986).

(50)   G. S. Agarwal, *Phys. Rev. A* **37**, 4741 (1988).

(51)   The probe field (2) is delayed with respect to the forward pump field (1) by a distance (~6 cm) greater than six times the coherence length of the laser, and the backward pump field (3) is delayed with respect to the forward pump field by a distance (~16 cm) greater than eighteen times the coherence length. Furthermore the interaction length of the fields is limited by the flame diameter (0.1 cm) to a distance approximately one tenth the coherence length. Under these conditions we assume that the MCECA theory is applicable.

(52)   The kinetics of four level molecular systems has been discussed by many authors. Some references pertinent to our studies are R. P. Lucht and N. M. Laurendeau, *Appl. Opt.* **18**, 856 (1979). J. O. Berg and W. L. Shackleford, *Appl. Opt.* **18**, 2093 (1979). R. P. Lucht, D. W. Sweeney and N. M. Laurendeau, *Appl. Opt.* **19**, 3295 (1980).

(53)   The temporal response of the DFWM signal was found to be approximately Gaussian with a fwhm in the range of 13-15 ns using fast photomultiplier (Hamamatsu R2393P) and a 1 GHz digitizing oscilloscope (HP54510A) for all experimental conditions. This observation suggests that the signal pulse shape follows that of the incident laser pulses and that the system response is steady state.

(54)   L. A. Rahn and M. S. Brown, submitted to *Opt. Lett.*.

(55)   S. Williams, L. Rahn, P. H. Paul, and J. Forsman, *Thermal Gratings in Flames,* in preparation.

(56)   S. Williams, R. N. Zare and L. A. Rahn, *Observation of Orientation and Alignment Dephasing in Resonant Four-Wave Mixing,* in preparation.

(57)   R. Altkorn and R. N. Zare, *Ann. Rev. Phys. Chem.* **35**, 265 (1984).

(58)   B. W. Shore, *The Theory of Coherent Atomic Excitation* (John Wiley & Sons, New York, 1990), Vol. I pp. 436-469 and Vol. II pp. 1343-1358.

(59)   E. U. Condon and G. H. Shortley, *Theory of Atomic Spectra* (Cambridge University Press, Cambridge, England, 1935).

(60)   R. N. Zare, *Angular Momentum* (John Wiley & Sons, New York, 1988).

(61)   D. G. Steel and J. F. Lam, *Opt. Commun.* **40**, 77 (1981).

(62)   M. Ducloy and D. Bloch, *Phys. Rev. A* **30**, 3107 (1984), Eq. (46).

(63)   For a nondegenerate two-level system, $\left|\mu_{ge}\right|^2 = \left|\mu_{eg}\right|^2$. For a degenerate two-level system, however, $(2J_g +1)\left|\mu_{ge}\right|^2 = (2J_e +1)\left|\mu_{eg}\right|^2$. The concentration difference, molecular line strength, and geometric factors of the DFWM intensity expression of Chapter 3, Eq. (2) have been normalized with respect to the ground level degeneracy $(2J_g +1)$. See Eqs. (47)-(51) of Chapter 3. Therefore in order to apply the geometric factors of Chapter 3, $\left|\mu_{ge}\right|^2 \propto B_{ge}$ must be used. Note that $\left|\mu_{ge}\right|^2$ has also been used in the two-level model expressions of Sec. III so that in the weak-field limit and for $N_g \gg N_e$ the two-level models will be equivalent to the Chapter 3 expressions derived rigorously.

(64)   T. A. Brunner and D. Prichard, in *Dynamics of the Excited State*, edited by K. P. Lawley (John Wiley & Sons, New York, 1982), pp. 589-641.

(65)   T. G. Owano, C. H. Kruger and M. A. Cappelli, *Mater. Res. Soc. Symp. Proc.* **190**, 131 (1991).

(66)   M. A. Cappelli, T. G. Owano and C. H. Kruger, *J. Mater. Res.* **5**, 2326 (1990).

(67)   T. G. Owano, D. G. Goodwin, C. H. Kruger and M. A. Cappelli, *Proc. 2nd Int. Conf. on the New Diamond Science and Technology*, Materials Research Society, Pittsburgh, PA, 497 (1991).

(68)   T. G. Owano, C. H. Kruger, D. S. Green, S. Williams and R. N. Zare, *Diamond and Related Materials* **2**, 661 (1993).

(69)   D. S. Green, T. G. Owano, S. Williams, D. G. Goodwin, R. N. Zare and C. H. Kruger, *Science* **259**, 1726 (1993).

(70)   T. G. Owano, E. H. Wahl, C. H. Kruger, D. S. Green and R. N. Zare, *Proc. of the 11th Int. Symp. on Plasma Chemistry*, 416 (1993).

APPENDIX

Calculation of the Polarization Tensor Products

Math, Math, and more Math

In this appendix we establish the notation used for expressing the polarization unit vectors and evaluate the polarization tensor products necessary to calculate the DFWM signal intensity for experimental configurations not treated in the text. In what follows, we rely on the definitions of symbols already introduced.

An arbitrary vector r can be expressed in Cartesian coordinates as

$$r = r_x e_x + r_y e_y + r_z e_z, \tag{A1}$$

and its complex conjugate r^* as

$$r^* = r_x^* e_x + r_y^* e_y + r_z^* e_z, \tag{A2}$$

where e_x, e_y, and e_z are unit vectors and r_x, r_y, and r_z are the standard Cartesian components of the vector r. The conventions for relating the unit vectors and the standard components of the Cartesian (real) basis to the spherical tensor (complex) basis are defined as follows:

$$e_{\pm 1} = \mp \tfrac{1}{\sqrt{2}} \left(e_x \pm i e_y \right) , \; e_0 = e_z, \qquad . \tag{A3}$$

and

$$r_{\pm 1}^{(1)} = \mp \tfrac{1}{\sqrt{2}} \left(r_x \pm i r_y \right) , \; r_0^{(1)} = r_z. \tag{A4}$$

It follows that

$$e_q^* = (-1)^q e_{-q} , \; e_q \cdot e_{q'}^* = \delta_{qq'}, \tag{A5}$$

and

$$(r^*)_q^{(1)} = (-1)^q \left[r_{-q}^{(1)} \right]^* \tag{A6}$$

where $q = 0, \pm 1$. Equations (A3) and (A4) in turn define the conventions for relating the unit vectors and the standard components of the spherical tensor basis to the Cartesian basis, i.e.,

$$e_x = -\tfrac{1}{\sqrt{2}} \left(e_{+1}^{(1)} - e_{-1}^{(1)} \right) , \; e_y = -\tfrac{i}{\sqrt{2}} \left(e_{+1}^{(1)} + e_{-1}^{(1)} \right) , \; e_z = e_0, \tag{A7}$$

and

$$r_x = -\tfrac{1}{\sqrt{2}} \left(r_{+1}^{(1)} - r_{-1}^{(1)} \right) , \; r_y = -\tfrac{i}{\sqrt{2}} \left(r_{+1}^{(1)} + r_{-1}^{(1)} \right) , \; r_z = r_0^{(1)}. \tag{A8}$$

Consequently, we have for the Cartesian basis

137

$$e_p^* = e_p \ , \ e_p \cdot e_{p'}^* = \delta_{pp'}, \tag{A9}$$

and

$$(r^*)_p = [r_p]^*, \tag{A10}$$

where $p = x, y, z$. Therefore adopting the standard definitions, we are left with the conclusion of expressing an arbitrary vector r and its complex conjugate r^* in the spherical tensor basis as

$$r = r_{+1}^{(1)} e_{+1}^* + r_0^{(1)} e_0^* + r_{-1}^{(1)} e_{-1}^* \tag{A11}$$

and

$$r^* = \left[r_{+1}^{(1)}\right]^* e_{+1} + \left[r_0^{(1)}\right]^* e_0 + \left[r_{-1}^{(1)}\right]^* e_{-1}, \tag{A12}$$

Hence we can express an orthonormal set of unit vectors ε_j in a generalized notation as

$$\varepsilon_j = \sum_i (\varepsilon_j)_i e_i^* \ , \ \varepsilon_j^* = (\varepsilon_j)^* = \sum_i [(\varepsilon_j)_i]^* e_i \ , \ \varepsilon_i \cdot \varepsilon_j^* = \delta_{ij} , \tag{A13}$$

where the standard components of the unit vectors are defined as

$$(\varepsilon_j)_i = \varepsilon_j \cdot e_i \ , \ [(\varepsilon_j)_i]^* = \varepsilon_j^* \cdot e_i^* \ , \ (\varepsilon_j^*)_i = \varepsilon_j^* \cdot e_i . \tag{A14}$$

Special care must be taken in interpreting Eq. (A14). We take $(\varepsilon_j)_i$ to represent the i component of the unit vector ε_j, $[(\varepsilon_j)_i]^*$ to represent the complex conjugate of the i component of the unit vector ε_j, and $(\varepsilon_j^*)_i$ to represent the i component of the complex conjugate of the unit vector ε_j, i.e., ε_j^*.

For light in a pure state of arbitrary polarization propagating along the space-fixed Z-axis (such a choice is always possible), its polarization unit vector and its complex conjugate may be represented by

$$\varepsilon_j = \cos\phi_j \, e_x + e^{i\delta_j} \sin\phi_j \, e_y = \tfrac{1}{\sqrt{2}}\left[\cos\phi_j - ie^{i\delta_j}\sin\phi_j\right]e_{-1}^* - \tfrac{1}{\sqrt{2}}\left[\cos\phi_j + ie^{i\delta_j}\sin\phi_j\right]e_{+1}^* \tag{A15}$$

and

$$\varepsilon_j^* = \cos\phi_j \, e_x + e^{-i\delta_j} \sin\phi_j \, e_y = \tfrac{1}{\sqrt{2}}\left[\cos\phi_j - ie^{-i\delta_j}\sin\phi_j\right]e_{-1}^* - \tfrac{1}{\sqrt{2}}\left[\cos\phi_j + ie^{-i\delta_j}\sin\phi_j\right]e_{+1}^* \tag{A16}$$

where ϕ_j ranges from 0 to π and δ_j is the phase necessary to describe elliptical polarization. Reference to Eqs. (A13)-(A16) shows that

$$(\varepsilon_j)_x = \cos\phi_j \ , \ (\varepsilon_j^*)_x = \cos\phi_j \ ,$$

138

$$(\varepsilon_j)_y = e^{i\delta_j}\sin\phi \; , \; (\varepsilon_j^*)_y = e^{-i\delta_j}\sin\phi_j \; ,$$

$$(\varepsilon_j)_{+1}^{(1)} = -\tfrac{1}{\sqrt{2}}\left[\cos\phi_j + ie^{i\delta_j}\sin\phi_j\right] \; , \; (\varepsilon_j^*)_{+1}^{(1)} = -\tfrac{1}{\sqrt{2}}\left[\cos\phi_j + ie^{-i\delta_j}\sin\phi_j\right] \; ,$$

$$(\varepsilon_j)_{-1}^{(1)} = \tfrac{1}{\sqrt{2}}\left[\cos\phi_j - ie^{i\delta_j}\sin\phi_j\right] \; , \; (\varepsilon_j^*)_{-1}^{(1)} = \tfrac{1}{\sqrt{2}}\left[\cos\phi_j - ie^{-i\delta_j}\sin\phi_j\right] \; . \qquad \text{(A17)}$$

For completeness we define left circularly polarized light[1] ($\phi_L = \pi/4$, $\delta_L = \pi/2$) as

$$\varepsilon_L = \tfrac{1}{\sqrt{2}}\left(e_x + ie_y\right) = e_{-1}^* \; , \qquad\qquad \text{(A18)}$$

right circularly polarized light ($\phi_R = \pi/4$, $\delta_R = -\pi/2$) as

$$\varepsilon_R = \tfrac{1}{\sqrt{2}}\left(e_x - ie_y\right) = -e_{+1}^* \; , \qquad\qquad \text{(A19)}$$

and light of arbitrary linear polarization ($\delta_j = 0$) as

$$\varepsilon_j = \cos\phi_j \, e_x + \sin\phi_j \, e_y = \tfrac{1}{\sqrt{2}}\left[e^{-i\phi_j}e_{-1}^* - e^{i\phi_j}e_{+1}^*\right] \; . \qquad\qquad \text{(A20)}$$

The polarization tensors of Chapter 3, Eq. (51) in the text are expanded and expressed in the spherical tensor basis as

$$F(\varepsilon_4,\varepsilon_i,\varepsilon_j,\varepsilon_2;K) = \sum_{Q,q,q'}(-1)^Q (\varepsilon_4^*)_{-q}^{(1)} (\varepsilon_j)_{q+Q}^{(1)} (\varepsilon_2^*)_{-q'}^{(1)} (\varepsilon_i)_{q'-Q}^{(1)} \begin{pmatrix} 1 & 1 & K \\ -q & q+Q & -Q \end{pmatrix}\begin{pmatrix} 1 & 1 & K \\ -q' & q'-Q & Q \end{pmatrix}, \text{ (A21)}$$

where the terms in parenthesis are 3-j symbols. The polarization tensors in the Cartesian basis are readily worked out using Eq. (A4) and (A21). The resulting expression does not have a compact form, so the polarization tensors are presented for each value of K, i.e.,

$$F(\varepsilon_4,\varepsilon_i,\varepsilon_j,\varepsilon_2;0) = \frac{1}{3}\Big\{ \left[(\varepsilon_4^*)_x \, (\varepsilon_j)_x + (\varepsilon_4^*)_y \, (\varepsilon_j)_y + (\varepsilon_4^*)_z \, (\varepsilon_j)_z\right]$$

$$\times \left[(\varepsilon_2^*)_x \, (\varepsilon_i)_x + (\varepsilon_2^*)_y \, (\varepsilon_i)_y + (\varepsilon_2^*)_z \, (\varepsilon_i)_z\right] \Big\}, \qquad \text{(A22a)}$$

$$F(\varepsilon_4,\varepsilon_i,\varepsilon_j,\varepsilon_2;1) = -\frac{1}{2}\Big\{ \left[(\varepsilon_4^*)_x \, (\varepsilon_j)_y - (\varepsilon_4^*)_y \, (\varepsilon_j)_x\right] \times \left[(\varepsilon_2^*)_x \, (\varepsilon_i)_y - (\varepsilon_2^*)_y \, (\varepsilon_i)_x\right]$$

$$+ \left[(\varepsilon_4^*)_z \, (\varepsilon_j)_x - (\varepsilon_4^*)_x \, (\varepsilon_j)_z\right] \times \left[(\varepsilon_2^*)_z \, (\varepsilon_i)_x - (\varepsilon_2^*)_x \, (\varepsilon_i)_z\right]$$

$$- \left[(\varepsilon_4^*)_z \, (\varepsilon_j)_y - (\varepsilon_4^*)_y \, (\varepsilon_j)_z\right] \times \left[(\varepsilon_2^*)_z \, (\varepsilon_i)_y - (\varepsilon_2^*)_y \, (\varepsilon_i)_z\right] \Big\}, \text{ (A22b)}$$

and

$$F(\varepsilon_4,\varepsilon_i,\varepsilon_j,\varepsilon_2;2)=\frac{1}{6}\Bigg\{\ \Big[2\,(\varepsilon_4^*)_z\,(\varepsilon_j)_z - (\varepsilon_4^*)_x\,(\varepsilon_j)_x - (\varepsilon_4^*)_y\,(\varepsilon_j)_y\Big]$$

$$\times \Big[2\,(\varepsilon_2^*)_z\,(\varepsilon_i)_z - (\varepsilon_2^*)_x\,(\varepsilon_i)_x - (\varepsilon_2^*)_y\,(\varepsilon_i)_y\Big]\ \Bigg\}$$

$$+\frac{1}{2}\Bigg\{\ \Big[(\varepsilon_4^*)_z\,(\varepsilon_j)_x + (\varepsilon_4^*)_x\,(\varepsilon_j)_z\Big]\times\Big[(\varepsilon_2^*)_z\,(\varepsilon_i)_x + (\varepsilon_2^*)_x\,(\varepsilon_i)_z\Big]$$

$$+\Big[(\varepsilon_4^*)_z\,(\varepsilon_j)_y + (\varepsilon_4^*)_y\,(\varepsilon_j)_z\Big]\times\Big[(\varepsilon_2^*)_z\,(\varepsilon_i)_y + (\varepsilon_2^*)_y\,(\varepsilon_i)_z\Big]$$

$$+\Big[(\varepsilon_4^*)_x\,(\varepsilon_j)_x - (\varepsilon_4^*)_y\,(\varepsilon_j)_y\Big]\times\Big[(\varepsilon_2^*)_x\,(\varepsilon_i)_x - (\varepsilon_2^*)_y\,(\varepsilon_i)_y\Big]$$

$$+\Big[(\varepsilon_4^*)_x\,(\varepsilon_j)_y + (\varepsilon_4^*)_y\,(\varepsilon_j)_x\Big]\times\Big[(\varepsilon_2^*)_x\,(\varepsilon_i)_y + (\varepsilon_2^*)_y\,(\varepsilon_i)_x\Big]\ \Bigg\}.\text{(A22c)}$$

Equations (A21) and (A22) can be used to obtain the DFWM signal intensity along ε_4, i.e., the DFWM signal direction. It is often possible to predict the direction of ε_4 by invoking symmetry arguments of $\chi^{(3)}$. These equations also apply for polarized detection in which case ε_4 is the polarization axis of the DFWM detector.

For experiments in which it is difficult to predict the DFWM signal direction by symmetry arguments or for unpolarized detection, it is more useful to express the DFWM signal intensity in terms of its components. Rewriting the DFWM signal intensity of Chapter 3, Eq. (19) in Sec IIIA in terms of the components of the generalized basis of orthonormal unit vectors defined by Eqs. (A13) and (A14) yields

$$I_{DFWM}\propto\left\langle\left|P^{(3)}(r,t)\right|^2\right\rangle=\sum_j\left|\wp_j^{(3)}\right|^2 \tag{A23}$$

where $\wp_j^{(3)}$ is the scalar amplitude of the j component of $P^{(3)}(r,t)$ and is defined as

$$\wp_j^{(3)}=P_{DFWM}^{(3)}\cdot\varepsilon_j^*. \tag{A24}$$

Equation (A24) can be rewritten using the notation of Chapter 3, Eqs. (45)-(51) as

$$\wp_j^{(3)}=\frac{9\varepsilon_0^2\hbar}{8\pi^2}\left[N_g-\frac{(2J_g+1)}{(2J_e+1)}N_e\right]\left[B_{ge}\left(J_g,J_e\right)\right]^2\,\mathcal{E}_1\,\mathcal{E}_2^*\,\mathcal{E}_3$$

$$\times\Bigg\{\ \sum_K L_{12}^g(\omega,K)\,G(J_g,J_e;K)\,F(\varepsilon_j,\varepsilon_1,\varepsilon_3,\varepsilon_2;K)$$

$$+\sum_K L_{12}^e(\omega,K)\,G(J_e,J_g;K)\,F(\varepsilon_j,\varepsilon_1,\varepsilon_3,\varepsilon_2;K)$$

$$+ \sum_{K} L_{32}^{g}(\omega,K)\, G(J_{g},J_{e};K)\, F(\varepsilon_{j},\varepsilon_{3},\varepsilon_{1},\varepsilon_{2};K)$$

$$+ \sum_{K} L_{32}^{e}(\omega,K)\, G(J_{e},J_{g};K)\, F(\varepsilon_{j},\varepsilon_{3},\varepsilon_{1},\varepsilon_{2};K) \Bigg\}. \quad (A25)$$

where all of the terms have their previous meanings.

Equation (A25) can also be expressed in terms of its standard components. In the spherical tensor basis $\varepsilon_{j} = e_{q}^{*}$, and the polarization tensors in Eq. (A25) take on the form

$$F(e_{q}^{*},\varepsilon_{i},\varepsilon_{j},\varepsilon_{2};K) = \sum_{Q=-K}^{K} (-1)^{Q} \left[e_{q}^{(1)} \otimes \varepsilon_{j}^{(1)} \right]_{Q}^{(K)} \left[\varepsilon_{2}^{*(1)} \otimes \varepsilon_{i}^{(1)} \right]_{-Q}^{(K)}. \quad (A26)$$

Substitution of $(e_{q})_{-q''}^{(1)} = e_{q} \cdot e_{-q''} = (-1)^{q} \delta_{qq''}$ into Eq. (A21) gives

$$F(e_{q}^{*},\varepsilon_{i},\varepsilon_{j},\varepsilon_{2};K) = \sum_{Q,q'} (-1)^{q+Q} (\varepsilon_{j})_{q+Q}^{(1)} (\varepsilon_{2}^{*})_{-q'}^{(1)} (\varepsilon_{i})_{q'-Q}^{(1)} \begin{pmatrix} 1 & 1 & K \\ -q & q+Q & -Q \end{pmatrix} \begin{pmatrix} 1 & 1 & K \\ -q' & q'-Q & Q \end{pmatrix} \quad (A27)$$

which can be used in Eq. (A25) to generate the expression for the scalar amplitude of the q component of the nonlinear polarization $P^{(3)}(r,t)$. The resulting expression is equivalent to Eqs. (33) and (34) of reference 2 derived using a density matrix approach in the weak-field limit. In the Cartesian basis $\varepsilon_{j} = e_{p}^{*}$, and substitution of $(\varepsilon_{p})_{p''} = e_{p} \cdot e_{p''} = \delta_{pp''}$ into Eq. (A22) for $p=y$ gives the Y component of the polarization tensors as a function of K, namely,

$$F(e_{y}^{*},\varepsilon_{i},\varepsilon_{j},\varepsilon_{2};0) = \frac{1}{3}\Big\{ \big[(\varepsilon_{j})_{y} (\varepsilon_{2}^{*})_{x} (\varepsilon_{i})_{x} + (\varepsilon_{j})_{y} (\varepsilon_{2}^{*})_{y} (\varepsilon_{i})_{y} + (\varepsilon_{j})_{y} (\varepsilon_{2}^{*})_{z} (\varepsilon_{i})_{z} \big] \Big\}, \quad (A28a)$$

$$F(e_{y}^{*},\varepsilon_{i},\varepsilon_{j},\varepsilon_{2};1) = \frac{1}{2}\Big\{ \big[(\varepsilon_{j})_{x} (\varepsilon_{2}^{*})_{x} (\varepsilon_{i})_{y} - (\varepsilon_{j})_{x} (\varepsilon_{2}^{*})_{y} (\varepsilon_{i})_{x} \big]$$

$$+ \big[(\varepsilon_{j})_{z} (\varepsilon_{2}^{*})_{z} (\varepsilon_{i})_{y} - (\varepsilon_{j})_{z} (\varepsilon_{2}^{*})_{y} (\varepsilon_{i})_{z} \big] \Big\}, \quad (A28b)$$

and

$$F(e_{y}^{*},\varepsilon_{i},\varepsilon_{j},\varepsilon_{2};2) = -\frac{1}{6}\Big\{ \big[2(\varepsilon_{j})_{y} (\varepsilon_{2}^{*})_{z} (\varepsilon_{i})_{z} - (\varepsilon_{j})_{y} (\varepsilon_{2}^{*})_{x} (\varepsilon_{i})_{x} - (\varepsilon_{j})_{y} (\varepsilon_{2}^{*})_{y} (\varepsilon_{i})_{y} \big] \Big\}$$

$$+ \frac{1}{2}\Big\{ \big[(\varepsilon_{j})_{z} (\varepsilon_{2}^{*})_{z} (\varepsilon_{i})_{y} + (\varepsilon_{j})_{z} (\varepsilon_{2}^{*})_{y} (\varepsilon_{i})_{z} \big]$$

$$- \big[(\varepsilon_{j})_{y} (\varepsilon_{2}^{*})_{x} (\varepsilon_{i})_{x} - (\varepsilon_{j})_{y} (\varepsilon_{2}^{*})_{y} (\varepsilon_{i})_{y} \big]$$

$$+\left[(\varepsilon_j)_x\,(\varepsilon_2^*)_x\,(\varepsilon_i)_y + (\varepsilon_j)_x\,(\varepsilon_2^*)_y\,(\varepsilon_i)_x\right]\Bigg\}. \qquad\text{(A28c)}$$

The X and Z components are readily evaluated by reiterating the procedure for $p=x$ and z, respectively.

For the near collinear phase matching geometries and pure polarization states described in this thesis, only one standard component is nonzero. This result can be verified by substituting the polarizations of the input fields E_1, E_2, and E_3 into Eq. (A26) and (A28) using the definitions of Eqs. (A18) and (A19) for circularly polarized light and Eq. (A20) for $\phi_j = 0$ and $\phi_j = \pi/2$ linearly polarized light. These substitutions yield the results presented in Table 3.5. For noncollinear phase matching geometries, mixed polarization states, or both, all of the components must be determined.

The above expressions refer to the standard components of the electric fields when all the fields are defined with respect to a common reference frame. For example, in the case of noncollinear phase matching geometries, all the fields must be rotated into a common frame of reference (we suggest the detection frame) before the standard components can be determined. Such frame rotations are readily carried out in the spherical tensor basis using Wigner rotation matrices or in the Cartesian basis using direction cosine matrices. For more information on this topic, see reference 3, Chapter 3.

(1) E. Hecht, *Optics* (Addison-Wesley Publishing, Inc., Reading, MA, 1987).

(2) M. Ducloy and D. Bloch, *Phys. Rev. A* **30**, 3107 (1984).

(3) R. N. Zare, *Angular Momentum* (John Wiley & Sons, New York, 1988).